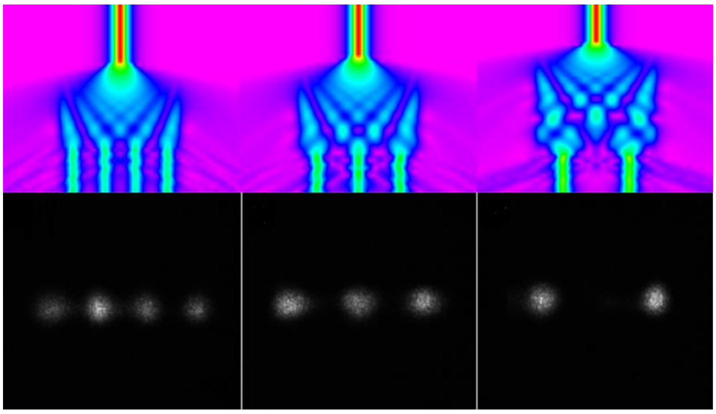

Fabrication of Integrated Optical Devices in Fused Silica by Femtosecond Laser Direct Writing

Vítor Alexandre Oliveira Amorim
Mestrado em Engenharia Física
Departamento de Física e Astronomia
2016

Orientador
Paulo Vicente da Silva Marques, Professor Auxiliar, Faculdade de Ciências da Universidade do Porto

MSc

U.PORTO

FACULDADE DE CIÊNCIAS
UNIVERSIDADE DO PORTO

Todas as correções determinadas pelo júri, e só essas, foram efetuadas.

O Presidente do Júri,

Porto, ______/______/_________

Acknowledgments

The realization of this dissertation would not be possible without the collaboration and contribution of several people, and for this reason I would like to express some words of acknowledgment and gratitude.

First of all, I would like to express my gratitude to Prof. Dr. Paulo Marques, my supervisor, for his support, dedication and advice that guided me throughout this dissertation. I would also like to thank him for the opportunities given and for making me a better professional. At last, I want to say that his companionship and friendship made this journey so much more joyful, and that, hopefully, this is only the beginning.

To Prof. Dr. António Leite for his support and carefully crafted advice given throughout the work developed in this dissertation.

To Prof. Dr. Daniel Alexandre for the advice and assistance in the writing software.

To INESC TEC, specially to the Center of Applied Photonics, and the people that make it for receiving me so well.

To Calouste Gulbenkian Foundation for the funding conceded through the stimulus to scientific research program grant.

To the few but good friends, André Gomes, Miguel Ferreira and João Maia, that throughout the course joined me on this adventure.

Lastly, I would like to thank my family and Joana for their support and company.

Abstract

In this dissertation, femtosecond laser direct writing is explored for the fabrication of several integrated optical devices in bulk fused silica.

The fabrication of integrated optical devices was demonstrated by implementing a transversal writing geometry with a microscope objective focusing the femtosecond laser beam inside the substrate. To improve the quality of the integrated optical devices fabricated, a study on the waveguide and bend loss was made in order to optimize the fabrication parameters. The fabrication of waveguides with propagation loss values very close to the best waveguides reported was obtained.

Using the femtosecond laser writing system, point-by point fabrication of first order uniform Bragg grating waveguides was demonstrated. To achieve this the laser beam modulation was controlled to yield a tight modulation of the refractive index profile along the Bragg grating. Furthermore, by changing the laser beam duty cycle and polarization orientation the spectral behavior of the devices was controlled. By controlled excitation of vertical and horizontal polarization modes an estimate on waveguide birefringence was also made.

The fabrication of directional couplers was studied and the coupling ratio controlled by carefully choosing the interaction length and waveguide separation. Due to waveguide birefringence polarization beam splitters were shown to be possible at several wavelengths. Since the coupling coefficient increases with wavelength, the fabrication of wavelength division (de)multiplexers was shown to be possible for several wavelengths and demonstrated for a particular case.

A method to fabricate symmetrical Y-junctions was devised. An asymmetry inherent to the fabrication process is created in the junction, leading to non uniform power splitting and wavelength dependent behavior. To overcome this limitation an initial arm separation was employed to reduce superposition on the splitting area; an uniform and broadband power splitter was demonstrated.

Several approaches to fabricate multimode waveguides were tested and multimode interference devices fabricated. Simulations were used to design the devices width and length. One-to-four, one-to-three and one-to-two splitting was achieved, thus validating the simulations.

The knowledge gained in the fabrication of the previous devices was later used to fabricate the first ever add-drop multiplexer using this technique. These add-drops were built in a Mach-Zehnder configuration with two Bragg grating waveguides and two 3dB directional couplers. The use of the fabricated device in 100 GHz networks is possible but further development including apodized Bragg gratings and real time trimming can open new possibilities, such as lower inter-channel crosstalk and smaller channel separations.

The knowledge obtained from the fabricated devices opens new doors to more complex integrated optical devices with additional functionalities, as well as optofluidic sensors.

Keywords: femtosecond laser, direct writing, fused silica, integrated optical devices, optical waveguides, s-bends, Bragg gratings, power splitters, directional couplers, y-junctions, mmi, add-drop multiplexer.

Resumo

A escrita direta com laser femtosegundo é explorada nesta dissertação para a fabricação de vários dispositivos óticos integrados em sílica fundida.

A fabricação de dispositivos óticos integrados foi demonstrada através da implementação de uma geometria de escrita transversal utilizando uma objetiva de microscópio para a focagem do feixe laser femtosegundo no interior do substrato. Para melhorar a qualidade dos dispositivos óticos integrados fabricados foi feito um estudo na perda de guias de onda lineares e curvilíneos, nomeadamente das perdas de propagação e acoplamento, de modo a otimizar os parâmetros de fabrico. Os resultados obtidos estão ao nível do estado da arte neste domínio.

A fabricação ponto a ponto de redes de Bragg uniformes de primeira ordem foi demonstrada usando escrita com laser femtosegundo; a modulação do feixe laser foi controlada de modo a produzir uma modulação periódica do índice de refração ao longo da rede de Bragg. O comportamento espetral dos dispositivos foi controlado alterando o *duty cycle* e orientação da polarização do feixe de escrita. A birrefringência dos guias de onda foi caracterizada pela excitação controlada dos respetivos modos ortogonais.

A fabricação de acopladores direcionais foi estudada e o rácio de acoplamento controlado cuidadosamente através da escolha do comprimento de interação e separação entre guias de onda. Devido à birrefringência dos guias de onda foi demonstrado ser possível a fabricação de divisores de polarização a vários comprimentos de onda. Dado que o coeficiente de acoplamento aumenta com o comprimento de onda é possível a fabricação de (de)multiplexadores de comprimento de onda, sendo que um dispositivo foi demonstrado para um caso em particular.

No fabrico de junções Y surge uma assimetria na junção, levando à divisão não uniforme de potência e ao comportamento dependente do comprimento de onda. Neste trabalho foi idealizado e implementado um método de fabrico que permite uma melhoria do desempenho dos dispositivos fabricados; a técnica baseia-se na separação inicial dos braços para reduzir a sobreposição na região da junção. Com esta modificação obtém-se divisores de potência uniformes e com uma grande largura de banda.

Foram testadas várias formas de fabricar guias de onda multimodo, e, com isto, foram fabricados dispositivos de interferência multimodal. Para determinar a largura e o comprimento dos dispositivos recorreu-se a simulações BPM, tendo sido obtidos divisores $1 \times N$ (N=2,3,4), validando assim as simulações teóricas.

O conhecimento e a experiência adquirida na fabricação dos dispositivos anteriores foi utilizada na fabricação de um multiplexador *add-drop*, baseado numa configuração de Mach-Zehnder, usando duas redes de Bragg e dois acopladores direcionais de 3 dB. O dispositivo fabricado pode ser aplicado em redes de 100 GHz de separação entre canais, mas o futuro desenvolvimento de redes de Bragg apodizadas e o ajuste de fase em tempo real pode permitir novas possibilidades, tal como um *crosstalk* menor e menor separação entre canais.

Em conclusão, neste trabalho foram demonstrados resultados ao nível do estado da arte no que diz respeito aos blocos fundamentais necessários para desenvolver dispositivos em ótica integrada; a possibilidade de desenvolvimento de dispositivos complexos baseado em processos de alta resolução espacial ficou demonstrada através da implementação de dispositivos cujos resultados não se encontram reportados na literatura.

Palavras-chave: laser femtosegundo, escrita direta, sílica fundida, dispositivos óticos integrados, s-bends, redes de Bragg, divisores de potência, acopladores direcionais, junções-y, MMI, multiplexador *add-drop*.

Contents

List of Tables

List of Figures

List of Acronyms

Acousto-optic modulator - AOM
Amplified spontaneous emission - ASE
Beam Propagation Method - BPM
Bragg grating waveguides - BGWs
Dicroic mirror - DM
Fiber Bragg gratings - FBGs
Flame hydrolysis deposition - FHD
Multimode interference - MMI
Numerical aperture - NA
Optical add-drop multiplexer - OADM
Optical spectrum analyzer - OSA
Planar Lightwave Circuit - PLC
Polarization maintaining - PM
Reactive ion etching - RIE

Chapter 1

Introduction

Today’s society relies heavily on optical technologies for many aspects of human life. Communication is, for instance, one of those aspects where the invention of optical fibers has severely impacted the way information is transmitted around the world. While optical fibers have become the main component of the world’s communication infrastructure, integrated optical devices have also found many important applications, enabling optical processing and optical sensing, with the sturdiness and density of integrated systems.

Since the theoretic foundation of light amplification by stimulated emission of radiation, proposed by Albert Einstein in 1917, a very large effort was directed towards the demonstration of the first laser, in 1960. Nowadays lasers are used as a tool in many applications, such as industrial material processing, where lasers are used for heat treating, cutting, welding, marking, and cleaning; scientific experiments, in spectroscopic, interferometric and astronomical measurements; medical applications, for eye and cosmetic surgery, and as a cutting and cauterization tool; military, as a weapon, defensive countermeasures, and target guiding; along with many other applications where high coherence and/or high optical intensities are required.

Photonics technologies have many advantages when compared to electrical based communication and sensing methods. For example, optical components can usually be deployed in environments hazardous to electronic equipment. Their immunity to electromagnetic interference makes them suitable for use in high power environments, while their robustness makes them great for extreme pressure (hundreds of MPa) or extreme heat (around 1000ºC) environments. With the correct dielectric materials integrated optical devices can also be used in ionizing radiation environments, such as in space applications or nuclear power plants.

Several techniques enable the fabrication of integrated optical circuits. Flame hydrolysis deposition and reactive ion etching are the industry standard techniques for the fabrication of planar lightwave circuits, since this method produces the best results with propagation losses as low as 0.017 dB/cm [1]. Unfortunately, the fabrication of devices with these techniques require multiple steps, masks, and a clean room environment. To avoid this femtosecond laser direct writing can be used [2]. Femtosecond laser direct writing is highly flexible regarding the material, as long as it is transparent at the writing wavelength, with devices being reported in glasses, crystals, and even polymers [3, 4, 5] with losses as low as 0.12 dB/cm [6]. The main advantages of this technique are its true 3D writing capabilities that enable new geometries, feature that is impossible in lithographic (planar) techniques, and the high writing resolution inherent to the nonlinear absorption process.

Since the discovery of induced refractive index modification on transparent materials, by femtosecond laser exposure, many devices have been demonstrated, including waveguides [7], Bragg grating waveguides [8], directional couplers [9], Y-junctions [10], multimode interference devices [11], and integrated lasers [12]. The lab-on-a-chip concept, where waveguides and micro-fluidic channels are integrated, has also grown with this technique. Here optical and fluidic components are produced by the same process, where a HF bath is used to etch the micro-fluidic channels selectively due to the laser induced anisotropy. These monolithic chips can, depending on the purpose, be used for sensing or manipulation of biomolecules and cells [13, 14, 15, 16]. Another possibility that arose with femtosecond lasers is the photopolymerization for three-dimensional microfabrication. Polymerization in the photosensitive material is caused by nonlinear absorption of the focused laser pulses. This method allows, therefore, the fabrication of photonic crystals and even microneedles for drug delivery [17], among other things.

The objective of this thesis is to study and fabricate optical circuits and devices with the femtosecond laser direct writing technique, for optical communication systems and, in the future, sensing. The material of choice used in this thesis is bulk fused silica glass to ensure optical devices with good optical properties. Previous knowledge in waveguide and segmented waveguide writing is explored for the fabrication of low loss waveguides and tunable uniform Bragg grating waveguides. Other optical circuits building blocks are also investigated and fabricated, such as low loss S-bend waveguides, directional couplers, and multimode interference devices. In addition, a new junction fabrication method is proposed and the fabrication of broadband Y-junction devices demonstrated. To finish, several building blocks are assembled together to create, for the first time using this technique, an add-drop multiplexer.

Chapter 2

Background

In this chapter different fabrication techniques and physical concepts are presented. Femtosecond laser direct writing is confronted with planar lightwave circuit technology and both advantages and disadvantages are discussed, as well as the waveguide fabrication methods. The interaction of the femtosecond laser pulses with the material is then explained and the different material modification regimes reviewed. The propagation of the writing beam through the material is analyzed in order to understand the spatial distribution of the energy density in the focal volume.

2.1 Fabrication of Integrated Optical Devices

The common fabrication techniques employed in the fabrication of planar lightwave circuits were borrowed from the semiconductor industry and involve often deposition of dielectric layer and photolitographic steps, together with dry-etching processing techniques. This techniques are limited to planar geometries due to the nature of the processes. The discovery of femtosecond laser direct writing applied to transparent materials enabled maskless high resolution three-dimensional fabrication of integrated optical devices.

2.1.1 Planar Lightwave Circuit Technology

Planar lightwave circuits using silica-based optical waveguides are fabricated on silicon or silica substrates by, typically, multi-step flame hydrolysis deposition (FHD) and reactive ion etching (RIE), as shown in figure 2.1. In FHD, $SiCl_4$ and $GeCl_4$ vapors are sent into an oxyhydrogen burner where SiO_2 and GeO_2 soot are produced as reaction products. To form the undercladding and core layers silica and GeO_2 rich silica soot are deposited, respectively. After deposition, the wafer with these two porous glass layers is heated to high temperatures for consolidation. The devices core ridge structures are then fabricated by photolithography and RIE. Finally, FHD is used again to cover the core ridge structures with a silica overcladding and consolidation is made for the last time.

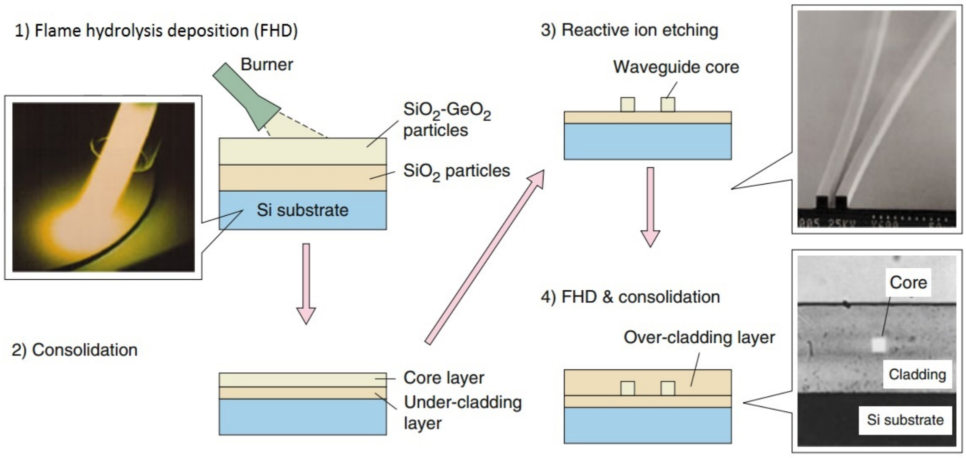

Figure 2.1: Fabrication steps for producing planar lightwave circuits in glass [18].

This method is a well-established and mature fabrication technique capable of producing optical devices with excellent performance. Propagation loss as low as 0.017 dB/cm have been demonstrated, with bent waveguides with curvature radius of less than 2 mm being achievable by adjusting the refractive index difference between core and cladding [1]. With these specifications the fabrication of optical devices for telecom applications is highly attractive. Unfortunately, this method is restricted to specific glasses and rectangular cross-sectional waveguides in planar geometries, and employs RIE which is a time consuming technique.

2.1.2 Femtosecond Laser Direct Writing

When a beam originated from a regular laser is focused on a transparent material such as glass nothing except transmission, scattering, and linear absorption occurs. However, when the regular laser is swapped by a femtosecond laser, the intensity at the beam focus can be on the order of 10 TW/cm^2, intensity at which nonlinear absorption starts to be relevant. This nonlinear absorption is, as opposite to linear absorption, localized as can be seen in figure 2.2.

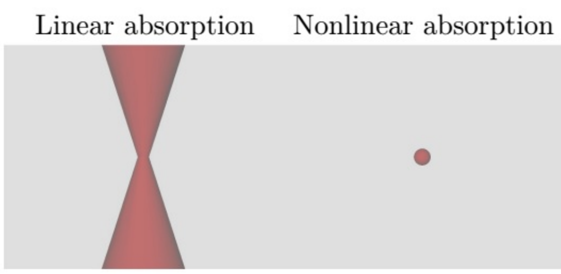

Figure 2.2: Comparison between linear absorption, produced by a continuous wave laser (or long pulsed light source) in a photosensitive material, and nonlinear absorption produced by an ultrafast laser focused in a transparent material [19].

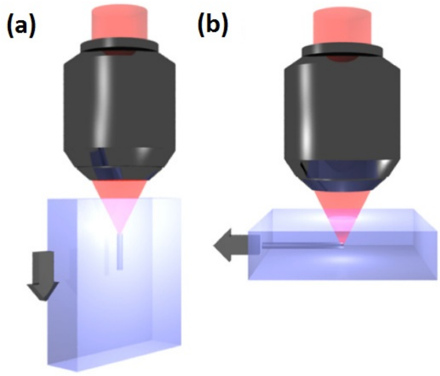

Figure 2.3: Longitudinal (a) and transversal (b) writing configurations for integrated optical devices fabrication in transparent materials. Arrows indicate substrate movement direction [23].

Depending on the material and writing parameters the absorption process may originate voids or structures with a positive/negative refractive index modification. Structures with a positive refractive index modification are required to guide light by total internal reflection. These can be fabricated by translation of the material relative to the beam focus with computer controlled stages.

Femtosecond laser direct writing has clear advantages over the planar lightwave circuit technology, namely the absence of masks and a clean room environment, the high flexibility regarding the material, it is a single step high resolution process, and has a true 3D writing capability that enables new geometries. Several low loss waveguides were reported in glasses, with the lowest propagation loss obtained at 1550 nm being 0.12 dB/cm [6] for multiple scans and 0.2 dB/cm [7] for a single scan. Waveguide writing was also reported in polymers, such as PMMA [5], and crystals [20]. Refractive index modification by femtosecond laser direct writing is on the order of $\sim 10^{-3}$, and as such the minimum bend curvature radius is large, due to the low confinement.

There are two possible writing configurations for the fabrication of integrated optical devices in planar substrates. In the longitudinal configuration the substrate moves along the direction of beam propagation (see figure 2.3 (a)) allowing the fabrication of waveguides with a cylindrical cross-section. However, it also has the huge disadvantage of limiting the length of the waveguides to the objective working distance (usually some millimeters). Another way of fabricating waveguides with this configuration is by using a low numerical aperture objective and high beam power to obtain filamentation. Filamentation arises from self focusing, due to the optical Kerr effect, and self-defocusing, from the plasma created, allowing the fabrication of waveguides without requiring substrate translation [21, 22].

For the transverse writing configuration the substrate moves perpendicularly to the beam direction, as seen in figure 2.3 (b). In this case the writing is only limited by the depth of the waveguide (due to the objective working distance), while the length of the waveguide is only determined by the stages employed. The main disadvantage is that the cross section of the waveguides fabricated is no longer symmetrical (at least not without beam shaping [24, 25] or heat accumulation [7]), but rather elliptically shaped [25, 26]. This lack of symmetry is due to the depth of focus ($2z_R$) being larger than the spot size ($2\omega_0$) by a factor of $\frac{2z_R}{2\omega_0} = \frac{n}{NA}$, where n is the refractive index of the medium and NA the numerical aperture of the microscope objective. In this dissertation a transverse configuration was used and, since the objective chosen has a $NA = 0.55$, a factor of $\frac{n}{NA} \approx 2.65$ is obtained. To make this factor equal to one oil immersion objectives (with a higher NA) can be used at the cost of reduced working distance.

2.2 Interaction of Femtosecond Laser Pulses with Transparent Materials

Visible and near-infrared laser radiation have insufficient energy to be linearly absorbed by transparent dielectric media due to their higher bandgap energy. However, with the developments in laser technology, peak intensities on the order of $10\ TW/cm^2$ can now be achieved by focused femtosecond laser pulses. Such peak intensities result on the nonlinear absorption of the beam by the medium which translates to a localized absorption of the energy at the focal volume. This nonlinear photoionization can start by tunneling and/or multiphoton ionization, depending on the laser frequency and peak intensity, which will then seed avalanche photo-ionization [27]. Despite tunneling and multiphoton ionization being highly dependent on bandgap energy, the writing intensity threshold does not behave the same way, since avalanche photoionization depends linearly with intensity [28]. Due to this fact, femtosecond laser direct writing can be applied to a broad variety of transparent materials.

2.2.1 Free Electron Plasma Formation

Multiphoton ionization occurs by the simultaneous absorption of multiple photons by a valence electron, as seen in figure 2.4 (a). Excitation is achieved when $mh\nu > E_g$, where m is the number of photons absorbed, ν the light frequency, and E_g the bandgap. This process is dominant at lower intensities and higher light frequencies because less photons are required to cross the bandgap. At higher intensities and lower light frequencies tunneling ionization becomes dominant because the band structure is distorted until electrons can make direct band to band transitions by tunneling, as seen in figure 2.4 (b). The transition between both processes is described by the Keldysh parameter [29]:

$$\gamma = \frac{\omega}{e}\sqrt{\frac{m_e c n \epsilon_0 E_g}{I}}, \tag{2.1}$$

where ω is the laser frequency, I is the laser intensity at the focus, m_e is the effective electron mass, e is the electron charge, c is the speed of light, n is the refractive index of the material, ϵ_0 is the permitivity of free space, and E_g is the band gap. When $\gamma \ll$

1.5 ($\gg 1.5$) tunneling (multiphoton) ionization dominates the process, but when $\gamma \approx 1.5$ photo-ionization is a combination of both processes. In the case of fused silica $\gamma \approx 1$, and as such nonlinear ionization is a combination of both tunneling and multiphoton ionization.

Regarding avalanche photoionization, the process can be seeded by thermally excited impurities, defect states, or previous photoionization processes [30]. Since electrons in the conduction band can still absorb photons the conduction band electron's energy will increase, as seen in figure 2.4 (c). After several photons are absorbed the energy of a conduction band electron can exceed the conduction band minimum by more than the band gap of the material enabling the promotion of a valence electron to the conduction band, resulting in two electrons at the minimum of the conduction band. As long as there are electrons in the conduction band, and energy being supplied by the incoming beam, this process can repeat itself, thus the name avalanche photoionization.

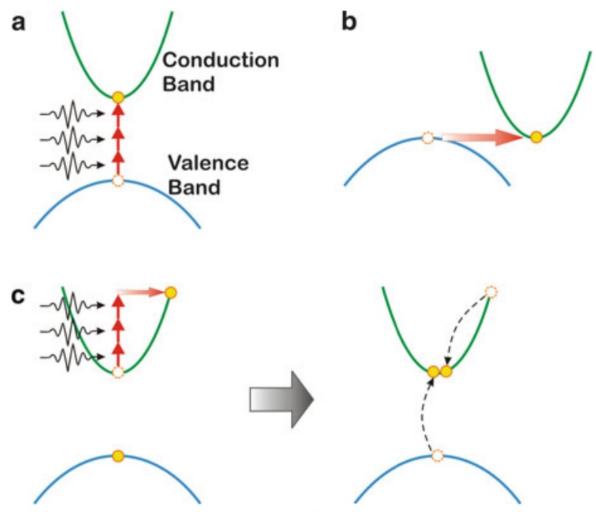

Figure 2.4: Nonlinear photoionization processes underlying femtosecond laser machining. (a) Multiphoton ionization, (b) tunneling ionization, and (c) Avalanche ionization: free carrier absorption followed by impact ionization [31].

Since for femtosecond pulses absorption occurs faster than the energy transfer to the lattice (on the order of 10 picoseconds [27]) the sample heating is decoupled from the pulse absorption, meaning that the avalanche photoionization is only seeded by nonlinear photoionization. A plasma forms as the density of electrons grows, and the absorption of the incident beam increases. Since shorter pulses need less energy to achieve the same peak power, and only the nonlinear photoionization processes can seed the avalanche photoionization, a higher writing resolution can be achieved.

2.2.2 Electron Relaxation and Dielectric Modification

The processes discussed previously, followed by the transfer of energy to the lattice, are the cause for the material modifications. However, the mechanisms for material modification are not yet completely understood. The material modification is highly dependent on the writing parameters and material used (see figure 2.5), but generally two outcomes can be expected: for lower intensities an isotropic refractive index change is obtained [32], while for higher intensities micro-explosions take place, creating empty voids [33, 34]. Reported work also demonstrated that, for fused silica, nanogratings within the waveguide appear at intermediate writing intensity with a direction dependent on the beam polarization, as seen in figure 2.6, causing a birefringent modification of the refractive index [35, 36]. It is important to notice that the refractive index modification is attributed to glass densification, with an index difference of the order of that found in standard optical fibers (around 10^{-3} [7, 37, 38, 20, 39, 40] and up to 10^{-2} [41]).

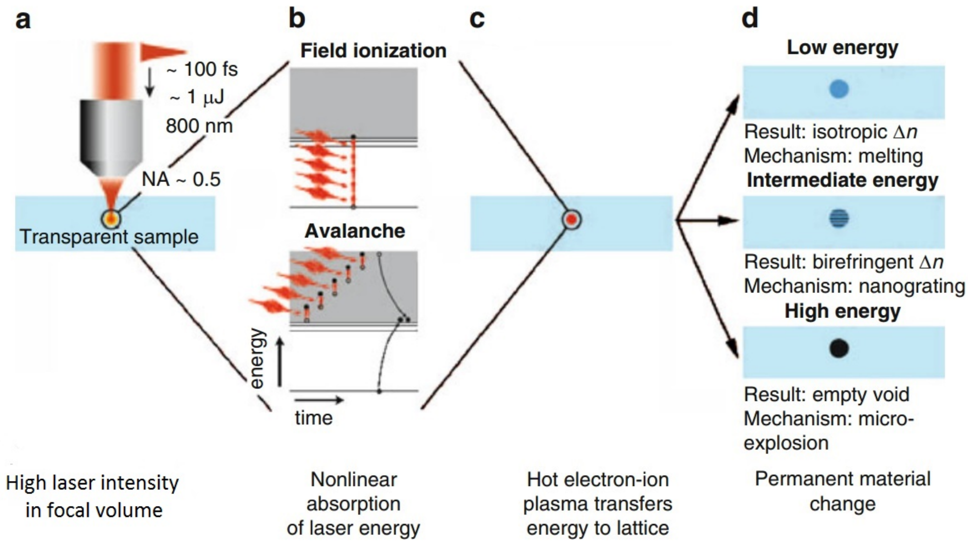

Figure 2.5: Illustration of the interaction physics of focused femtosecond laser pulses in bulk fused silica. (a) The laser is focused below the sample surface resulting in a high intensity in the focal volume. (b) The energy is nonlinearly absorbed and a free electron plasma is created by multiphoton/tunneling and avalanche photoionization. (c) The plasma transfers its energy to the lattice on a ~10 ps time scale resulting in one of three types of permanent modification (d): isotropic refractive index change at low pulse energy, sub-wavelength birefringent nanostructures at moderated energy (regime used in this thesis) and empty voids at high pulse energy [42].

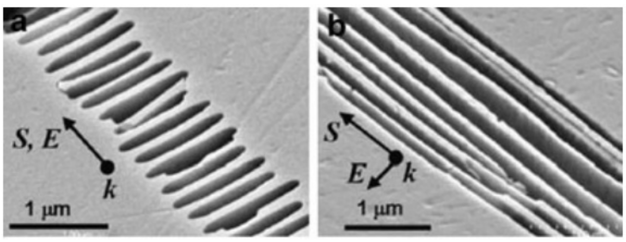

Figure 2.6: SEM image of nanogratings formed at 65 μm depth (sample cleaved and polished at writing depth) with polarization parallel (a) and perpendicular (b) to the scan direction [43].

2.3 Propagation of Gaussian Laser Beams

Knowledge on the propagation behavior of a beam being focused in a material is key to understand the material modification. In this subsection several linear and nonlinear aspects are taken into account.

2.3.1 Linear Propagation

Usually, the spatial intensity of a femtosecond laser beam is well described by the paraxial wave equation. However, to drive nonlinear absorption, microscope objectives are commonly used to focus the beam to a micrometer sized spot, which may cause spherical and chromatic aberrations that are not accounted in this model. If aberrations are neglected the intensity distribution of the Gaussian beam can be well approximated by:

$$I(\rho, z) = \left(\frac{w_0}{w(z)}\right)^2 exp\left(-\frac{2r^2}{w^2(z)}\right), \tag{2.2}$$

where r is the radial distance given by $r = \sqrt{x^2 + y^2}$, z the axial distance from the beam waist, w_0 the waist radius, and $w(z)$ the waist radius along the beam propagation direction. The diffraction limited minimum waist radius is given by:

$$w_0 = \frac{M^2\lambda}{\pi NA}, \tag{2.3}$$

where M^2 is the beam quality factor, NA the microscope objective numerical aperture, and λ the free space wavelength. The waist radius along the beam propagation direction is given by:

$$w(z) = w_0\sqrt{1 + \left(\frac{z}{z_0}\right)^2}, \tag{2.4}$$

where the Rayleigh range, z_0, is, inside a material of refractive index n, given by:

$$z_0 = \frac{M^2 n\lambda}{\pi NA^2}. \tag{2.5}$$

For the beam wavelength and objective used (λ=515 nm and NA=0.55) a waist radius of 0.38 μm is obtained at the focus with a Rayleigh range of 1.0 μm. For a more profound analysis check reference [44].

As was already said spherical and chromatic aberrations are not taken into account in this model. This means that a deviation from the Gaussian intensity distribution can cause equations 2.3, 2.4 and 2.5 to be no longer valid. Chromatic aberrations are originated by the dispersion characteristics of the objective, where the lens fails to focus all wavelengths to the same convergence point. Since the laser used in this dissertation has a bandwidth around 9 nm the chromatic aberrations are negligible. Regarding spherical aberrations, these defects occur due to the increased refraction of light rays that strike the lens near its edge, in comparison with those near the centre, failing to converge to the same point. This problem arises from spherical lenses and can be reduced or even eliminated by employing an aspherical lens. Unfortunately, spherical aberrations are also introduced by the index mismatch at the air-glass interface when writing waveguides inside fused silica. The spherical aberrations are more pronounced for higher NA objectives, as can be seen in figure 2.7, and have a strong dependence in depth [45]. This problem was not solved in this dissertation but can be avoided by employing oil-immersion objectives or dry objectives with collars that enable spherical aberration correction at different focusing depths.

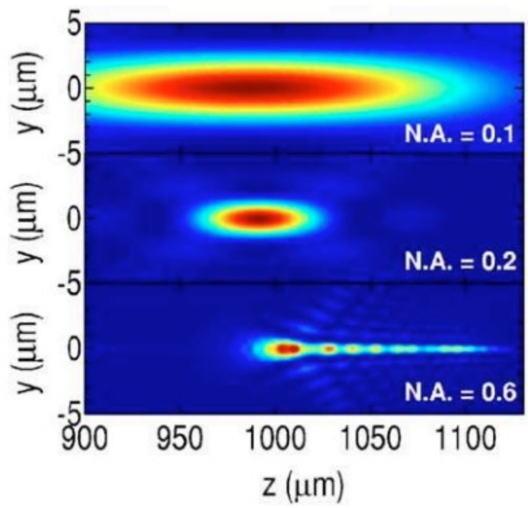

Figure 2.7: Intensity distribution of 800 nm wavelength laser focused 1 mm below the surface of glass with NA=0.1, 0.2 and 0.6 [45].

A parameter that is fundamental in the fabrication of waveguides is depth. Due to refraction between the air-glass interface (see figure 2.8) a change in the objective height does not mean the focus height changing accordingly. Using Snell's law a rough estimate of the waveguide's depth, z', can be obtained by knowing the change in objective height, z, since:

$$z' = z\frac{n^{\shortparallel}}{n^{\shortmid}}\sqrt{1+\frac{(n^{\shortparallel 2}-n^{\shortmid 2})\,NA^2}{(n^{\shortparallel}n^{\shortmid})^2-(n^{\shortparallel}NA)^2}}. \tag{2.6}$$

For the microscope objective used in this dissertation (NA=0.55) the following approximation can be used:

$$z' \approx z\frac{n^{\shortparallel}}{n^{\shortmid}}, \tag{2.7}$$

with an error of 11 % to the exact solution.

The temporal duration of the pulse can also be affected by dispersion from mirror reflections and transmission in optical elements of the system. This pulse broadening

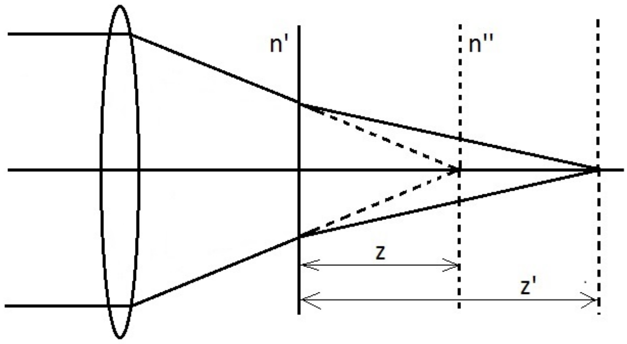

Figure 2.8: Schematic of a beam being focused inside fused silica through air.

affects the peak power and thus modifies the interaction of the pulse with the material at the focus. Fortunately, temporal broadening can be neglected since relatively high pulse durations are being used ($\sim$250 fs).

2.3.2 Nonlinear Propagation

When light propagates through a dielectric material its electric field interacts with electric dipoles and induced electric dipoles. The material response to this electric field can be observed in the material polarization. Fused silica is a centrosymmetric material ($\chi^{(2)} = 0$), and as such the polarization vector is given by:

$$P = \epsilon_0 \left[\chi^{(1)} + \frac{3}{4}\chi^{(3)} \mid E \mid^2 \right] E, \tag{2.8}$$

where $\chi^{(i)}$ is the i-th order susceptibility and E is the electric field vector. Higher orders were discarded due to the small contribution. From this equation the refractive index can be found as:

$$n = \sqrt{1 + \chi^{(1)} + \frac{3}{4}\chi^{(3)} \mid E \mid^2} = n_0 + n_2 I, \tag{2.9}$$

where $n_0 = \sqrt{1 + \chi^{(1)}}$ is the linear refractive index, $n_2 = 3\chi^{(3)}/4\epsilon_0 c n_0^2$ is the nonlinear refractive index, and $I = \epsilon_0 c n_0 \mid E \mid^2 /2$ is the light intensity.

Considering for instance an intense Gaussian beam propagating through a material, according to the previous equation the refractive index will change introducing an intensity dependent spatial phase modulation which will alter the shape of the wavefront and hence the focusing properties. Since n_2 is positive for fused silica the refractive index at the center of the beam will be larger than at the wings, effectively creating a lens that focuses the beam. This process is called self-focusing and it is a third order nonlinear optical process that arises from the optical Kerr effect. A curious aspect of self-focusing is that it depends on power rather than intensity, where the critical power for self-focusing to dominate diffraction is described by:

$$P_{crit} = \frac{3.77\lambda^2}{8\pi n_0 n_2}. \tag{2.10}$$

For fused silica $n_0 = 1.4615$ and $n_2 \approx 3 * 10^{-20}\ m^2/W$, at $\lambda = 515\ nm$. These values mean a critical power of approximately 0.9 MW, which is approximately the peak power obtained while writing waveguides. This raises the problem of how to prevent self-focusing from occurring until the focus is reached. Despite self-focusing depending on power rather than intensity, it is still linked to intensity. If the beam is wide and intensity low, or, in other words, if the beam is tightly focused, nothing will happen until the focus is reached because the intensity is not sufficient to nonlinearly ionize the material. A problem related to this process is obtained when low NA objectives are used. In this case higher powers are required meaning that self-focusing occurs before the focus, nonlinearly ionizing the material and producing a plasma. The plasma decreases the refractive index acting as a diverging lens that counters self-focusing. This balance leads to filamentary propagation, resulting in elongated structures undesired in transversal writing. A more in-depth discussion on self-focusing can be seen in references [46, 47].

Chapter 3

Laser Writing, Device Characterization and Sample Preparation

In this chapter the methods used for the fabrication and characterization of integrated optical devices are presented, as well as sample preparation.

This chapter begins, in section 3.1, with a description of the femtosecond laser system, its operation and alignment procedures. In section 3.2 the characterization setups and methods for insertion loss, coupling loss and propagation loss measurements are described. The grating characterization setup is also discussed. In section 3.3 sample preparation, polishing and cleaning procedures are explained.

3.1 Femtosecond Laser Direct Writing System

In this section the femtosecond laser system main parameters are described. The writing setup is then fully explained as well as its alignment. Since light suffers loss as it travels along the setup the total loss of the system is investigated, so that the real writing pulse energy at the sample is known.

3.1.1 Writing Setup

The laser system used in this thesis is a Satsuma HP fiber amplified laser, capable of delivering pulses of 250 fs, at 500 kHz (270 fs, at 10 MHz), with a polarization ratio of 1200:1. Due to an external modulator the repetition rate ranges between a single shot and up to 10 MHz. By using the oscillator output a repetition rate of 40 MHz is also possible. This system is able to produce radiation with a central wavelength of 1030 nm and then generate second harmonic, at 515 nm, and third harmonic, at 343 nm, with maximum average powers of 10.5, 5.5, and 1.94 W, respectively. This means that the maximum

Parameters	Specifications	
Center Wavelength	1030 nm	515 nm
Repetition Rate	0.5-10 MHz	500 kHz
Bandwidth FWHM	8.4-9.5 nm	-
Polarization Contrast Ratio	1200:1	-
Beam Quality, M^2 (X,Y)	(1.11,1.14)-(1.11-1.13)	(1.12-1.13)
Beam Diameter (1/e^2) (X,Y)	(2.17,2.30)-(2.14,2.35) mm	(1.97,2.08) mm
Beam Divergence (X,Y)	(0.94,1.11)-(0.97,1.17) mrad	(0.69,0.75) mrad
Pulse Duration	250-270	-
Maximum Average Power	10.5-10.8 W	5.5 W
Maximum Pulse Energy	21-0.11 μJ	11 μJ

Table 3.1: Satsuma HP fiber amplified laser specifications.

energy per pulse for fundamental, second harmonic and third harmonic is, at 500 kHz, 21, 11, and 3.88 μJ, respectively. The key characteristics are summarized in table 3.1.

The laser power can then be controlled internally by the laser external modulator, however, for an easier control, an external motorized attenuator unit from Altechna (see figure 3.1) is used [48]. This unit works by having two thin film polarizers aligned at the Brewster angle. The polarizers will only reflect s-polarized light while transmitting p-polarized and a small percentage of s-polarized light. The power will be controlled via the rotation of a $\lambda/2$ waveplate that rotates the linear polarization of the incident laser beam. The polarization rotation changes the ratio between s and p-polarized laser beam components and thus the power that will be reflected or transmitted. Depending on the characteristics desired for the laser beam, p or s-polarization can be selected at the exit of the attenuator. P-polarization gives maximum transmission (more power) while s-polarization offers a higher purity beam polarization contrast.

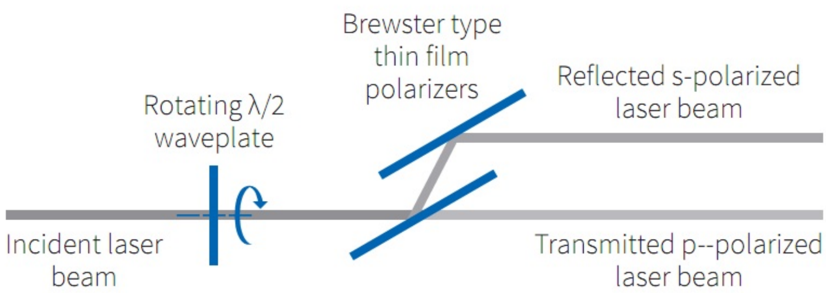

Figure 3.1: Watt Pilot operating principle [48].

After the attenuator the beam is directed to the beam delivery system (see figure 3.2) by mirrors. Since femtosecond pulses are being used one must take into account the damage threshold and dispersion of the mirrors, due to the beam bandwidth and pulse time duration of approximately 250 fs. The mirrors used (Altechna 1-OS-2-0254-5-[1K00-GDD]) have low group delay dispersion (-10 $fs^2$to 10 fs^2 at the designed bandwidth) and high damage threshold at the writing wavelength (515 nm).

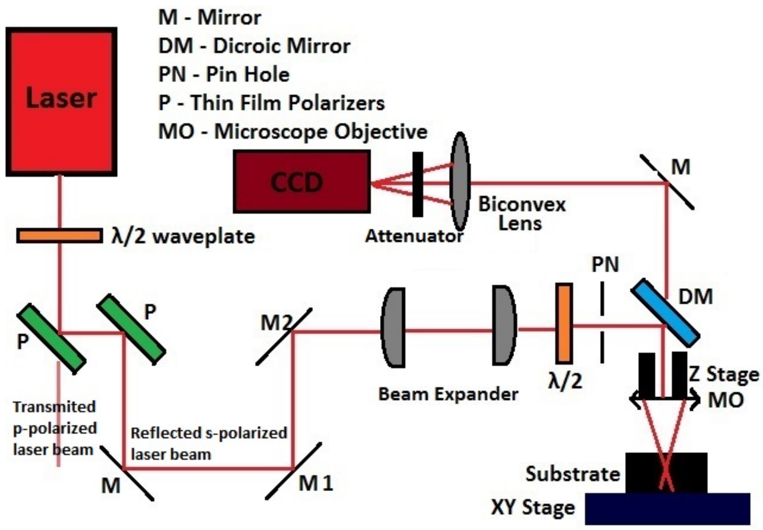

Figure 3.2: Experimental setup for femtosecond laser direct writing, with visualization of the writing process and 3D capability.

From here the laser beam is directed to a beam expander.

The beam expander is composed of two planar-convex lenses with a focal length of 35 and 80 mm, and it is used to increase the width of the beam (magnification $m = \frac{f_2}{f_1} \approx 2.29$). With this the microscope objective is filled and as a consequence the effective numerical aperture is increased, resulting in the smallest focusing spot possible for this lens [49]. One problem that could arise for this expander geometry is that the beam is being focused in air, which for high enough power can create a plasma. To solve this problem, this configuration should be used in vacuum or a Galilean beam expander could be employed. However, since we have relatively low powers, a Keplerian beam expander is sufficient. Spatial filtering of the beam (that is not employed in our setup) could also be employed, by placing a pin-hole at the focus to remove the spatial intensity fluctuations from the Fourier plane [50].

The beam then passes by a $\lambda/2$ waveplate that controls the polarization of the writing beam. Next, the beam passes through a variable circular aperture to control its diameter when entering the objective and to also clean the external part of the beam from its imperfections. The beam then reflects on a dicroic mirror (selected for the writing wavelength of 515 nm) into the microscope objective that will focus the beam inside the substrate. The microscope objective being used for the writing is a New Focus 5722 A-H aspheric lens with a numerical aperture (NA) of 0.55 and a 2.9 mm working distance. An aspheric objective has to be used to reduce or even eliminate spherical aberrations that will affect the depth profile of the beam, translating into an elongated depth modification of the refractive index.

To enable 3D writing there are 3 stages (X, Y and Z). The X and Y horizontal stages consist of two Aerotech ABL10100-BL Air-Bearing Linear Stage (with a closed-loop resolution of 0.5 nm, repeatability of 50 nm, maximum travel of 100 mm and maximum speed of 300 mm/s) placed orthogonally on top of each other and mounted on the optical table. The Z vertical stage is mounted on a support and consists of a PI P-725 PIFOC Long-Travel Objective Scanner, with 400 microns of travel and sub nanometer resolution, where the microscope objective is attached. This set of stages is controlled by a C++ program.

For visualization a CCD is present, so that the light that travels through the microscope objective and then is transmitted by the dicroic mirror is focused on the CCD to be imaged. This CCD has two main purposes, visualization of the process and substrate alignment. For visualization of the writing process a LED is used to illuminate the substrate from bellow. For substrate alignment, and to find the substrate surface to use as a reference, the light used is the beam itself since a small portion of the beam is transmitted by the dicroic mirror.

For more information on the fabrication setup check reference [51].

3.1.2 Setup Alignment

The alignment of the system is achieved by following these rather simple steps:

- Assuming that the laser beam propagates parallel to the optical table, after passing through the attenuator, the beam will get to a periscope system that will insert it into the main setup described above. This periscope system is composed of two mirrors oriented at 45 degrees to the beam (working angle of the mirrors) where the beam in between the mirrors necessarily needs to be vertical. The exiting beam into the main setup is horizontal.

- At this point the beam must be hitting mirror 1 (M1). By placing M2 and the dicroic mirror (DM) at 45 degrees the beam should be hitting the substrate holder that is placed on top of the XY stages. It should be noted that this process must be done without the beam expander, $\lambda/2$ waveplate and variable circular aperture since this is a coarse alignment. For a fine alignment a mirror is placed on the bottom of the substrate holder (by doing this we are assuming that the bottom of the substrate holder is parallel to the optical table) and the angle of the mirrors is fine tuned using screws. If after M2 the beam is horizontal only the DM needs to be fine tuned. The perfect alignment corresponds to both optical paths (transmitted and reflected) being the same, so, to fine tune the angle, a circular aperture is inserted temporarily on the exit of the attenuator (maximum distance from the reflecting mirror, to improve alignment) and the angle of the DM adjusted until both beams propagate through the aperture.

- At this point the variable circular aperture described on the setup can be placed, and the alignment checked by simply closing aperture and observing what part of the beam is disappearing first. By readjusting the variable circular aperture position and repeating the process a good alignment should be achieved.

- Then, the $\lambda/2$ waveplate can be inserted. To align it the same process as the mirrors is applied, by checking the reflection of the beam on the surface of the waveplate.
- To insert the beam expander we make use of the plane part of the lenses. With the first lens turned around (planar interface facing laser) we can again check the reflections until both optical paths coincide. By removing the first lens (but leaving the holders) we can do the same to the second. Since the second lens is already in the correct orientation now all we have to do is insert the first lens with its orientation reversed to the previous step. To have the beam exiting the beam expander collimated the distance between the lenses must be adjusted (for a coarse alignment the distance between both lenses is $f1 + f2 = 115mm$), and to verify when the beam is collimated a mirror can be inserted after the beam expander to remove the beam from the setup. With this it is trivial to check if the diameter of the laser beam is changing or not by measuring it at different distances.
- All that was done previously was a part of the alignment process for the microscope objective. By guaranteeing that the beam is perpendicular to the optical table and now that the axis of the microscope objective is parallel to the laser beam we are ensuring optimum conditions for the writing. To align the axis of the microscope objective a mirror is placed on top of its holder and once again the holder is adjusted until the reflected laser beam is coincident with the incoming beam.
- Another alignment that needs to be done on the microscope objective is to center the beam with its center. To do this a paper is placed on the substrate holder at some distance to the objective, to get a bigger view of what is happening, and by closing the variable circular aperture, not to fill the entire objective, a rough center is found. To get a fine alignment the circular aperture is opened and the first part of the beam to disappear from the image is compensated by dislocating the objective. This fine process is repeated several times until there is no noticeable difference.
- All there is left to do now is to align the sample holder, so that the substrate lies parallel to the optical table, and, thus, transversal to the beam. To do this the height of the microscope objective is adjusted, at very low power (so that no ablation occurs at the sample surface), until a spot on the screen is found. This happens because the laser beam is being focused on a surface of the substrate, where a portion of the beam is being reflected and propagating while collimated to the lens that will focus it on the CCD. It is also important to refer that when the focus is not exactly on the interface diffraction rings appear on the CCD. This characteristic is useful for the fine alignment process. So, all there is to do is find the upper surface, since there is more power being reflected, and to position the focus on an edge of the substrate. Then, the substrate is displaced to the opposite edge and the substrate holder height adjusted until the spot is again found. Going to the previous position and adjusting the height of the objective and repeating the process enough times should result

in one axis aligned. Doing the same process in the orthogonal direction enables a fully aligned sample. In case the sample is not perfectly plane the curvature can be measured by measuring how much the objective has to be moved until the spot is again obtained.

3.1.3 Power Control

One of the most important parameters when fabricating integrated optical devices with femtosecond laser direct writing is pulse energy. The pulse energy used to write devices is given by $E_P = P/R$, where P is the power after the microscope objective and R is the pulse repetition rate. Since this measurement is difficult to obtain with the current setup it is vital that the losses of the system are known, so that accurate estimates can be made by measuring the power after the attenuator (which is a much easier thing to do). In figure 3.3 the measured writing pulse energy is plotted as a function of power measured after the attenuator, as well as the respective fitting and system loss. From the figure it is visible that the writing pulse energy grows linearly with power at the attenuator, and that the writing pulse energy is given by:

$$E_P \approx 0.456 P_{att} + 3.38, \tag{3.1}$$

where E_P is the writing pulse energy in nanojoule and P_{att} the power after the attenuator in miliwatt. The average system loss at different powers was 54 %.

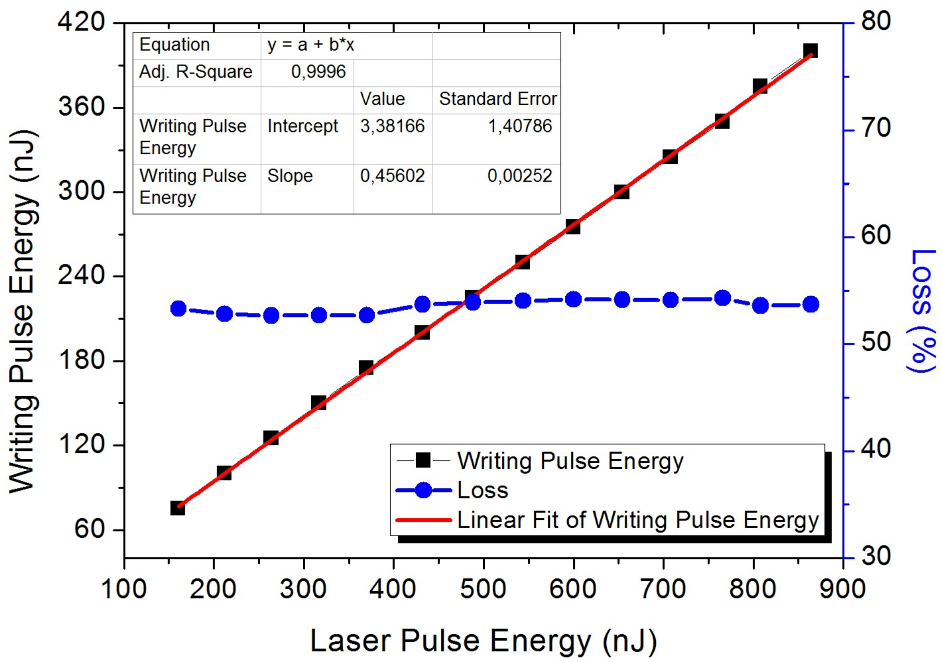

Figure 3.3: Plot of the writing pulse energy as a function of power measured after the attenuator with respective fitting and system loss.

3.2 Characterization of integrated optical devices

This section describes the apparatus and procedure employed for the optical characterization of the produced devices, namely insertion loss, modal profile, and spectral transmission and reflection.

3.2.1 Insertion Loss Measurement

Insertion losses were measured using the setup described in figure 3.4. To characterize integrated optical devices two radiation sources were used, a 632.8 nm diode laser, to easily find when light is being coupled, and a Santec TSL-210V tunable laser, to evaluate the losses at the desired wavelength in the 1550 nm region. Light from these lasers is then inserted into a 90/10 coupler (JDS Uniphase FOC-9010-JDS-FFCCA22PB110) and guided by SMF28 fibers. Two fibers are butt-coupled to the substrate and are used as input, of 90% of the laser light, and output, of the transmitted laser light. Index matching (Cargille series: AA $n_D^{25°C} = 1.458 \pm 0.0002$) is used in both fiber-substrate interfaces to minimize Fresnel reflections, and to increase the accuracy of the measurements. Both fibers are aligned using Elliot Scientific E-2100 precision stages with three degrees of freedom (X, Y and Z), each axis having a piezoelectric adjuster for nanometric resolution. The substrate is also placed in a precision stage, with four degrees of freedom (X, Y, yaw and pitch) to complement the alignment, and hold in place using vacuum. The transmitted light and the other 10% of the laser light are then guided to a Exfo Optical System IQ-203 power meter, where the transmitted light gives us a measurement of the insertion loss, and the 10% of the laser light a reference of the laser power stability.

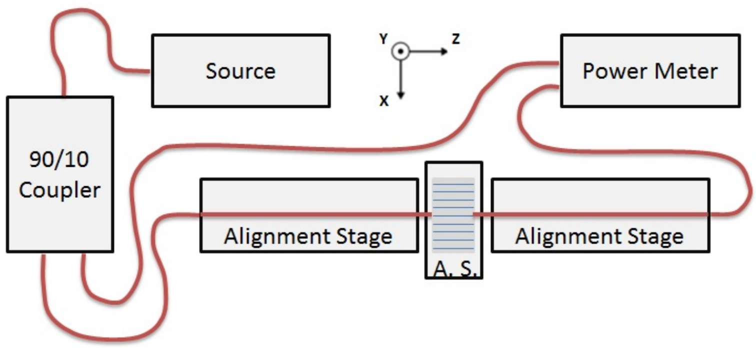

Figure 3.4: Waveguide insertion loss characterization setup.

From this setup the insertion loss is obtained by measuring the laser power directly (P_0), with a patch cord connecting the tunable laser to the power meter, and the transmitted power (P_1). Since the laser power was measured in Watts, formula 3.2 gives us the insertion loss in dB.

$$IL = 10log_{10}(\frac{P_1}{P_0}) \tag{3.2}$$

The method used gives an upper bound of the insertion loss, since Fresnel reflections in both fiber-index matching-waveguide interfaces are not taken into account, and due to the difficulty in aligning both input and output fibers with the waveguide, which always decreases the transmitted power.

To check the 90/10 coupler behavior, both arms were measured. Figure 3.5 shows the power obtained in the 90 % arm as a function of the power at measured in the 10 % arm. From here it is possible to see that the coupler behavior at 1550 nm is linear, with an adjusted R^2 of 1, and that the coupler has a behavior of $\approx 93/7$. Since the power used in the 90% coupler arm, for characterization, was around 1 mW, any shift in laser power can be seen in the reference arm and P_0 rectified. It is however important to refer that the laser behavior with time was quite stable, and only very small power variation was observed.

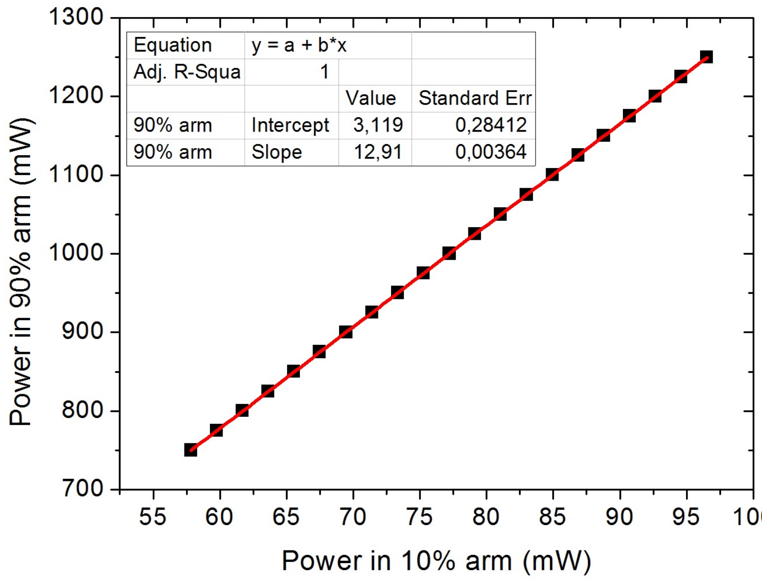

Figure 3.5: Power behavior of 90/10 coupler.

3.2.2 Mode Profile Measurement and Coupling Loss

Coupling loss is defined as the power loss that occurs when coupling light from one optical medium to another. Here coupling loss refers, more specifically, to the power loss from light coupling from an SMF28 to an integrated device, or vice versa. Since index matching is used Fresnel reflections can be neglected. Hence, coupling loss can only be attributed to the modal profile mismatch of the fiber with the integrated devices.

To calculate the coupling losses that exist between the integrated devices and the input/output fibers the waveguide mode diameter has to be measured. To do so, the setup in figure 3.6 was used. This setup is basically the same has the setup in figure 3.4, but, instead of having an output fiber, there is a microscope objective to focus the waveguide output into a CCD camera (Point Grey Research CMLN-13S2M-CS). To reduce background noise and dust falling on the CCD, a tube was screwed to the camera.

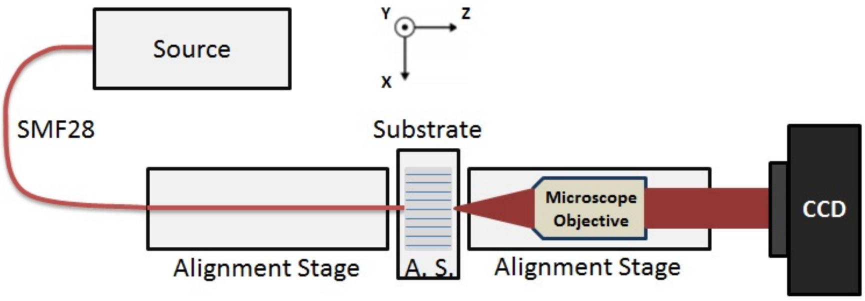

Figure 3.6: Waveguide coupling loss characterization setup.

Regarding the microscope objective, theoretically a higher magnification should be used to increase resolution, however, as seen in figure 3.7 (a), the CCD has different sensitivities for different areas. To solve this issue a 20x microscope objective was employed, and the most uniform uniform area was located (top left in this case) using the Gaussian mode of a SMF28 fiber. From figure 3.7 (b) it is visible that the mode is much better reproduced. Another problem with the CCD is the presence of granularity, but unfortunately this cannot be solved.

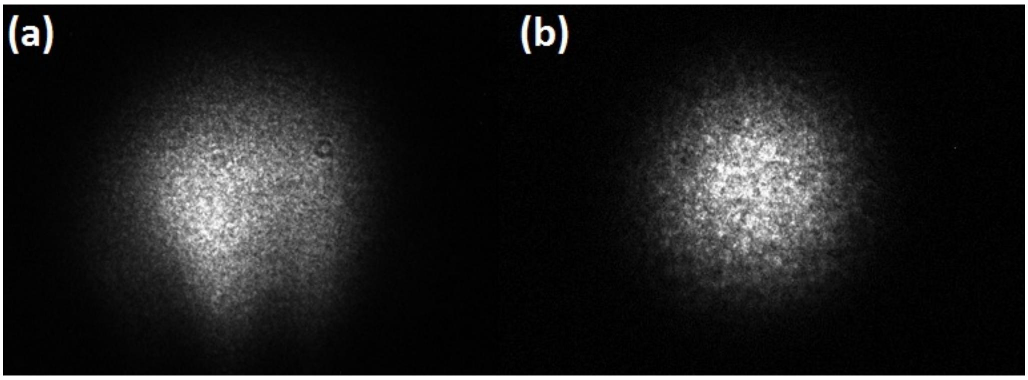

Figure 3.7: SMF28 modal distribution imaged by the CCD at 60x magnification (a) and 20x magnification (b) (cropped image from the top left part of the CCD).

To measure the waveguides mode diameter a comparison between the SMF28 mode diameter (known to be 10.4 μm @ 1550 nm) and the integrated devices mode diameter was made. The integrated devices mode images were taken and the noise present in the CCD removed, by subtraction of the images with the image with the beam blocked. The integrated devices mode diameter and SMF28 mode diameter were then obtained through LaseView, using a Gaussian function for the fit in the X and Y directions.

From here the coupling efficiency between the substrate and the fiber can be estimated by the overlap integral of both modes:

$$\eta = \frac{\mid \int_{-\infty}^{\infty} \Psi_1(X,Y)\Psi_2(X,Y)dXdY \mid^2}{\int_{-\infty}^{\infty} \mid \Psi_1(X,Y) \mid^2 dXdY \int_{-\infty}^{\infty} \mid \Psi_2(X,Y) \mid^2 dXdY}. \tag{3.3}$$

When Gaussian modes are assumed $\Psi_1(X,Y) = Aexp(-(X^2+Y^2)/a^2)$, where "a" is the mode field diameter of the input and output fibers (10.4 μm @ 1550 nm), and $\Psi_2(X,Y) = Bexp(-(X^2/d_X^2 + Y^2/d_Y^2)$, where "$d_X$" and "$d_Y$" are the mode field diameters of the integrated devices in the horizontal and vertical directions respectively (mode field diameters obtained at $e^{-2}o$f the intensity profile). From substitution we arrive to the simplified equation:

$$\eta = \frac{4a^2 d_X d_Y}{(d_X^2 + a^2)(d_Y^2 + a^2)}. \tag{3.4}$$

From coupling efficiency coupling loss (of one fiber-integrated device interface) can be calculated (in dB) by the following equation:

$$CL = 10log_{10}(\eta) \tag{3.5}$$

3.2.3 Propagation Loss

Propagation loss of light in waveguides arises mostly from Rayleigh scattering and absorption. The insertion loss of optical waveguides is described by:

$$IL = 2CL + PL * L, \tag{3.6}$$

where L is the device length, CL the coupling loss, and PL the propagation loss. From this, several approaches are available. The most straight forward technique is based on writing a very long waveguide, so that $PL \approx IL/L$. Since $PL * L$ needs to be much bigger than $2CL$, L needs to be larger for lower propagation losses. However, the maximum travel range of the stages used is 10 cm which, for low propagation loss waveguides with higher coupling loss, means a considerable error.

Another technique bases on the linear behavior of insertion losses with waveguide length. This technique consists on the fabrication of waveguides with different lengths (with the same parameters). From the slope propagation loss would be attainable, and by extrapolation to L=0 coupling losses could also be obtained. However, to have confidence in the data, a large quantity of waveguides would be needed.

To solve this problem, in this thesis the propagation loss of the fabricated waveguides was measured indirectly. First the insertion loss was measured as seen in section 3.2.1, and then the coupling loss was estimated as in section 3.2.2. The propagation loss was then obtained from:

$$PL = \frac{IL - 2CL}{L},$$

where L is the waveguide length.

3.2.4 Grating Characterization

For grating characterization two setups were used, as seen in figure 3.8. The first setup was used to quickly find the Bragg wavelength (discussed in section 5.1) with the reflected signal, while the second was used to characterize the Bragg gratings with a better resolution.

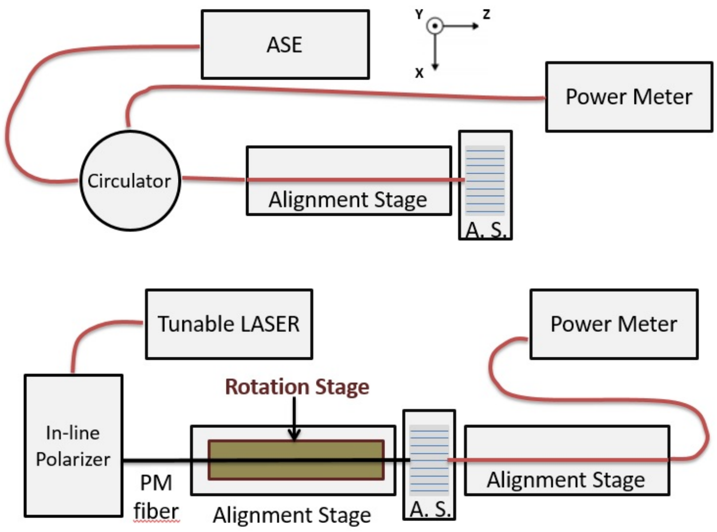

Figure 3.8: Grating characterization setups for a coarse measurement of the Bragg wavelength (top), and a fine measurement of the Bragg grating transmission spectra (bottom).

The first setup is composed of a amplified spontaneous emission (ASE) light source (EXFO IQ-2300), emitting from around 1525 to 1570 nm. The grating Bragg wavelength is then checked using the reflected signal removed by an optical circulator. The detector used was a Ando AQ-6315B optical spectrum analyzer (OSA), capable of measurements from 350 nm to 1750 nm with a 0.05 nm maximum resolution.

The second setup is composed of a tunable laser source (Santec TSL-210V), capable of emitting from 1500 to 1620 nm. To check grating birefringence an in-line polarizer (Thorlabs ILP1550PM-APC) was used to guarantee a linear polarization, and the end of a polarization maintaining (PM) fiber rotated using an ELLIOT MARTOCK rotation stage to analyze horizontal and vertical input polarizations. An SMF28 optical fiber then carried the transmitted signal to an EXFO IQ-1600 power meter.

3.3 Sample Preparation

For better results and repeatability the substrates coupling facets were polished and cleaned. These processes are detailed in the next subsections.

3.3.1 Sample Polishing

To polish the fused silica substrates, in the input and output facets, the substrates had to be fixed to another thick glass plate that provides support. To do this the following steps were taken:

- Both the support glass and substrates were gradually heated, to avoid cracks, at the same time to approximately $150°$ Celsius;
- Logitech ocon-199 plasticized bonding wax was applied to the support glass;
- The first substrate was placed on the support glass and the nonexistence of air bubbles was checked. If there are bubbles at the polishing edge this step has to be repeated;
- The same process can be repeated if more than one substrate is going to be polished;
- The multiple substrate facets that are going to be polished are then aligned to each other to minimize the polishing time, by placing a thin glass vertically with an aligning glass pressing it against the substrate. At this point the stack should look like in figure 3.9;

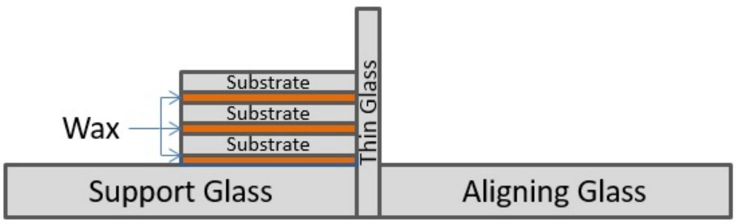

Figure 3.9: Substrates being fixed and aligned for polishing.

- The heating is then turned off for the substrates to cool down slowly (again to avoid cracks);
- When the wax is solid the aligning glass and thin glass are removed.

To polish the exposed facet the following steps were taken:

- The set of substrates with the support glass is placed on the jig with the facets of the substrates facing the polishing plate;
- First Step: Turn the polishing machine on and let the iron plate rotate while dripping polishing fluid (Logitech Silicon carbide Powder, 600 grit) onto it;
  - Place the jig on the polishing machine while it is rotating at 3 rpm, and let the fluid spread on the polishing plate (all of this while avoiding the contact of the substrates with the plate);
  - Let the substrates touch the plate gently to correct the small angle between the substrates and the plate, to avoid chipping. When there is a large surface of the substrates in contact with the plate the substrates can be totally dropped;
  - The plate rotation is then increased to approximately 20 rpm, while having approximately 3 drops of polishing fluid per rotation. At this moment the jig should be also rotating, to ensure a better polishing uniformity;
  - The state of the polishing needs to be checked from time to time until the facet becomes dull and there are no major scratches on the surface. At this moment the first polishing step is complete and the jig can be removed (by first lifting the substrate);
  - Then the jig and substrate have to be thoroughly cleaned with water, to ensure that there is no contamination to further steps (by having larger grains present then those being used to polish);
- Second Step: The jig is now placed on a grooved brass plate while using Logitech Aluminum Oxide (3 micron) polishing fluid and the process is repeated until the substrate gets clear with no scratches;
- Third Step: After another cleaning the jig is placed on an aluminum covered expanded polyurethane polishing pad plate with Logitech SF1 as the final polishing suspension that gives the substrate an optical grade polishing;
- After this last step the plate must be thoroughly cleaned with water so that the polishing suspension (silica) does not dry, damaging the plate.

Since this process is only to polish one of the facets the substrates have then to be rotated and the process repeated for the opposed facet.

3.3.2 Sample Cleaning

To clean the substrates two methods were used, depending on the substrate dirtiness. When the substrate had wax from the polishing a piranha solution was used, instead of a non-polar solvent such as xylene that dissolves the wax but is also carcinogenic. The process used was:

- Add hydrogen peroxide slowly to sulfuric acid, while stirring, until the temperature of the solution increased to approximately 80 degrees Celsius;
- When the temperature is achieved the substrate is submerged for 5 minutes;
- After 5 minutes, the substrate is removed from the piranha solution and submerged in distilled water;
- The substrate is then dried with an N_2 gun, and the next process applied.

When the substrate was dirty from common use (dust, fingerprints, index matching, etc) the process applied was:

- Submerge the substrate in acetone;
- Scrub the substrate with appropriate paper;
- Submerge again the substrate in acetone;
- Since acetone leaves a film the substrate is then submerged in ethanol (acetone solvent);
- Since ethanol leaves a film the substrate is then submerged in water (ethanol solvent);
- To dry the substrate an N_2 gun is finally used.

Chapter 4

Waveguide Fabrication in Fused Silica

In this chapter the results obtained on waveguide fabrication in fused silica substrates are presented. The results were obtained using the setup described in chapter 3, with a laser pulse repetition rate of 500 kHz and a 0.55 NA microscope objective. These parameters were chosen based on past experience on waveguide and grating writing by Luis Fernandes [19] and Diogo Lopes [52].

This chapter begins with an analysis of the waveguides cross-section profile, and its evolution with depth. The optimization of parameters such as laser beam polarization (relative to the writing direction), pulse energy, substrate translation velocity and writing depth is also made in order to minimize waveguide losses. The effects of writing on the border of the substrate are also analyzed. In the end of the chapter the fabrication of S-bend waveguides is discussed and optimized.

The main objective of this chapter is to find the parameters that enable the writing of low loss waveguides, with an optical mode profile that determines relatively low coupling losses to standard optical fibers. This information will then allow the fabrication of several integrated optical devices, as will be seen in chapter 5.

4.1 Background

For light to be guided, a medium with a higher refractive index than its surrounding media should be guaranteed. Waveguides consist of a core with a refractive index n_1 and a cladding with a refractive index n_0, as shown in figure 4.1. The light coupled to the waveguide travels mainly in the core by total internal reflection, however, to have total internal reflection, the following condition should be met:

$$\phi \leq \frac{\pi}{2} - arcsin\left(\frac{n_0}{n_1}\right). \tag{4.1}$$

This angle is related with the accepted cone angle, θ, by:

$$\theta \leq arcsin\left(\sqrt{n_1^2 - n_0^2}\right) \equiv \theta_{max}, \tag{4.2}$$

where θ_{max} is the critical accepted angle for total internal reflection.

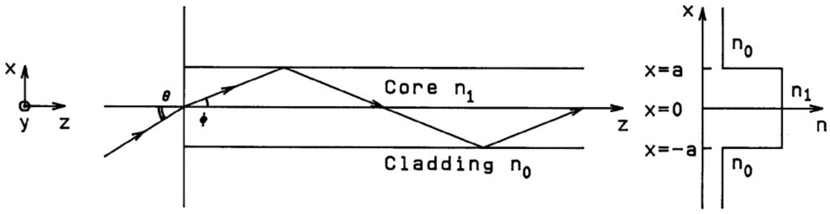

Figure 4.1: Basic structure and refractive-index profile of the optical waveguide [53].

However, despite light being coupled at angles lower than the maximum acceptance angle, light with arbitrary angles may not be able to propagate. This is due to the existence of modes, where the different rays propagating in the core with the same angle have to be in phase.

The background presented here is based on a propagating light rays approach which offers some insight on this matter but lacks the ability to explain more complex concepts. A proper analysis requires solving Maxwell's equations, and, to those willing to invest some time in a more in depth analysis, the following references should be checked [54, 53, 55].

4.2 Waveguide Cross-Section Profile

The fabrication of waveguides with femtosecond laser direct writing leads to a complex refractive index distribution. In order to obtain more insight on the waveguide cross-section profile, several waveguides were fabricated with parallel polarization (polarization parallel to the writing direction) while varying pulse energy, scan velocity and depth.

Figure 4.2 shows the cross-section of waveguides fabricated with pulse energies between 100 and 300 nJ, depths between 50 and 250 μm, and a velocity of 100 μm/s. From the pictures can be seen that the waveguide cross-section consists of an elongated inverted droplet shape. This droplet shape is caused by the size of the depth of focus and, possibly, due to self-focusing and/or spherical aberrations when the power is increased. It is also visible that the structure created is composed by two regions, top and bottom. The top region does not guide light and therefore is associated with a decrease of the refractive index, while on the bottom region light is guided and is therefore associated with an increase of the refractive index. This feature was already shown with refractive near field measurements [3].

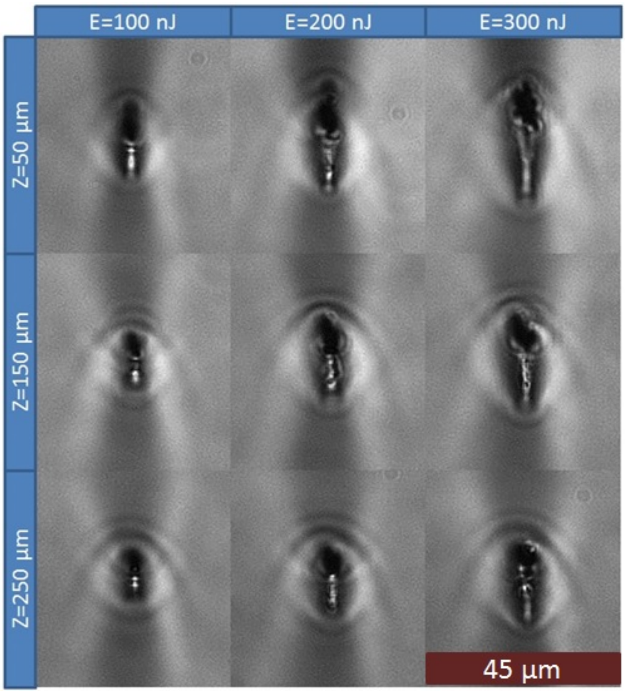

Figure 4.2: Cross-sectional images of waveguides fabricated with a pulse energy between 100 and 300 nJ, depth between 50 and 250 μm, and a scan velocity of 100 μm/s.

Figure 4.2 also shows that waveguide dimensions are dependent on writing parameters. In figure 4.3 (a) the waveguide height is plotted as a function of pulse energy, and, as can be seen, the waveguide height increases with pulse energy. This is likely due to more energy being deposited on the top because of self-focusing and spherical aberrations. On the other hand, in figure 4.3 (b) waveguide height is seen to decrease with depth. This feature is not so obvious and probably occurs due to temporal pulse broadening of the femtosecond laser beam, which decreases the peak power and thus the total energy absorbed by the sample.

4.3 Waveguide Depth Control

To be able to produce high complexity 3D integrated optical devices, and to be able to control the fabrication conditions, one needs to know how the writing depth is changing with the objective displacement.

To answer this, a reference has to be found. Logically, the best and easiest reference to find is the first surface that the beam encounters, the top surface of the substrate. When a bright spot is visible on the CCD the beam focus is on the substrate surface, since part of it is reflected and travels collimated back to the CCD. The main advantage of using this method is that any misalignment on the Z axis (vertical axis) is visible, due to the formation of interference rings around the spot caused by light rays that are not fully collimated.

After the reference has been established several waveguides were written at different

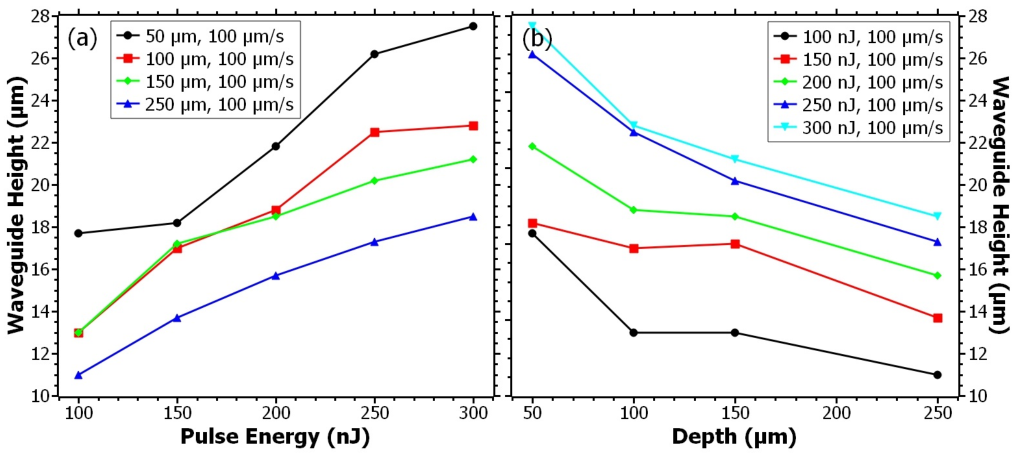

Figure 4.3: (a) Waveguide height in function of pulse energy for waveguides fabricated with a depth between 50 and 250 μm and a scan velocity of 100 μm/s. (b) Waveguide height in function of depth for waveguides fabricated with a pulse energy between 100 and 300 nJ and a scan velocity of 100 μm/s.

depths, by displacing the objective, with different pulse energies. To measure the waveguide depth the distance between the substrate surface and the boundary between high and low refractive index was obtained, since this characteristic determines, more or less, the center of the structures written. In figure 4.4 the waveguide depth is plotted as a function of calculated depth for different pulse energies. From the figure it is clear that the simple approach used to determine the waveguide depth (see section 2.3.1) is valid in this range of depths, since the slopes of the expected and experimental results match. However, the interception at the origin for the expected and experimental results do not match. This mismatch is around 10 μm (for waveguides written at 100 nJ) and is probably due to the alignment of the focus with the reference. This effect can take place due to a finite depth of focus and/or due to misalignment of the CCD in the axial axis, where the distance between the CCD and the lens that focus the image is not equal to its focal distance. By last, it is also visible that for higher pulse energies the parallel mismatch increases. This effect is attributed to self-focusing as will be seen next.

Since high peak powers are used, attention must be paid to self-focusing effects (see subsection 2.3.2). If self-focusing occurs the waveguides written are expected to appear closer to the surface. To test this possibility waveguides were written at different depths with a pulse energy between 100 and 300 nJ and were analyzed regarding the depth level of the bottom, middle (zone between high and low refractive index) and top part of the written structure. The results obtained are displayed in figure 4.5. From the figure it can be seen that self-focusing does indeed occur for all depths, and that the maximum increase in the top part of the structure is around 10 μm. One interesting aspect is that, even if the top part of the structure rises due to self-focusing, the bottom part stays at the same position. This aspect of self-focusing was already reported [22]. From figure 4.5 it is also visible that the depth of the region between high and low refractive index is a good

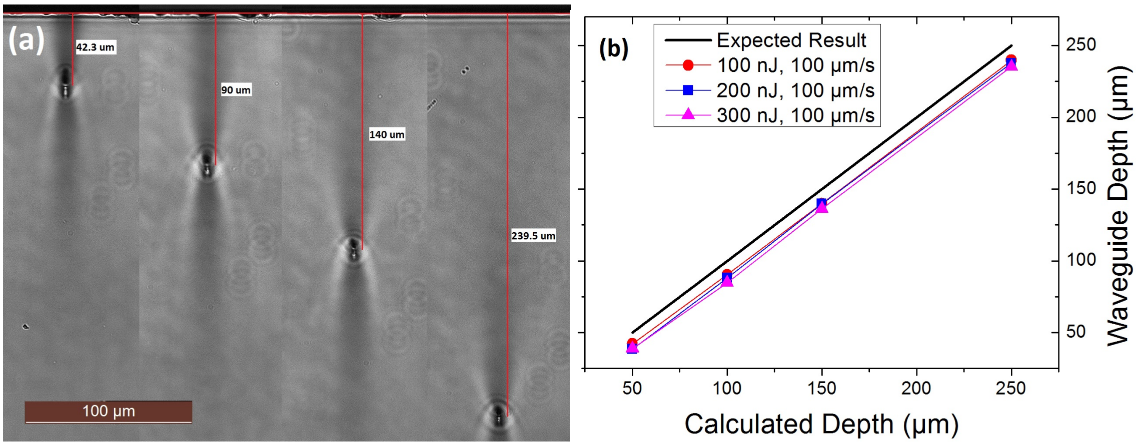

Figure 4.4: (a) Testing of waveguides with depth. (b) Waveguide depth as a function of calculated depth (from equation 2.7), for waveguides fabricated with a pulse energy between 100 and 300 nJ and a scan velocity of 100 μm/s, and the expected result.

indicator for the depth of the structures written, since this gives a rough estimate of the middle of the structure.

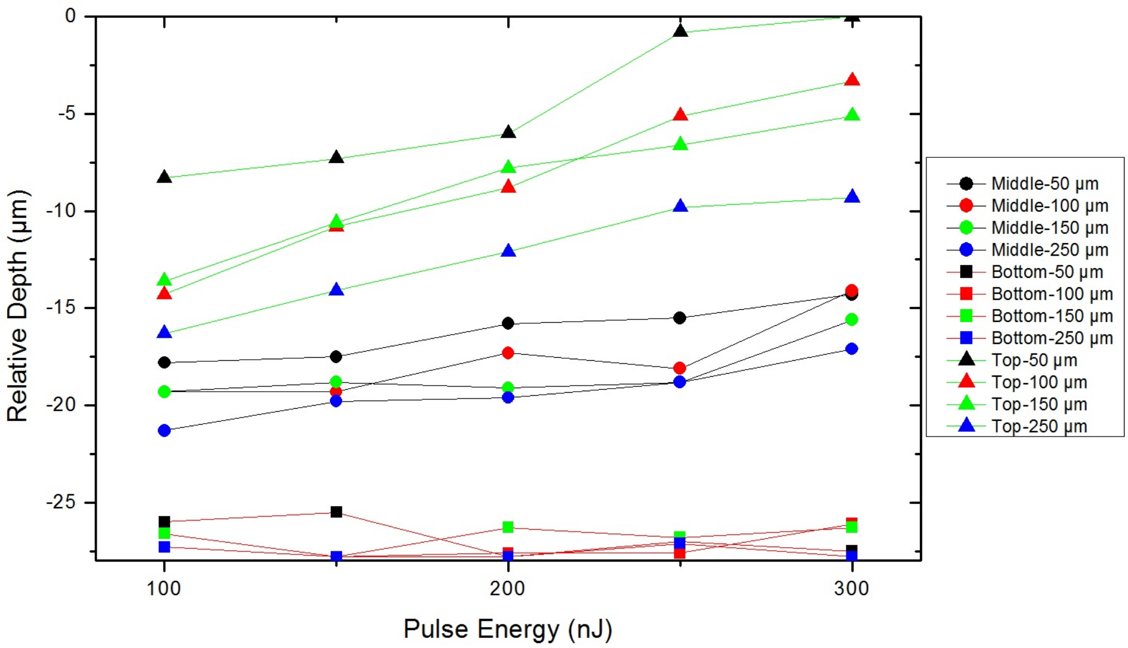

Figure 4.5: Relative depth as a function of pulse energy, for waveguides fabricated at a depth between 50 and 250 μm and a velocity of 100μm/s. The depth of the bottom of the waveguides is 52, 99, 149 and 246 μm.

4.4 Optimization of Writing Polarization

There are several fabrication parameters that influence the waveguide quality and the first parameter to be optimized was polarization. To optimize polarization several waveguides were fabricated while changing the pulse energy, substrate scan velocity and depth. Figure 4.6 (a) and (b) displays the waveguide insertion loss for parallel and perpendicular writing polarization, respectively, as a function of pulse energy and velocity for different depths. Both figures show that the minimum insertion loss was obtained at a depth of 50 μm, with an insertion loss of 1.32 dB and 2.49 dB being obtained for 2.5 cm long waveguides fabricated with parallel and perpendicular writing polarization, respectively. Since there is a large difference in insertion loss between both polarizations, parallel writing polarization was chosen for further investigations.

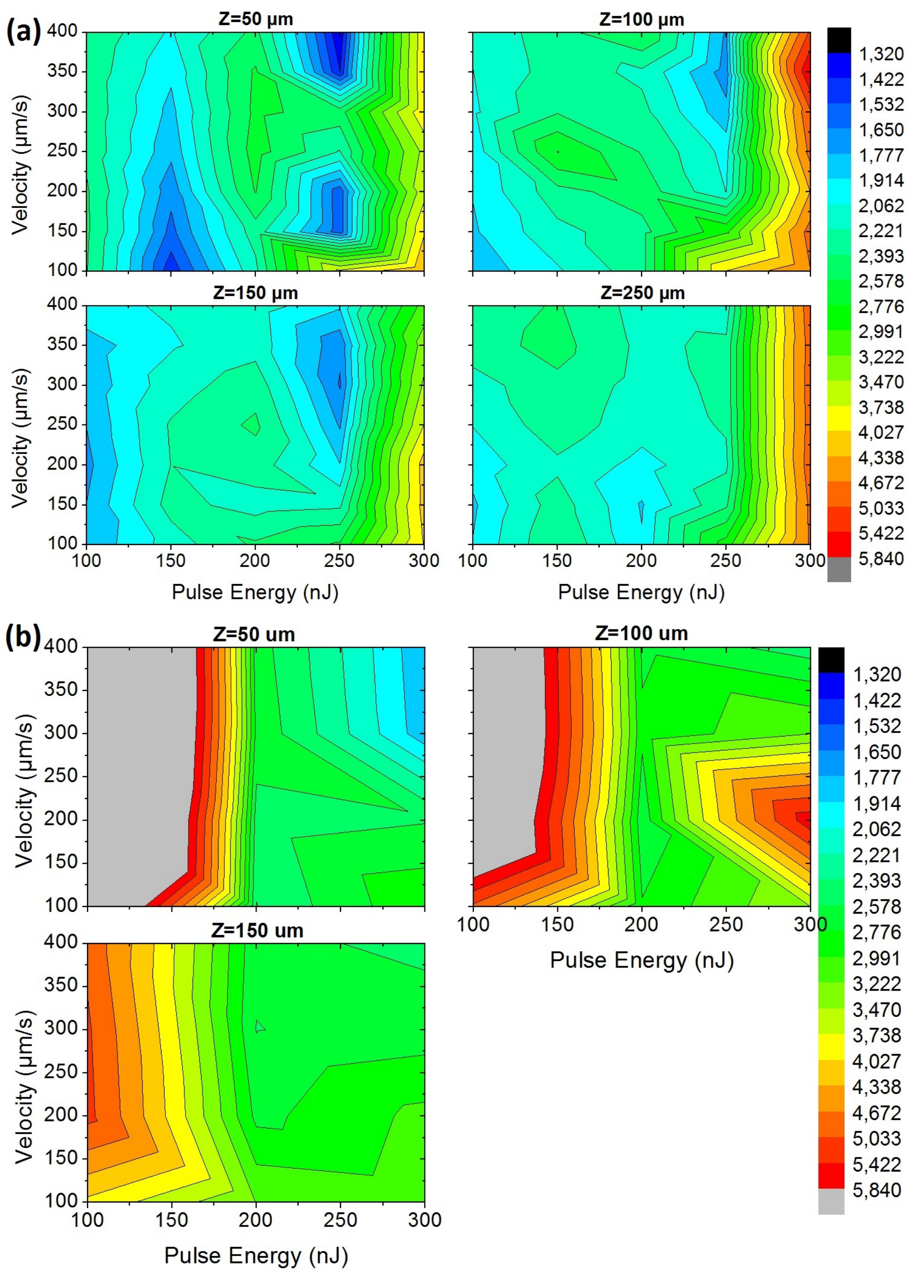

Figure 4.6: Insertion loss of waveguides fabricated with parallel (a) and perpendicular (b) polarization, as a function of pulse energy and scan velocity for different depths, before polishing.

4.5 Border Effects

In fabricating integrated optical devices care must be taken at the borders of the substrate. Since the beam being focused has a given dimension it is expected that at the borders a part of the beam enters the substrate from the side while the other part enters the substrate from the top, resulting in a perturbed waveguide at the extremities as shown in figure 4.7.

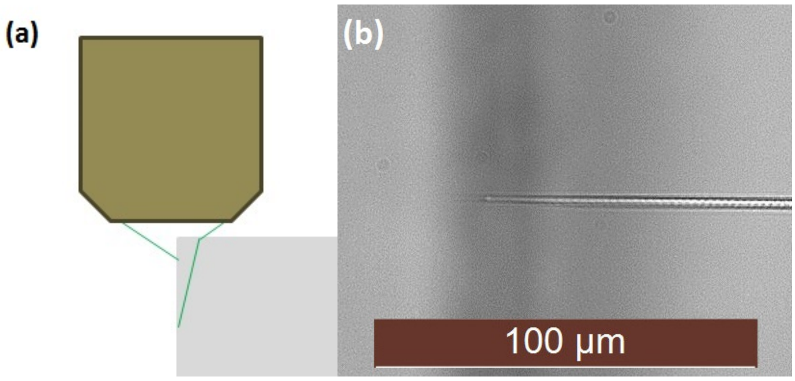

Figure 4.7: (a) Illustrative image of a microscope objective focusing a beam while at the edge of a substrate. (b) Top view of a waveguide fabricated from the border at a depth of 150 μm.

As represented in figure 4.7, depending on the position of the writing objective over the edge of the substrate, only part of the writing beam exposes the substrate at the correct height. This means that, depending on the objective location, there is the probability of not even reaching the nonlinear absorption threshold required to have an increase of the refractive index, meaning that the waveguide fabrication right to the edge of the substrate may not be possible. Taking this effects into account, if the energy per pulse is large enough it is expectable to see waveguides starting with a small modification and, while the beam progressively makes its way into the substrate, observing the modification grow until all the beam is totally focused inside the substrate through the top. This effect was observed and is shown in figure 4.7 (b). It should be noted that this effect is larger for higher writing depths, as expected.

Since the fabricated waveguides have a transition region at the borders the insertion loss is affected. To quantify this effect waveguides were fabricated on a previously polished substrate and insertion losses measured, followed by another polishing, to remove the transition region, and the insertion losses were measured again on the same waveguides. This procedure was done for different pulse energies, scan velocities and depths, and, from the subtraction of the insertion loss before and after polishing, the edge loss for both edges obtained. The results obtained are plotted in figure 4.8. From here we can observe that for different depths the edge loss behavior is different. At low depths the edge loss is bigger for higher pulse energies, and smaller for lower pulse energies. As depth increases the maximum edge loss seems to shift to lower pulse energies, where, at a depth of 250 μm, it is visible that with a pulse energy of 300 nJ the insertion losses after the polishing are higher than before.

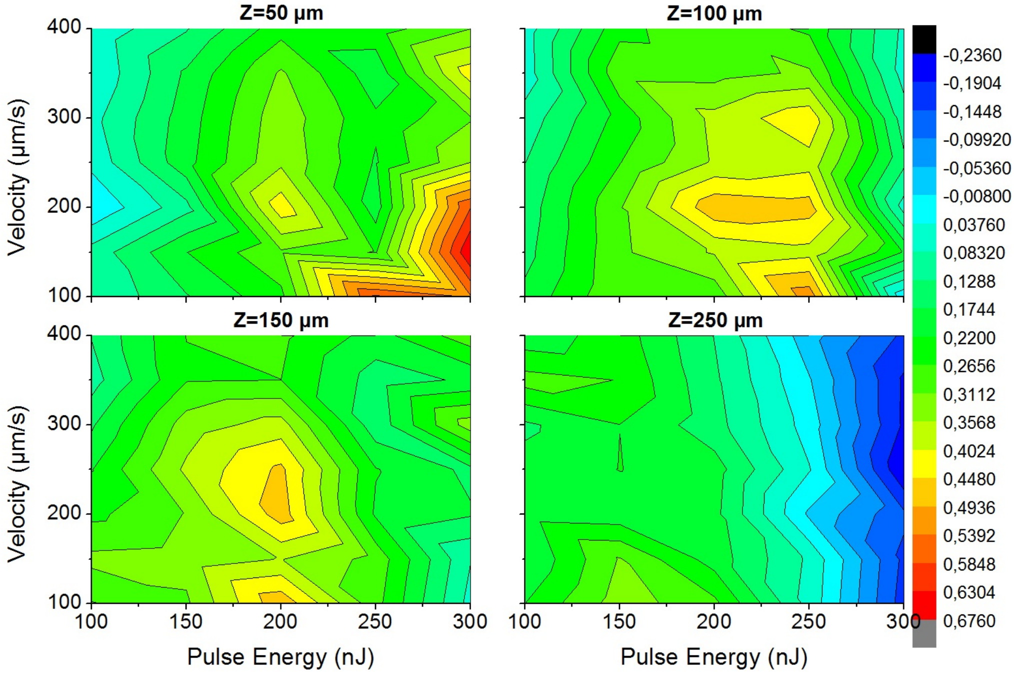

Figure 4.8: Edge loss as a function of pulse energy and scan velocity, for different depths, of the fabricated waveguides due to the change in writing beam pulse energy at the border of the substrate.

To have further insight in the edge loss behavior individual analysis on pulse energy, scan velocity and depth were made. Figure 4.9 (a) displays edge loss as a function of pulse energy for different scan velocities and depths, where the depth dependent behavior is evident. For a depth of 50 μm the edge loss is seen to increase with pulse energy, but, as depth increases, the edge loss maximum shifts to lower pulse energies, where, at a depth of 250 μm, a greater insertion loss is found after polishing for a pulse energy of 300 nJ. Figure 4.9 (b) shows the edge loss as a function of scan velocity for different scan velocities and depths, where a small dependence with scan velocity can be seen. Although small, edge loss clearly decreases monotonically with scan velocity. Relatively to the edge loss in function of depth, the analysis was made but no apparent behavior was observable.

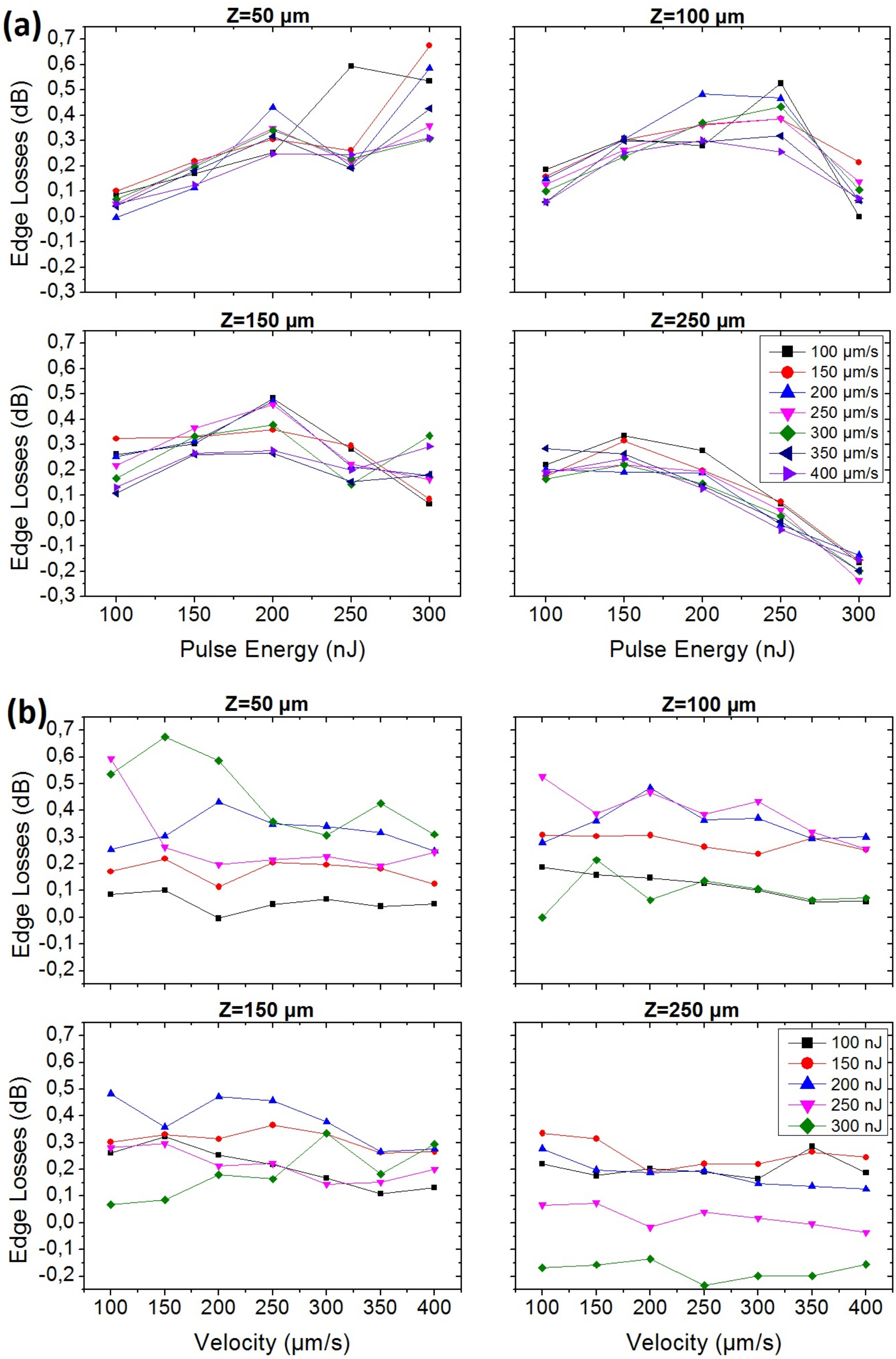

Figure 4.9: (a) Edge loss as a function of pulse energy for different scan velocities and depths. (b) Edge loss as a function of scan velocity for different pulse energies and depths.

4.6 Optimization of Pulse Energy, Velocity and Depth

As already seen in section 4.4, fabrication parameters have a big impact in a waveguide guiding efficiency. In this study some parameters were optimized by fabricating waveguides while changing the pulse energy, substrate scan velocity and depth, in order to obtain an insertion loss as low as possible at 1550 nm.

Figure 4.10 displays the insertion loss as a function of pulse energy and velocity for different depths, after polishing the substrate to eliminate any border effects. From the figure it is possible to affirm that the minimum insertion loss still occurs at a depth of 50 μm, for a pulse energy of 150 and 250 nJ, while, in general, the maximum insertion loss occurs for a pulse energy of 300 nJ for all depths tested. As depth increases the minimum insertion loss seems to shift to a lower pulse energy. The most important result to retrieve from here is that the best waveguide measured was fabricated with a pulse energy of 250 nJ, a scan velocity of 400 μm/s and a depth of 50 μm. This waveguide yielded an insertion loss of 1.08 dB for a 2.5 cm long waveguide.

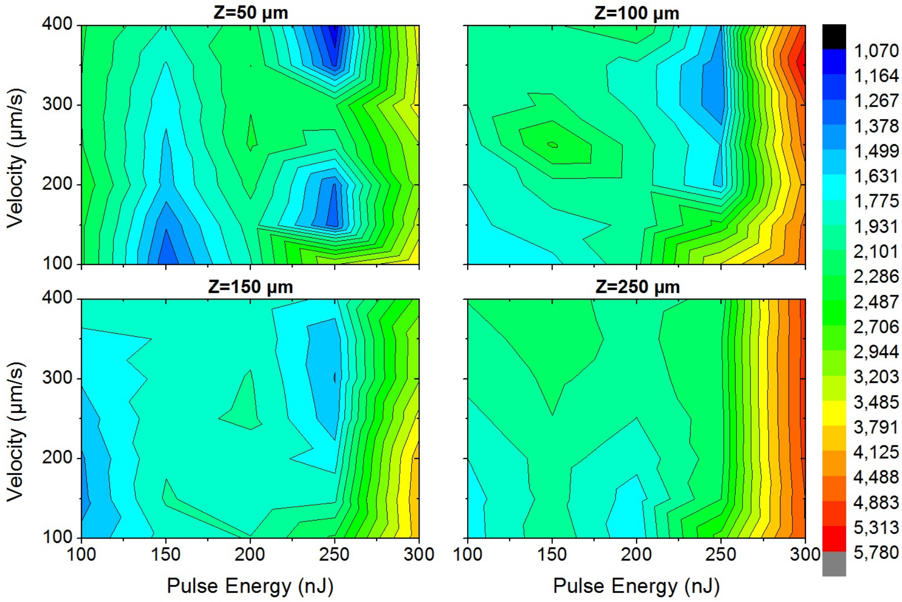

Figure 4.10: Insertion loss, at 1550 nm, of the fabricated waveguides as a function of pulse energy and scan velocity for different depths and a parallel writing beam polarization.

For further insight on the insertion loss behavior individual analysis with pulse energy, scan velocity and depth were made. Figure 4.11 (a) displays insertion loss as a function of pulse energy for different scan velocities and depths, where, at a depth of 50 μm, two insertion loss minima are observed at 150 and 250 nJ. As depth increases the first and second minima translate to 100 and 200 nJ respectively, while the insertion loss of these minima increases. It is also visible that the insertion loss increases dramatically for a pulse energy of 300 nJ, independently of fabrication depth, and that the insertion loss behavior gets flatter with increasing depth.

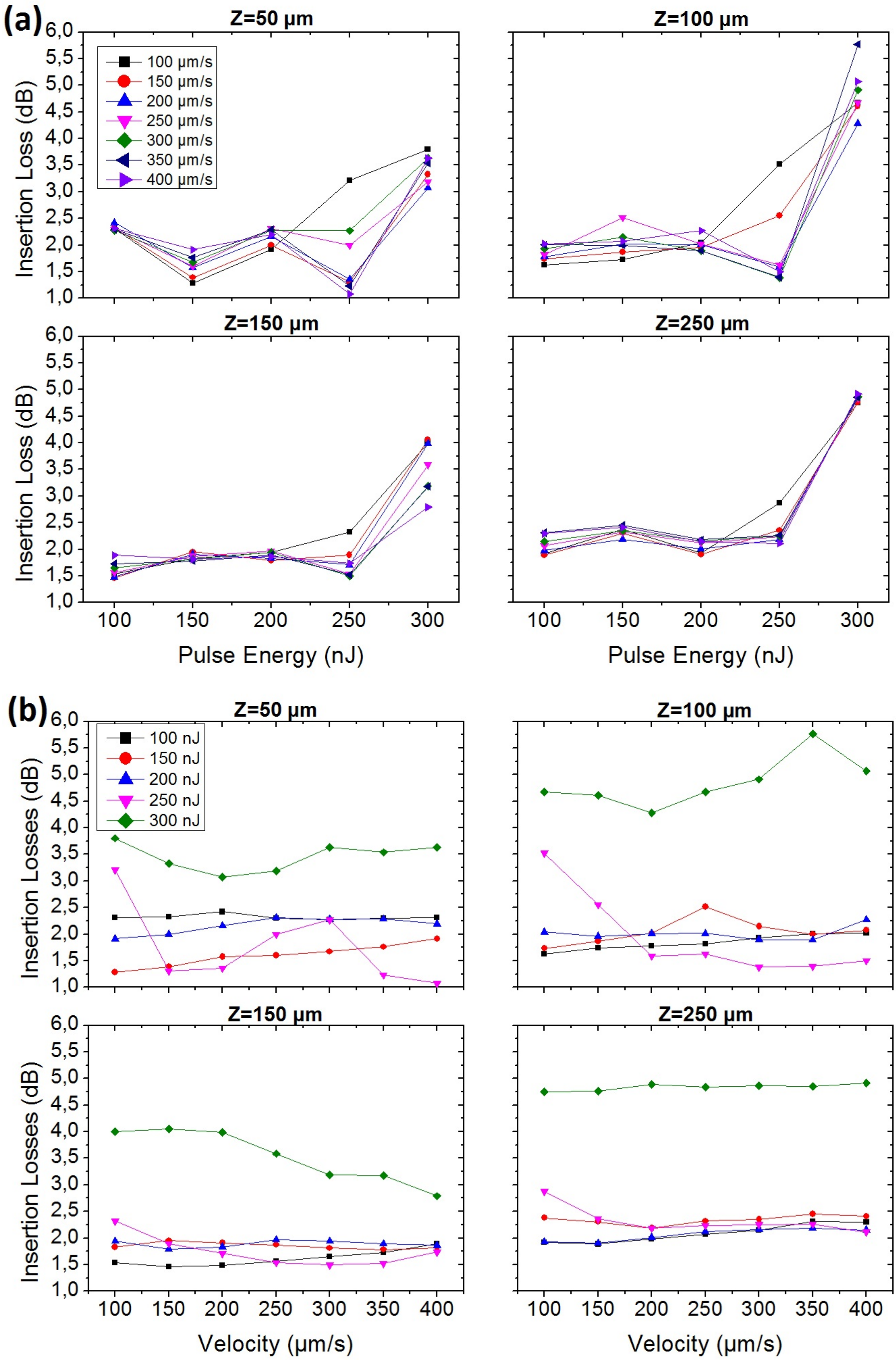

Figure 4.11: (a) Insertion loss as a function of pulse energy for different scan velocities and depths. (b) Insertion loss as a function of scan velocity for different pulse energies and depths.

Figure 4.11 (b) displays insertion loss as a function of velocity for different pulse energies and depths, where a low dependency on scan velocity can be seen with a few exceptions. In this exceptions are the waveguides fabricated with a depth of 50 μm and a pulse energy of 250 nJ, where two low insertion loss windows are available. In this figure a flattening behavior is also seen for higher depths, showing that for this case the insertion loss is invariant with velocity (for the ranges tested).

An analysis of insertion loss as a function of depth was also made but no conclusive results were obtained.

In order to better understand the different contributions leading to the insertion loss the coupling loss has to be determined. To be able to obtain the coupling loss of the fabricated waveguides the modal field distribution was measured. Figure 4.12 (a) shows the mode field diameter as a function of pulse energy, where the similar behavior of the X and Y directions is obvious (despite the difference in scales). The horizontal and vertical mode diameter difference is also notorious, with this being derived by the elongated cross-section profile of the waveguide (as already seen in section 4.2). One characteristic of this curves is that the minimum mode diameter is not observed at the lowest pulse energy. This probably happens because at low pulse energies both waveguide dimensions and refractive index contrast are small, which contributes to a large modal diameter since the confinement of the mode is small. When the pulse energy is increased the waveguide dimensions also increase but the confinement plays a major role and the modal diameter ends up decreasing. At higher energies the refractive index modification saturates and the waveguide dimensions start to dominate the mode diameter. Another characteristic present is the modal diameter minimum shifting to lower pulse energies with increasing depth. This might occur due to the decrease of the waveguide dimensions or refractive index modification with depth, since less energy is being absorbed because of temporal pulse broadening.

Figure 4.12 (b) displays the mode field diameter as a function of scan velocity. In previous analysis velocity did not seem to be a determinant factor, and a similar behavior was also noticed here.

Again, an analysis with depth was also made but no conclusive results were obtained.

Figure 4.13 shows the coupling loss, obtained by equation 3.5, as a function of pulse energy and scan velocity for different depths for all waveguides fabricated. From figure 4.13 (a) it can be seen that the largest coupling losses are found at high pulse energies. It also shows that a local coupling loss minimum is obtained at 250 nJ, while increasing depth, and that this minimum shifts to lower pulse energies. Finally, it is also possible to observe that the coupling losses are minimum for 100 nJ, independently of the fabrication depth.

As for the dependency with scan velocity, figure 4.13 (b) displays coupling loss as a function of scan velocity. As expected from previous results, a low dependency of coupling loss with scan velocity is observable. Despite being small, coupling loss is seen to decrease with scan velocity.

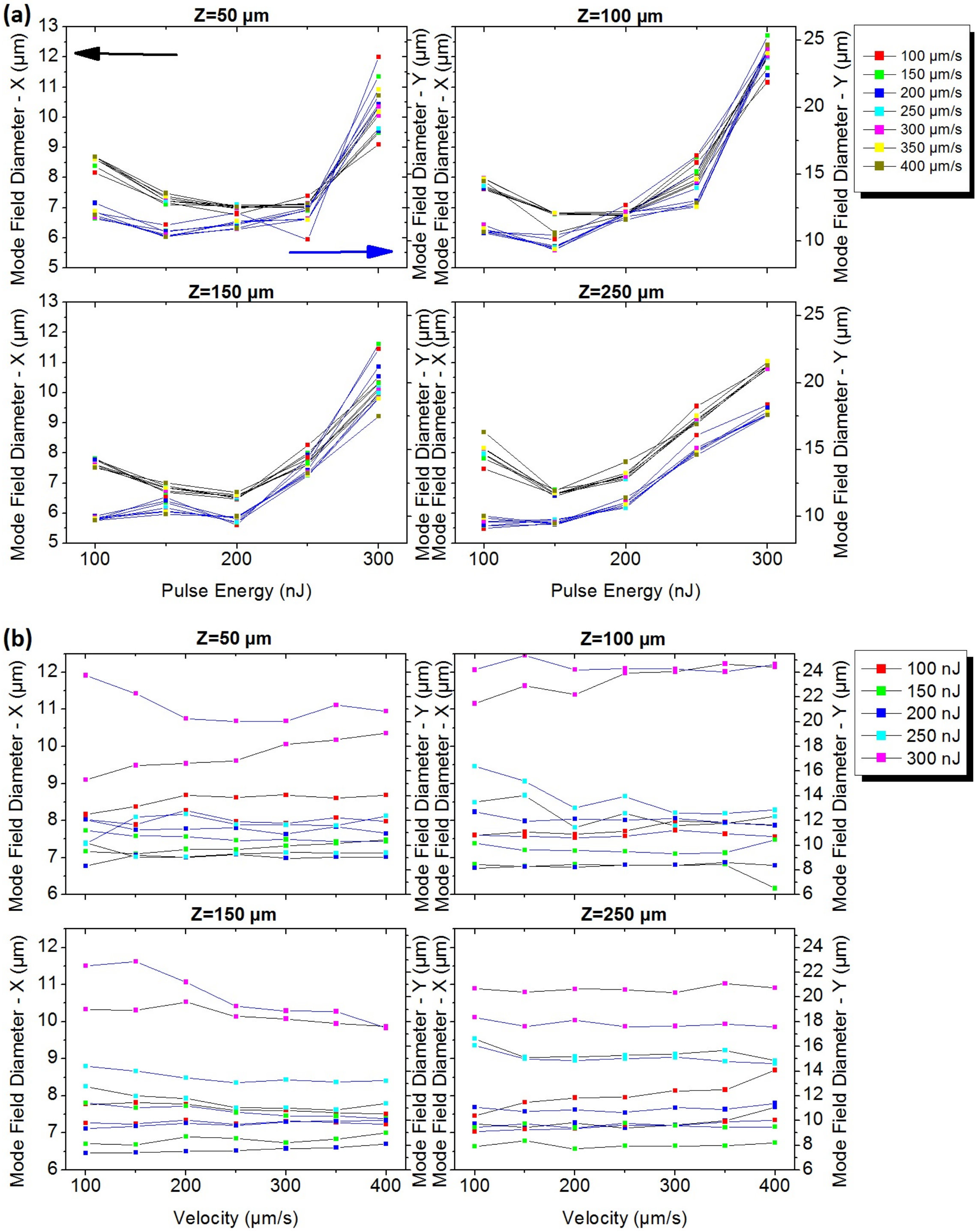

Figure 4.12: Mode field diameter of the X (horizontal) and Y (vertical) directions as a function of pulse energy (a) and scan velocity (b).

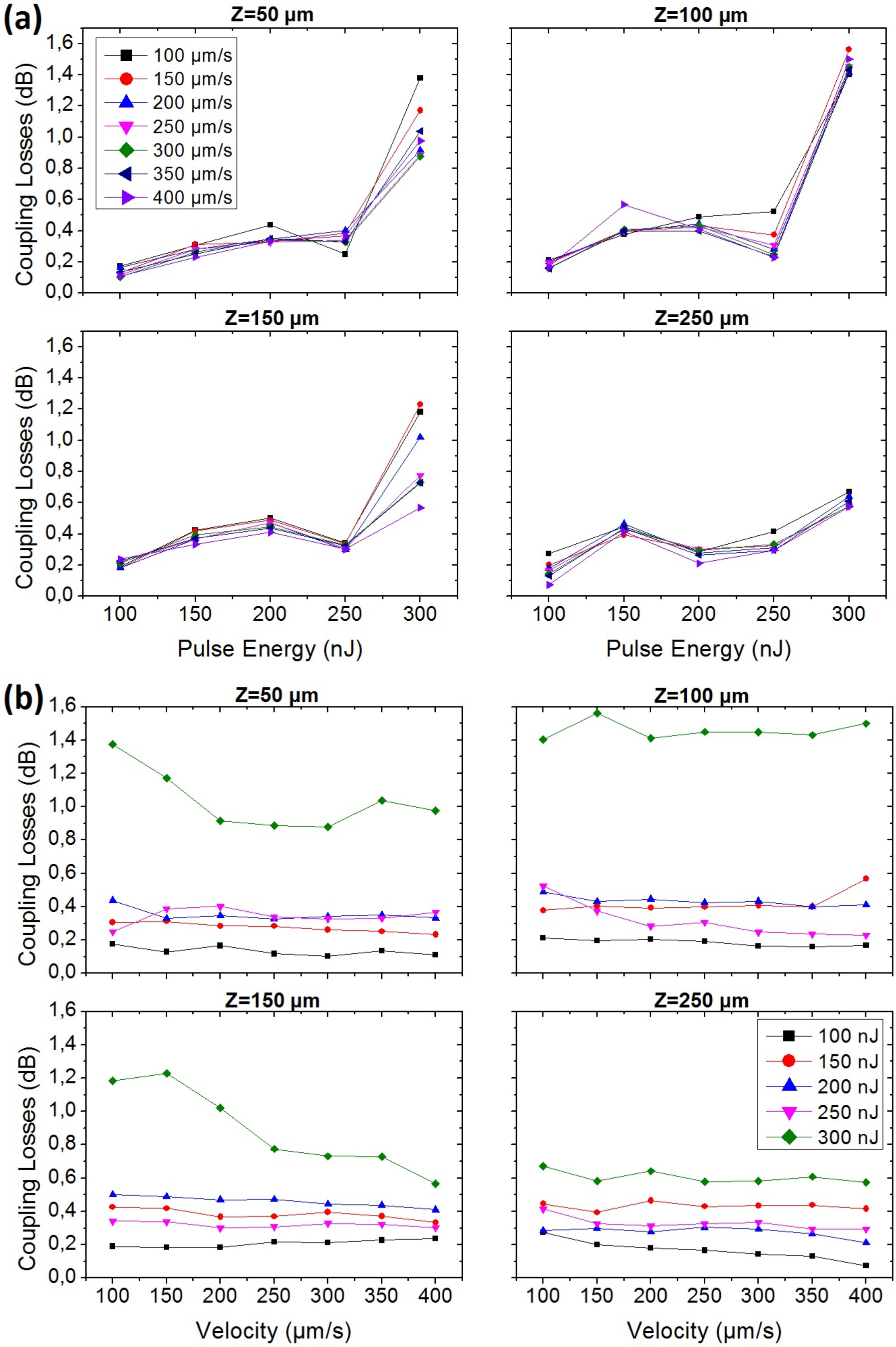

Figure 4.13: Coupling loss between the fabricated waveguides and a SMF 28, at 1550 nm, as a function of pulse energy (a) and scan velocity (b).

Relatively to the dependence with depth, figure 4.14 shows that for a pulse energy between 100 and 250 nJ the coupling loss variation is small, while at 300 nJ the coupling loss tend to decrease with depth.

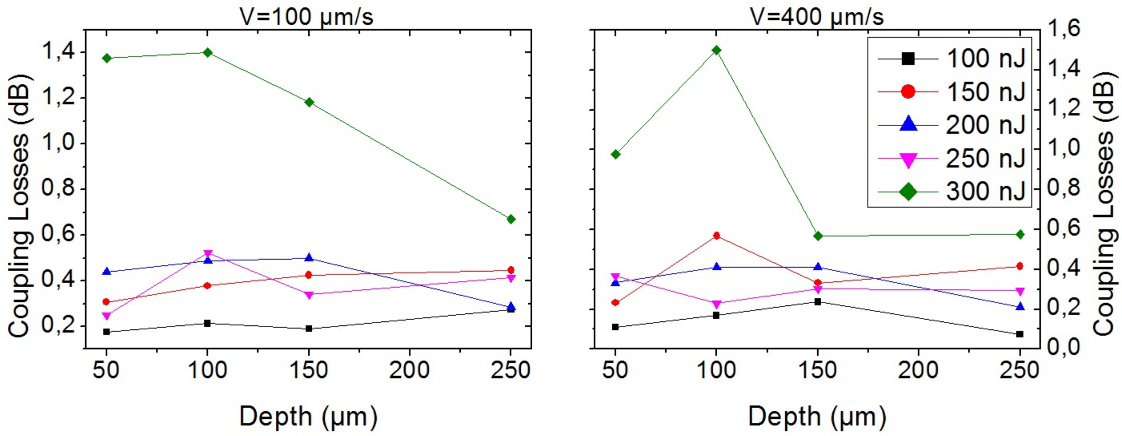

Figure 4.14: Coupling loss between the fabricated waveguides and a SMF 28, at 1550 nm, as a function of depth.

The major objective of this analysis is to find the propagation losses of the fabricated waveguides. This is an interesting measurement because it is the quantity that will dominate the losses for longer waveguides. Figure 4.15 shows the propagation losses of the fabricated waveguides in function of pulse energy and scan velocity at different depths. From the figure we are able to see that the behavior is different for each depth. At a depth of 50 μm there are three main areas where low propagation loss is observed (one at 150 and two at 250 nJ). Still at a depth of 50 μm, it also observed that at 100 nJ the propagation loss is relatively high. As depth increases to 250 μm, these low propagation loss areas fade away and the propagation loss gets more uniform. At 250 μm it is also observed that, for a pulse energy of 300 nJ, the propagation losses increase dramatically.

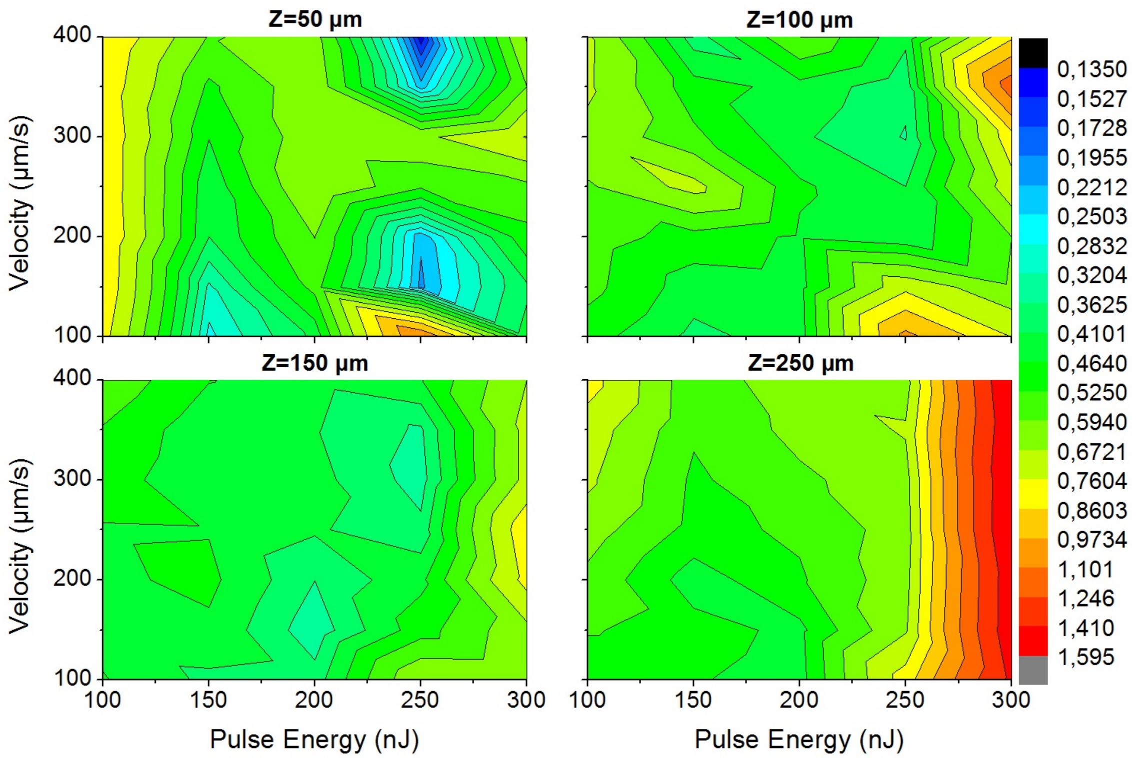

Figure 4.15: Propagation loss, at 1550 nm, of the fabricated waveguides as a function of pulse energy and scan velocity for different depths.

To better visualize these effects, graphics of propagation loss were built and displayed in figure 4.16 for each individual parameter. From figure 4.16 (a) it becomes easy to understand what was stated before. At a depth of 50 μm there are two local propagation loss minima for a pulse energy of 150 and 250 nJ. As depth increases the minimum propagation loss is transferred to 250 nJ and then shifts to lower pulse energies. It is also interesting to see that, at a depth of 50 μm , the maximum propagation loss is found at 100 nJ, and that at a depth of 250 μm the maximum propagation loss is found at 300 nJ. One last thing to retain is that the propagation loss behavior is relatively constant in certain zones, which might indicate that the pulse energies being used are placed in the center of what could be a parabola like curve, where the non central part of the parabola occurs due to lack of confinement at low pulse energies and increased scattering at higher pulse energies.

Figure 4.16 (b) shows that for most of the pulse energies the propagation loss has very little dependence with scan velocity. There are however exceptions, and one comes at a depth of 50 μm with a pulse energy of 250 nJ, where two propagation loss minima are observed. These exception zones should be highlighted because these are the zones where the lowest propagation losses were found, being registered, at 400 μm/s, a propagation loss of 0.14 dB/cm.

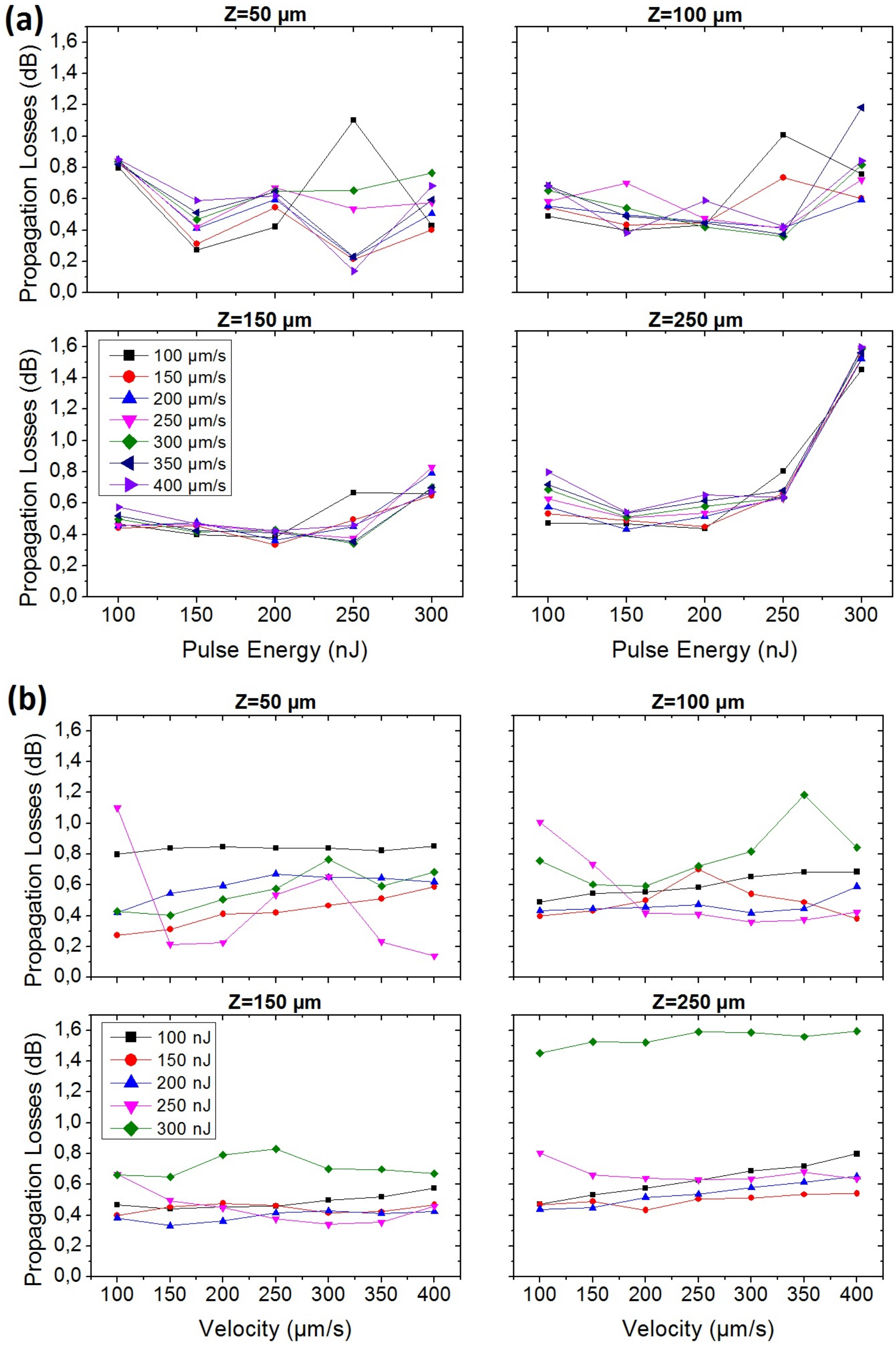

Figure 4.16: Propagation loss, at 1550 nm, of the fabricated waveguides as a function of pulse energy (a) and scan velocity (b).

4.7 S-Shaped Optical Waveguide Bends

In order to fabricate more complex devices bent waveguides are required. These bent waveguides, also called S-bends, can be manufactured with several shapes, from cosine to sine and arc shapes. In this thesis arc shaped S-bends were used since BPM simulations showed that this design gives better performance for most of the design parameters [56].

Bend loss was studied for the best waveguide fabrication parameters by measuring the insertion loss of a waveguide displaced by a S-bend, as shown in figure 4.17 (a), and subtracting the insertion loss measured for a reference waveguide. The input to output lateral shift range was changed from 125 μm to 500 μm, for bend radii varying between 3 and 80 mm, which translates into a longitudinal transition length varying from 1.22 to 12.64 mm. The measured bend loss, which consists of transition loss and loss due to the curvature itself, is plotted in figure 4.17 (b) as a function of bend radius for 1550 nm. This figure shows that bend loss decreases dramatically with bend radius, with bend loss being negligible for radii larger than 50 mm. Regarding the several separations tested, it appears that for radii larger than 30 mm the bend loss becomes approximately equal for all the separations tested.

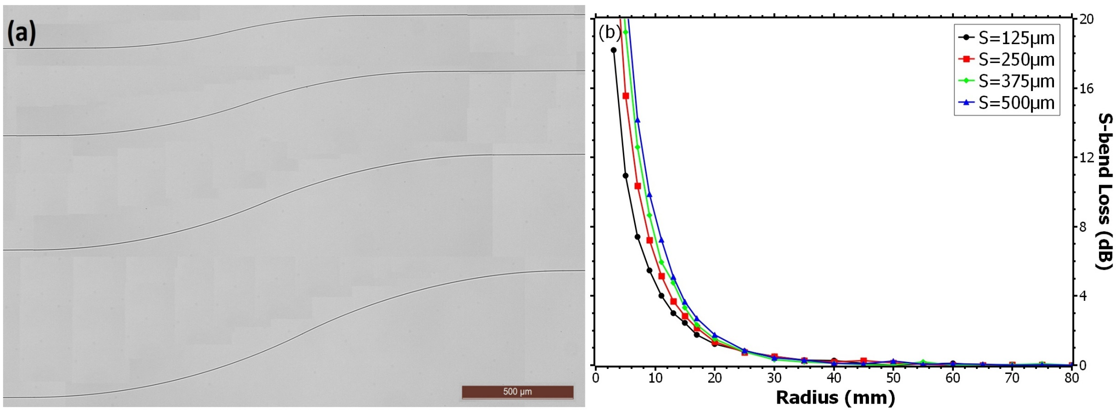

Figure 4.17: (a) Microscope images of s-bends (R=3 mm) with input and output waveguide separations of 125, 250, 375 and 500 μm from top to bottom respectively. (b) Bend loss in function of bend radius for different waveguide separations.

In an effort to reduce the S-bend loss a study was conducted on the bend loss as a function of the offset at the inflection point, as seen in figure 4.18 (a). In figure 4.18 (b) the bend loss change, in relation to zero offset, is plotted as a function of the bends offset, for multiple bend radii. This figure shows that the optimum offset, that offers minimum bend loss, shifts to lower values as bend radii increases, since the propagating mode is not as shifted from the core for large bend radius and small bend angle as for a small bend radius and large bend angle. It also shows that the improvement in bend loss decreases as bend radius increases, since the overall bend loss decreases.

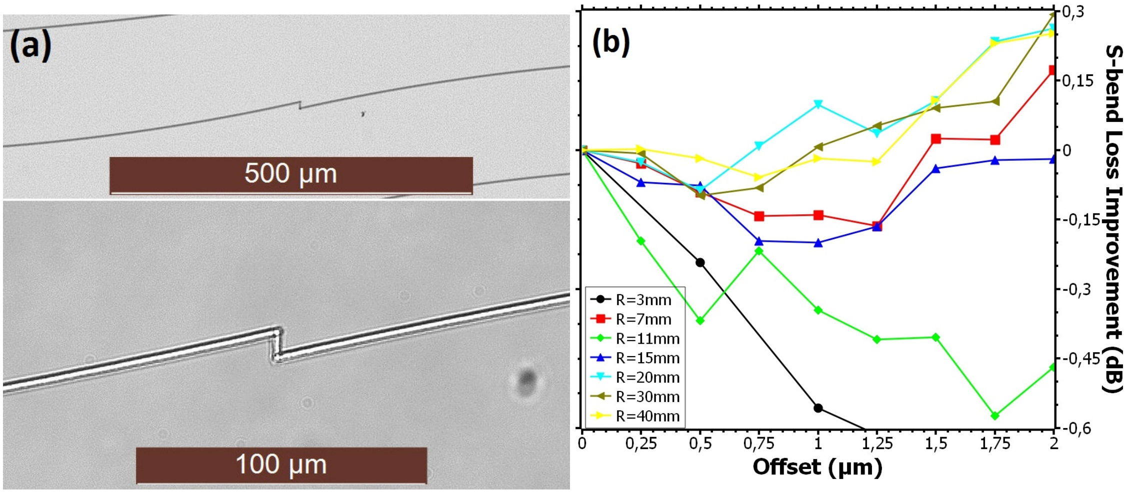

Figure 4.18: (a) Microscope images of the same S-bend with an offset of 9 μm. (b) Bend loss change as a function of arc offset for different bend radii.

In short, from this results and from the need of negligible bend loss, to minimize the total insertion loss, a high bend radii is required. For these conditions the offset solution becomes irrelevant and was dropped. It must be noted that further bend loss improvement can be achieved using another offset at the end of the second arc, but this improvement will be even smaller than the previous offset and introduces non reciprocity on the device, since the light that propagates in the opposite direction will encounter a shifted arc. With this study a bend radius of 80 mm was chosen for all the devices produced due to the increased stability, since there is only an increase of 26 % in the device length (to 6.32 mm at a separation of 125 μm) when compared with a bend radius of 50 mm.

4.8 Conclusions

In this chapter a 500 kHz femtosecond fiber laser was used to study the fabrication of low loss waveguides in fused silica. For this, 140 waveguides were fabricated with parallel polarization, a 0.55 numerical aperture aspheric lens, and different pulse energies, scan velocities and depths. The fabricated waveguides were then characterized to find the best writing parameters.

The waveguide cross-section profile was studied, where the existence of a zone of positive refractive index change, where light is guided, and a zone of negative refractive index change were confirmed. From this analysis it was also concluded that the height of the waveguide increases with pulse energy and decreases with depth.

Waveguide fabrication depth was also controlled, where it was found that a simple approach based in the refraction on the air-substrate interface is sufficient. It was also verified that there is a depth mismatch of about 10 μm, since having a larger depth of focus complicates the task of centering on the interface. Self-focusing was discovered, where the waveguide's bottom remains at the same depth but the top rises with increasing power.

The insertion loss was studied for a parallel and perpendicular writing polarization, where both insertion loss minima were found at a depth of 50 μm. However, it was discovered that waveguides fabricated with perpendicular polarization have much higher insertion losses.

The extremities of the waveguides were analyzed and a border effect discovered. It was deduced that only the part of the beam that refracts on the top of the substrate has enough power to modify the material. Since the writing beam power is not constant when passing on the edge, waveguides written on the edges have a transitional length, dependent on the depth, that possess different properties from normal waveguides.

Relatively to the parameter optimization, it was found that, for the variable range used, the lowest coupling loss is obtained at 100 nJ. As for propagation losses, the two best low loss zones were found at 150 and 250 nJ, at a depth of 50 μm. The waveguides fabricated showed a small increase of the propagation loss with increasing scan velocity, with a few exceptions. Surprisingly, one of the exceptions is where two low propagation loss zones appear and where the minimum propagation loss is registered.

With this, the best waveguide in terms of insertion loss and propagation loss was found. The waveguide was fabricated with a pulse energy of 250 nJ, a scan velocity of 400 μm/s and a depth of 50 μm, yielding an insertion loss of 1.08 dB with a coupling loss of 0.37 dB and a propagation loss of 0.14 dB/cm. The best waveguide in terms of coupling loss was fabricated with a pulse energy of 100 nJ, a scan velocity of 400 μm/s and a depth of 250 μm, having been found a coupling loss of just 0.07 dB.

To finalize, bend loss was analyzed as a function of bend radius for the best waveguide fabrication parameters. It was found that bend loss quickly decreases with curvature radius, with bend loss being negligible above 50 mm. For different input/output waveguide separations the difference between bend loss was also found to be negligible above a 30 mm curvature radius.

Chapter 5

Fabrication of Passive Photonic Devices

Chapter 4 introduced the fabrication of low loss optical waveguides in fused silica and the study of S-bends to allow different fabrication geometries. In a sense, the previous chapter served as a base for the fabrication of more complex integrated optical devices. In this chapter previous results are used to fabricate passive photonic devices that can be seen as building blocks. In the end of the chapter an example of a fabricated add-drop multiplexer device is shown demonstrating the possibilities and capabilities of femtosecond laser direct writing.

In section 5.1 uniform Bragg grating waveguides fabricated with different duty cycles and writing polarizations are characterized. Propagation and coupling loss are measured, as well as the grating strength, Bragg wavelength and birefringence. In section 5.2, 5.3 and 5.4 three different power splitters are investigated. In section 5.2 directional couplers with separation distances between 5 and 15 μm are analyzed at 1550 nm. Measurements between 1300 and 1600 nm were also made to show the wavelength-division (de)multiplexing capabilities, and the possibility to create polarization splitters due to waveguide birefringence. In section 5.3 two designs are tested to obtain symmetrical Y-junction power splitters. Measurements from 1300 to 1600 nm show very good results for the arm separation design with the possibility to fabricate low-loss broadband Y-junction power splitters. In section 5.4 three multimode interference device designs were fabricated and tested, and the results compared to the results of simulation. The best device design is found by the modal distribution and microscope images of the devices. In section 5.5 an optical add-drop multiplexer is shown. The device is analyzed in terms of spectral response for the through and drop port, and compared with the specifications required to work in 100 GHz networks.

5.1 Bragg Grating Waveguides

Since the invention of the fiber Bragg gratings (FBGs), these devices have been showing their potential in telecommunications and sensing, due to their spectral characteristics. FBGs are fabricated upon an existing waveguide, but the Bragg grating waveguides (BGWs) shown in this section are devices fabricated in one process that function as both waveguides and Bragg gratings. BGWs fabricated with femtosecond laser direct writing were first used to show the high spatial resolution inherent to this fabrication technique. Nowadays they are being implemented in lab-on-a-chip devices as sensing devices, and, with current investigation, steps towards telecommunications are being made.

In this section the fabrication of uniform BGWs is demonstrated and a detailed study of the effect of some fabrication parameters has been performed.

5.1.1 Background

A Bragg grating is a periodic perturbation of the refractive index, or aperiodic depending on the spectral characteristics needed, with periods on the order of hundreds of nanometers. Such structures have millimeter to centimeter long sizes and lead to light reflection in a narrow range of wavelengths around the Bragg wavelength which is defined by:

$$\lambda_B = 2n_{eff}\mathit{\Lambda}, \tag{5.1}$$

where n_{eff} is the Bragg grating effective refractive index and $\mathit{\Lambda}$ the grating period [57]. The wavelength spacing between the first minima in the reflection spectra can also be deduced and is, in the strong grating limit, given by:

$$\mathit{\Delta}\lambda = \left[\frac{2\delta n_0 \eta}{\pi}\right]\lambda_B, \tag{5.2}$$

where δn_0 is the refractive index perturbation and η the fraction of power in the guiding region.

Essentially, the Bragg condition means that the multiple Fresnel reflections along the grating are in phase for a very specific wavelength (for a given periodicity), so that they can interfere constructively.

If we now consider a birefringent Bragg grating we obtain two different effective refractive indexes for the two orthogonal polarization modes. This means that a shift in the Bragg wavelength is present between both modes, and as such, the birefringence can be measured by:

$$B = \Delta n_{eff} = \frac{\Delta\lambda_B}{2\mathit{\Lambda}}. \tag{5.3}$$

Besides the reflection around the Bragg wavelength, side lobes are also present in the reflection spectrum. These are specially strong when the amplitude of the refractive index modulation is constant over the grating length (uniform Bragg grating). To minimize this effect, apodization can be used by modulating the coupling coefficient with a Gaussian function for instance. However, to have a pure apodization, the coupling coefficient should be varied while maintaining a constant mean effective refractive index, meaning a constant Bragg wavelength.

The fabrication of these Bragg structures have already been demonstrated using femtosecond laser direct writing. Uniform [8], chirped [58], phase-shifted [59] and apodized [60] BGWs have all been reported. BGWs have several applications in telecommunications and sensing. One application that has already been demonstrated is the lab-on-a-chip device, that combines sensing elements, such as BGWs, with microfluidics to sense refractive index [61].

5.1.2 Fabrication

The femtosecond laser system used for the fabrication of the BGWs was described in section 3.1. The second harmonic beam at λ = 515 nm with approximately 250 fs pulse duration was focused inside the fused silica substrate, 50 μm below the surface, with a 0.55 NA aspheric lens. To fabricate the BGWs the same parameters used in the fabrication of low loss optical waveguides were used (E_p=250 nJ, V=400 μm/s). In this particular study parallel and perpendicular writing beam polarizations were tested.

In order to fabricate segmented waveguides an acousto-optic modulator (AOM), present inside the laser system, was controlled as a fast on/off switch to enable the modulation of the femtosecond laser beam. To control the AOM modulation a Stanford Research Systems DS345 function generator was used to generate an arbitrary wave form. For the fabrication of the uniform BGWs presented in this section, the AOM was controlled by a square wave with a given frequency (see subsection 5.1.3) while varying the square wave duty cycle. This AOM modulation resulted in periodically spaced guiding segments with a periodicity given by:

$$\Lambda = \frac{v}{f}, \tag{5.4}$$

where v is the stages translation speed, and f the AOM modulation frequency. The uniform BGWs were fabricated with a length of 25 mm.

5.1.3 Chromatic Dispersion of Femtosecond Laser Fabricated Waveguides

As previously seen in equation 5.1, the wavelength at which a resonance is observed is dependent on the BGW periodicity; since n_{eff} is not known, several BGWs were fabricated while varying the AOM modulation frequency, with a duty cycle of 40 %. The results obtained are displayed in figure 5.1.

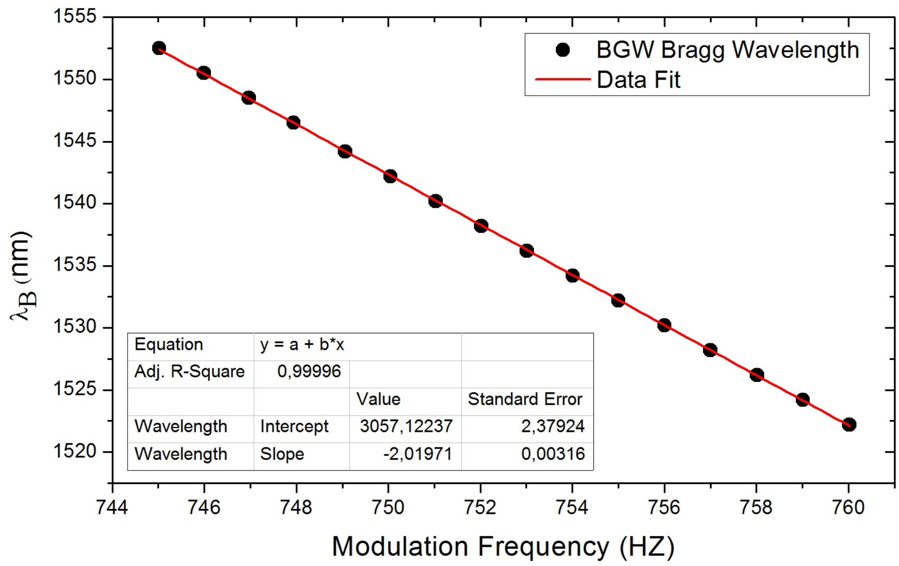

Figure 5.1: Bragg wavelength in function of AOM modulation frequency for parallel writing polarization.

For the range of AOM modulation frequencies tested it is possible to say that the Bragg wavelength behavior is linear with periodicity. Also, using an interpolation, it is visible that a modulation frequency around 746.13 Hz is required for λ_B=1550 nm. Since the translation velocity of the substrate relative to the beam focus is 400 μm/s, using equation 5.4 we get that the BGWs period, Λ, is approximately $536.1\ nm$. By using equation 5.1, and taking into account the previous results (Λ=536.1 nm and λ_B=1550 nm), an effective index, n_{eff}, of approximately 1.4456 is obtained.

Since the effective index gives an approximation of the waveguide refractive index, using the previous data from the BGWs fabricated and equation 5.1, an estimate on the waveguide's chromatic dispersion can be deduced. Figure 5.2 displays the results of the effective index measured for the BGWs fabricated with different AOM frequencies, as well as the refractive index of fused silica according to Sellmeir's equation. From the figure the parallel behavior of both curves is visible, showing that the chromatic dispersion of the waveguides fabricated is similar to the dispersion of pristine substrate silica.

5.1.4 Experimental Results

In order to find the best fabrication parameters for BGWs several devices were fabricated varying the writing duty cycle, from 10 to 90 %, and the writing polarization, parallel or perpendicular. Depending on the application different characteristics are required, and as such this subsection works as a catalog where the limitations are also explored.

The fabricated segmented waveguides yielded spectral responses as in figure 5.3. In this specific case these BGWs were written with a duty cycle of 40 % and parallel (a)

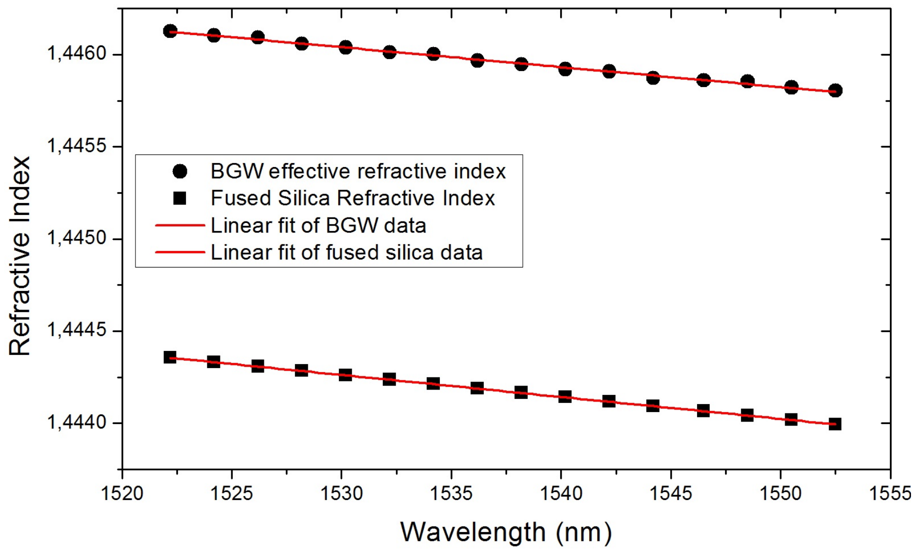

Figure 5.2: BGW and fused silica refractive index in function of wavelength for parallel writing polarization.

and perpendicular (b) polarization. From the figure it is clear that both BGWs possess birefringence that it is larger for a perpendicular writing polarization.

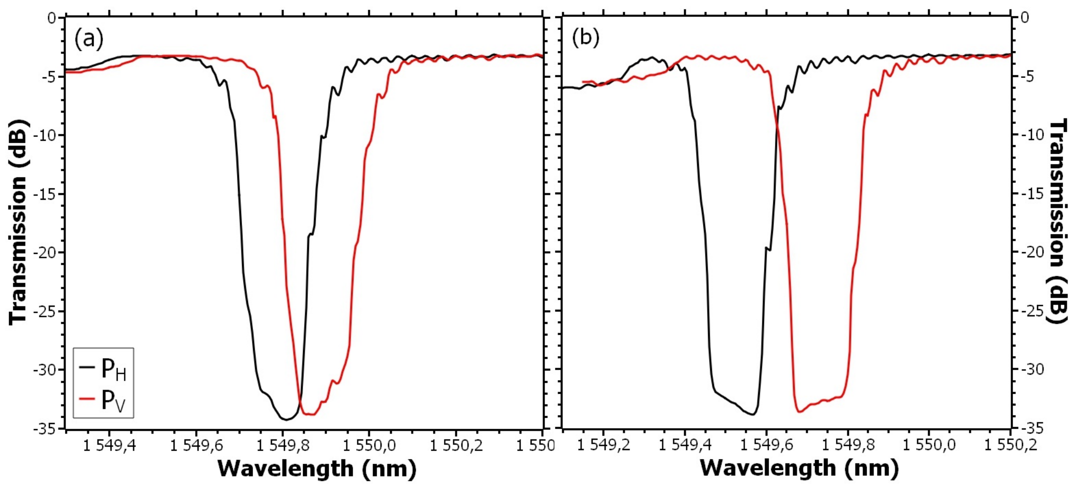

Figure 5.3: Transmission spectra of two BGWs written with parallel (a) and perpendicular (b) polarization and a 40 % duty cycle. The devices were analyzed with horizontal (black line) and vertical (red line) polarized light.

As already seen, the variation of the fabrication parameters can have strong effects on the BGW properties. In figure 5.4 the excess propagation loss, measured at 1551 nm, is displayed. The excess propagation loss is the difference in propagation loss between a waveguide with and without a grating. This value has been measured for wavelengths longer than the Bragg wavelength, outside the stopband, in order to avoid losses due to the coupling to higher order cladding modes. As can be seen, excess propagation loss decreases monotonically with increasing duty cycle for both writing polarizations. This is likely due to the decreasing grating roughness with increasing duty cycle, which decreases the light being scattered. It is also important to notice that the amplitude of the refractive index variation is key for grating strength since it also relies on Fresnel reflection, so, in order to have quality Bragg gratings, one must find a balance between these two variables. Since duty cycle refers to the proportion of written waveguide in a period (100 % meaning a normal waveguide), it is only natural that as this value tends to 100 % the excess loss tends to 0. However, it is odd to see that only an excess propagation loss around 3 dB/cm is found with a 10 % duty cycle, since at 0 % (nothing written) an infinite loss is obtained. Again, the lack of resolution seems to be the responsible for this characteristic, since the percentage effectively modified in one cycle is larger than the writing duty cycle.

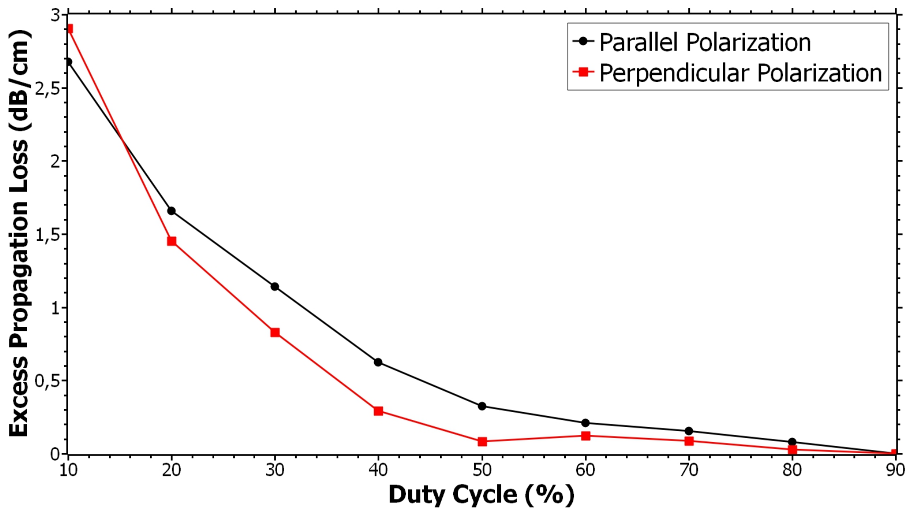

Figure 5.4: Excess propagation loss in function of duty cycle for BGWs fabricated with parallel and perpendicular polarization.

To fully understand how the insertion loss behaves with writing duty cycle, the mode field diameter was also measured to quantify the coupling loss. Figure 5.5 (a) displays the vertical and horizontal mode field diameter for BGWs fabricated with parallel and perpendicular polarization. For the horizontal mode field diameter it is seen that, for both writing polarizations, there is less confinement at lower duty cycles since a higher mode field diameter is obtained. Relatively to the vertical mode field diameter the analysis is not so obvious, but, for BGWs fabricated with parallel polarization, a higher mode field diameter is observed at both lower and higher duty cycles. With this data coupling loss was calculated (see subsection 3.2.2) and displayed in figure 5.5 (b). For both writing polarizations the coupling loss is seen to increase with increasing duty cycle to around 0.35 dB.

Relatively to the spectral behavior, grating strength, Bragg wavelength and birefringence results were analyzed and displayed in figure 5.6 for parallel and perpendicular writing polarizations. Figure 5.6 (a) shows that, for BGWs fabricated

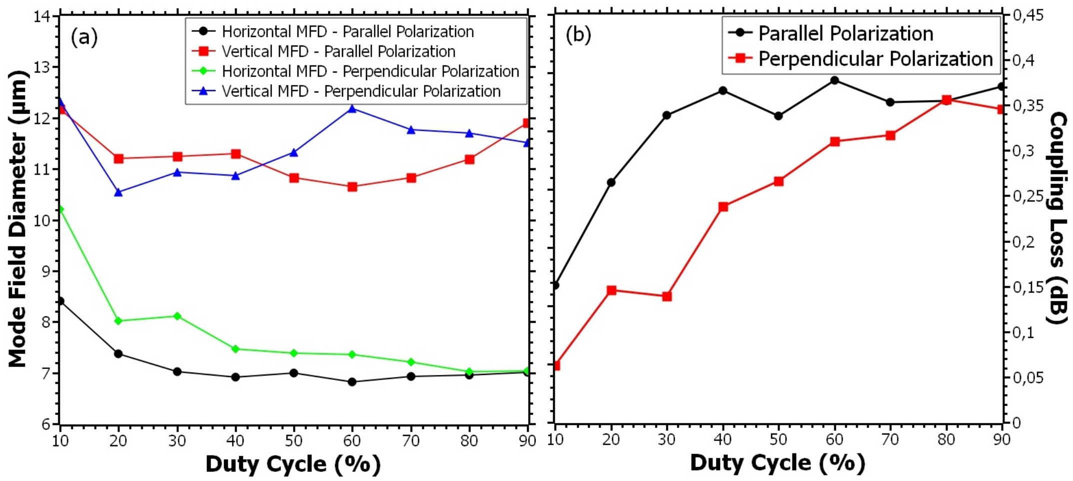

Figure 5.5: Horizontal and vertical mode field diameter (a), and coupling loss (b) in function of duty cycle for BGWs fabricated with parallel and perpendicular polarization.

with parallel polarization, the grating strength is around 31 dB for a grating fabricated with a 40 % duty cycle, reaching 6.5 dB for a grating fabricated with a 90 % duty cycle. In the case of the perpendicular writing polarization, the grating has maximum strength when fabricated at 50 % duty cycle, with the grating strength at 10 and 90 % duty cycle being around 23 dB and 3 dB, respectively. As was already explained, the grating strength decreases for high duty cycles due to an increasing overlap between two adjacent modified regions, that decrease the amplitude of the refractive index modulation. Regarding the behavior at lower duty cycles, for both writing polarizations (saturation and decrease in grating strength), this probably occurred due to the increased propagation loss and the characterization laser signal to noise ratio.

The Bragg wavelength of the fabricated BGWs was also analyzed and is displayed in figure 5.6 (b). As expected, the Bragg wavelength increases monotonically with duty cycle for both writing polarizations. This is explained by the simple fact that the average refractive index modification increases as laser exposure increases. Also, since the BGWs fabricated with parallel polarization have a higher Bragg wavelength than the perpendicular polarization written BGWs, it can be assumed that the refractive index modification is greater while writing with parallel polarization for the same writing parameters. Another interesting fact is that, for parallel polarization, the Bragg wavelength saturates with a duty cycle around 50 %. This agrees with the grating strength decreasing for duty cycles higher than 40 %, since the amplitude of the refractive index variation becomes smaller. The resolution of the refractive index modification can also be estimated by this saturation. Since the Bragg grating period is 536.1 nm and the Bragg wavelength saturates for a duty cycle larger than 50%, it is safe to say that the refractive index modification process has a resolution of approximately half of the Bragg grating period (268 nm). This implies that a duty cycle of 50 % has a refractive index modulation of a waveguide (100 % duty cycle), and as such, by doing a linear fit between 10 and 50 % and extrapolating to a duty cycle of -50 % (the new 0 % that corresponds to no modification), we can find a refractive index of n=1.4441, proving that the material is indeed fused silica. Some considerations on waveguide refractive index can also be made. Since the Bragg wavelength saturates at around 1549.97 nm, by using equation 5.1, to obtain the effective refractive index, and subtracting the refractive index of fused silica at 1550 nm, one gets the effective refractive index change to be $\Delta n_{eff} \approx 1.6 \times 10^{-3}$.

The amount of birefringence in the BGWs is also an important measurement because it tells us how large the behavior asymmetry, between horizontal and vertical input polarized light, in the fabricated devices is. Figure 5.6 (c) displays the birefringence, obtained from equation 5.3, for BGWs fabricated with parallel and perpendicular polarizations. As can be seen, birefringence has a maximum for a duty cycle around 30 % and two minima at both 10 % and 90 % duty cycle, for both writing polarizations. Birefringence lowers for duty cycles bellow 30 %, probably due to the lack of confinement. It was also found that, for a perpendicular writing polarization, birefringence is two to three times larger than for parallel polarization. The origin of the extra birefringence lies on the formation of nanogratings aligned with the writing direction. The birefringence measured is approximately $\Delta n = 5.6 \times 10^{-5}$ and $\Delta n = 1.48 \times 10^{-4}$, for a waveguide fabricated with parallel and perpendicular polarization, respectively.

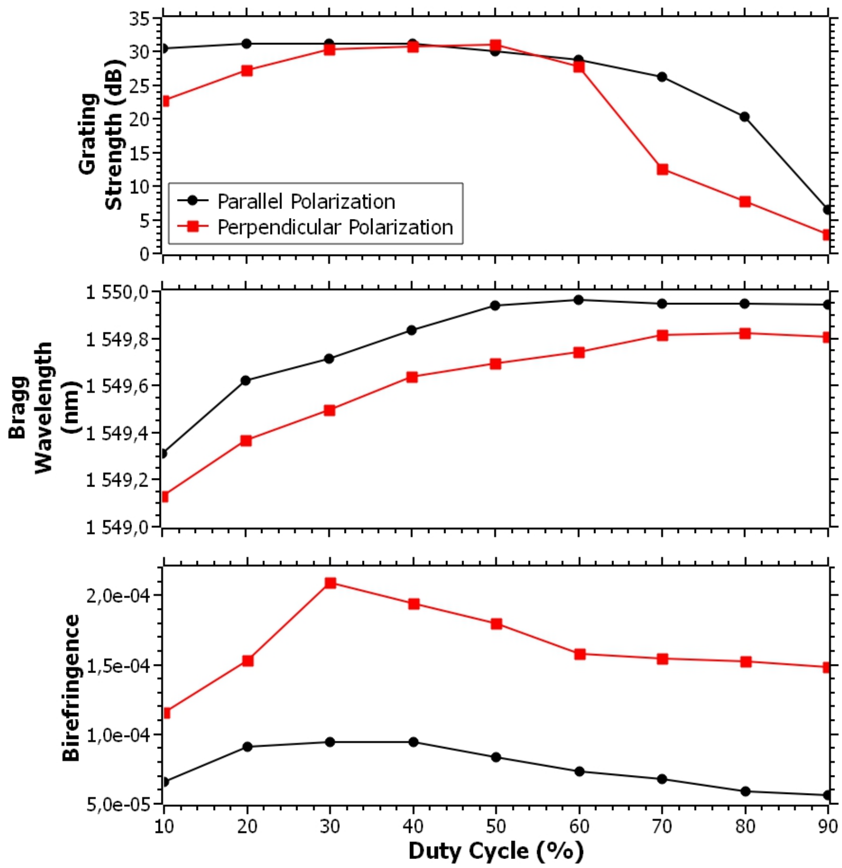

Figure 5.6: Grating strength (a), Bragg wavelength (b) and birefringence (c) as function of duty cycle, for BGWs fabricated with parallel and perpendicular polarizations.

To finalize, an analysis on the radiation mode loss was also made. Figure 5.7 shows the transmission and reflection spectra for BGWs fabricated with a duty cycle between 10 and 90 % (parallel writing polarization). The figure shows that despite the strength of the radiation mode loss present in the transmission spectra the light is not reflected, indicating that this light is indeed lost. Besides the grating strength behavior changing with duty cycle, it is also visible that the maximum strength of the radiation mode loss decreases monotonically with duty cycle, with a 8.5, 4.5 and 1 dB radiation mode loss being obtained for a duty cycle of 10, 50 and 90 %, respectively.

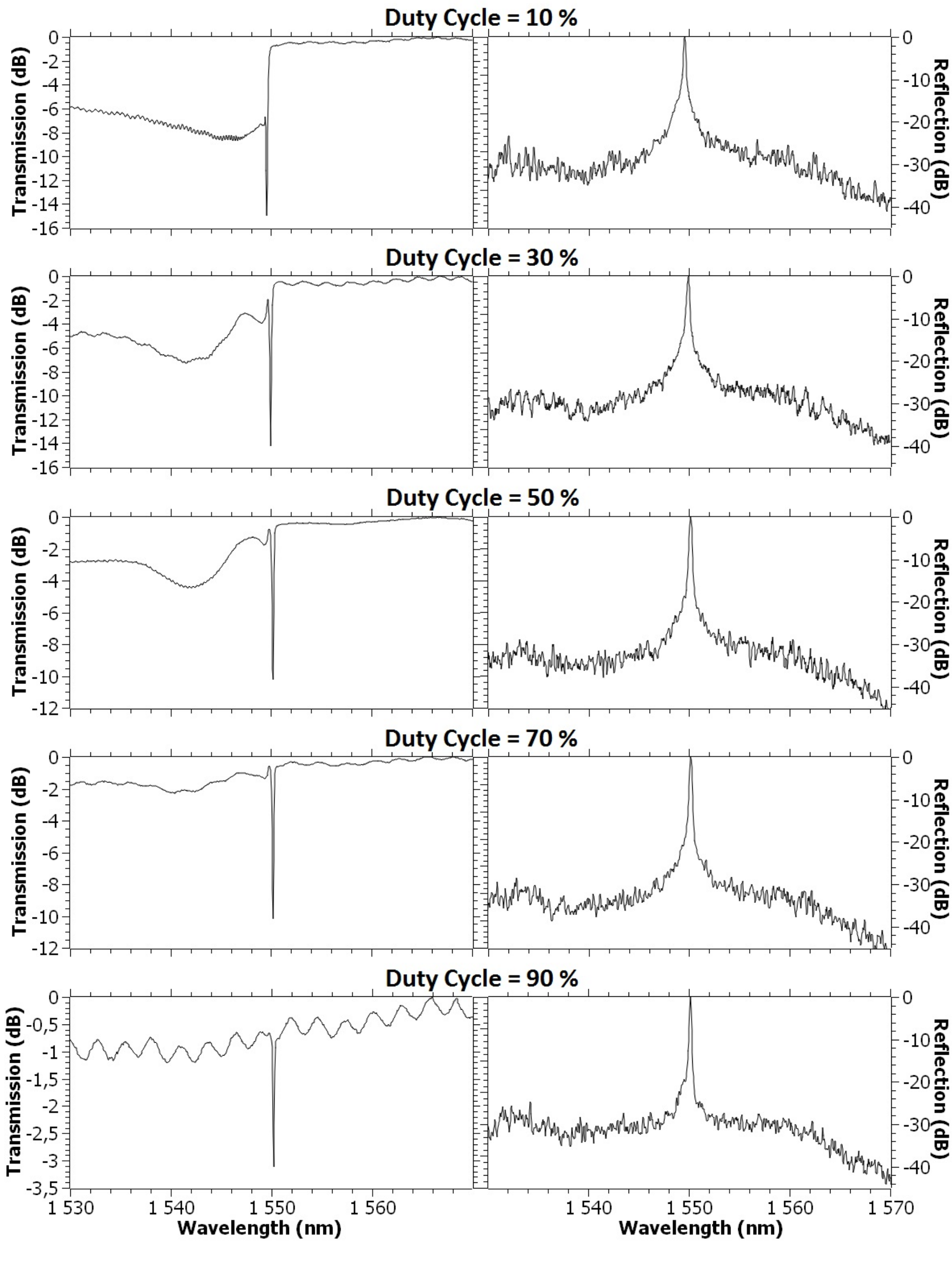

Figure 5.7: Transmission and reflection spectra of BGWs fabricated with parallel polarization and a duty cycle between 10 and 90 %.

5.2 Directional Couplers

Directional couplers are an important building block for the fabrication of more complex photonic devices, such as Mach-Zehnder interferometers, optical interleavers, power splitters, add-drop multiplexers and sensors. In this section detailed characterization results are presented for directional couplers fabricated with femtosecond laser direct writing. These devices were also characterized across the full telecom band (1300 to 1600 nm) showing the possibility for wavelength-division (de)multiplexing and polarization splitting.

5.2.1 Background

Directional couplers are devices defined by the existence of two single-mode waveguides that bend into a waist with a given waveguide separation and interaction length, as can be seen in figure 5.8. These devices can be analyzed by coupled mode theory and work as follows; light coupled into port 1 will travel along the single-mode waveguide and, as the waveguides get closer, light will start to be transferred to the other single-mode waveguide by evanescent coupling. If the waveguides are identical coupling will continue until all power is in the opposite waveguide and past that distance power will return to the original waveguide. This behavior is periodical and the interaction length defines the power splitting at the output ports 3 and 4.

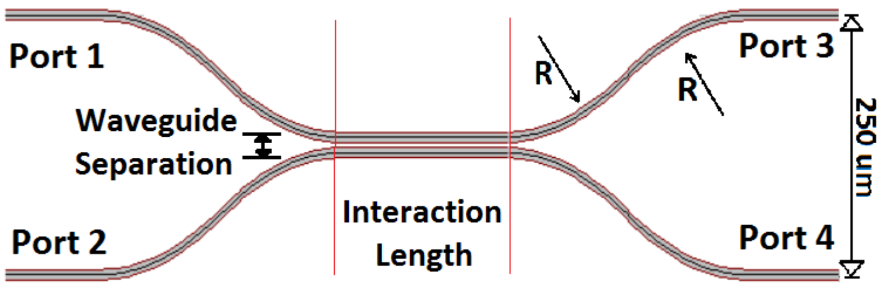

Figure 5.8: Directional coupler design.

The power transferred to the opposite waveguide can be expressed by the coupling ratio defined in equation 5.5, where the power at cross port, P_4, is normalized to the total output power (ports 3 and 4).

$$r = \frac{P_4}{P_3 + P_4} \tag{5.5}$$

The coupling ratio can also be described by equation 5.6, where K is the coupling coefficient, L the interaction length, and ϕ the phase acquired in the bending region.

$$r = sin^2(KL + \phi) \tag{5.6}$$

Since K and ϕ are wavelength and polarization dependent, the coupling ratio is also dependent on these variables. This fact enables the fabrication of WDM devices and polarization splitters based in the difference in coupling ratios between two wavelengths or orthogonal polarizations. In the case of polarization splitters the splitting contrast factor can be calculated from equation 5.7, where the subscript V and H are for vertical and horizontal polarized light, respectively.

$$\Delta r = |r_V - r_H| = |sin\left[(K_V - K_H)L + \phi_V - \phi_H\right] sin\left[(K_V + K_H)L + \phi_V + \phi_H\right]| \quad (5.7)$$

Directional couplers have many other uses and can be utilized to fabricate Mach-Zehnder interferometers [62] and add-drop multiplexers [63] for instance. The fabrication of directional couplers with femtosecond laser direct writing was already reported [9], as well as the fabrication of polarization beam splitters with directional couplers [64].

5.2.2 Fabrication Parameters

The femtosecond laser system used in the fabrication of the directional couplers was described in section 3.1. The second harmonic beam at λ = 515 nm with a, roughly, 250 fs pulse duration was focused inside the fused silica substrate, 50 μm below the surface, with a 0.55 NA aspheric lens.

To fabricate the directional couplers low loss optical waveguides were written using 250 nJ pulses while scanning the sample at a constant speed of 400 μm/s. The writing beam polarization was linear and parallel oriented to the scanning direction. These exposure conditions yielded waveguides with optimal insertion losses of 1.1 dB, for 2.5 cm long substrates, with a MFD of 12.3 μm x 7.1 μm, resulting in coupling losses of 0.37 dB per facet and propagation losses of 0.14 dB/cm. To avoid any extra losses, in comparison with straight waveguides, S-bends were designed with a 80 mm radius of curvature and a lateral offset of 125 μm, to yield a 250 μm output waveguide separation.

For this study the waveguide center-to-center distance in the coupling region was between 5 and 15 μm, and an interaction length between 0 and 12 mm, resulting in 12 to 25 mm long devices.

5.2.3 Results

In this work the power splitting was assessed as a function of interaction length and separation distance. Figure 5.9 shows the coupling ratio, from equation 5.9, of port 3 (1-r) and 4 (r), obtained using port 1 as input, in function of interaction length for separation distances of 5, 7.5, 10 and 15 μm at a wavelength of 1550 nm. The sinusoidal behavior is present for all separation distances tested, as expected, and the amplitude is close to the unity as expected for identical waveguides. The minimum coupling ratio obtained varies from 2.5 % (-16 dB), at 5 μm separation distance, to 0.07 % (-31.5 dB), at 15 μm separation distance. It is also relevant to refer that the couplers response is symmetrical despite the input being at port 1 or 2.

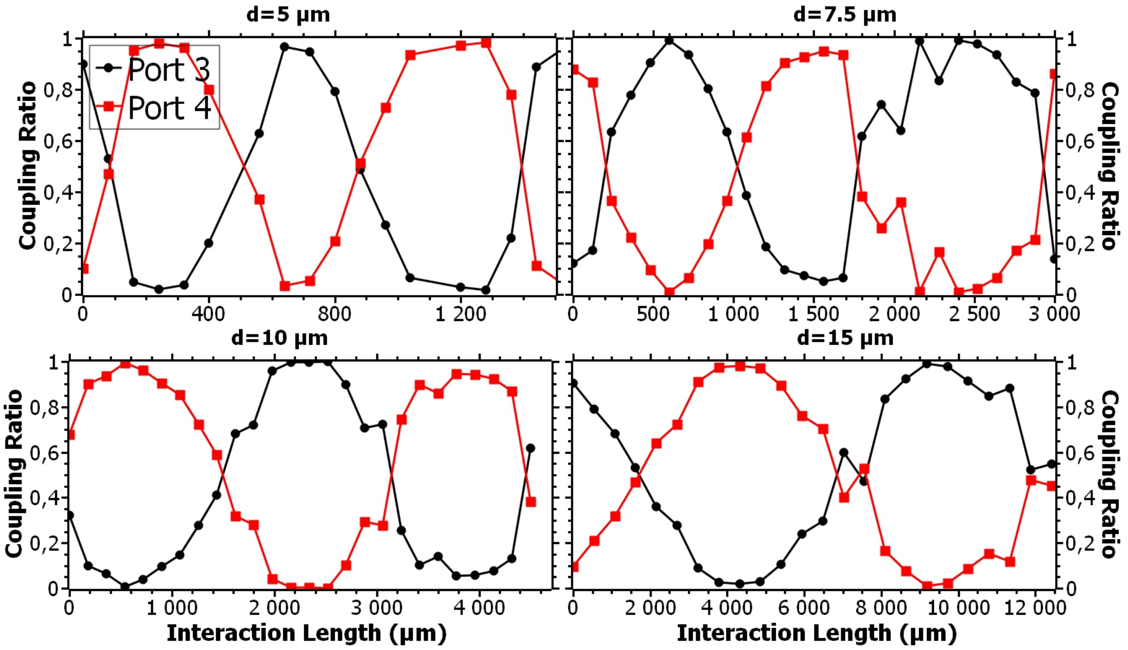

Figure 5.9: Coupling ratio in function of interaction length for waveguide separation distances of 5, 7.5, 10 and 15 μm.

The coupling length was also studied from the data represented in figure 5.9 and the result plotted in figure 5.10 (a) as a function of separation distance. As expected, the coupling length increases with separation distance, since the coupling coefficient decreases exponentially with increasing separation distance. For 5 μm separation distance a coupling length of around 0.5 mm was achieved, while for 15 μm separation distance a coupling length of approximately 5.6 mm was obtained. If the coupling coefficient decreases exponentially equation 5.6 shows that the beating length must increase exponentially, and from this an exponential growth was used to fit the beating length versus separation distance data. It is however important to notice that the phase accumulation depends on the separation distance, since the S-bend curvature radius is not zero and coupling also occurs in the bending region. Thus, to properly design the performance of the directional couplers, both coupling length and phase is needed.

The insertion loss was also analyzed for all directional couplers fabricated. In figure 5.10 (b) insertion loss is plotted in function of interaction length for all separation distances tested. For a separation distance of 5 μm the average insertion loss increases with interaction length, which indicates a degradation of the interacting waveguides due to an overlapping of the material modification. When the separation distance increases such overlapping ceases to exist and guiding occurs without any additional loss from the single waveguide case, as seen for separation distances of 7.5, 10 and 15 μm. The insertion loss for these 2.5 cm long devices is approximately 1.8 dB (with around 0.37 dB coupling loss per interface), value that almost equals the average 1.75 dB insertion loss of the reference linear waveguides written at the same time as the directional couplers. Since 2.5 cm waveguides with approximately 1.1 dB insertion loss were already developed in this thesis it is expected that directional couplers with much lower insertion losses can be fabricated.

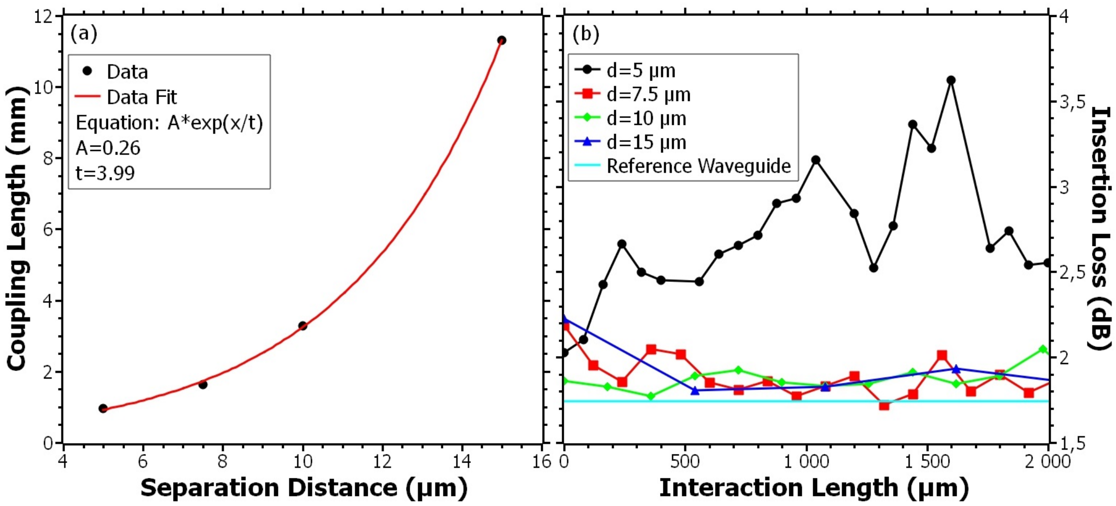

Figure 5.10: (a) Directional coupler coupling length and respective exponential growth fit in function of separation distance. (b) Insertion loss for directional couplers with a separation distance of 5, 7.5, 10 and 15 μm as a function of interaction length. Insertion loss of a reference waveguide is also displayed.

An important feature that was also tested was the directional couplers repeatability. This was tested while searching for a 3 dB (50%) directional coupler, and as such, only tested for 10 and 15 μm separation distance, since the slope for this cases is smaller giving less variation with interaction length. The results are presented in figure 5.11 where the previous and new set of directional couplers are plotted. In the new set the couplers were fabricated with an interaction length changing in intervals of 40 μm, around the 3 dB interaction length. Higher variation is found for a smaller separation distance, as expected, since separation distance fluctuation causes a performance deviation that is larger for larger coupling coefficients. With this data it is expectable that the performance fluctuations are even worse for the 7.5 and 5 μm separation distance couplers. From this work it was possible to obtain couplers with a splitting ratio of 44/56%, for 10 μm separation distance and 1.48 mm interaction length, and 51/49%, for 15 μm separation distance and 1.77 mm interaction length.

Since the waveguides fabricated by femtosecond laser direct writing are intrinsically birefringent (see section 5.1) it is expectable that the directional couplers behavior is also polarization dependent. To confirm this a study regarding input light polarization was made for directional couplers fabricated with a separation distance of 10 μm. In figure 5.12 the coupling ratio of port 4 is plotted as a function of interaction length for

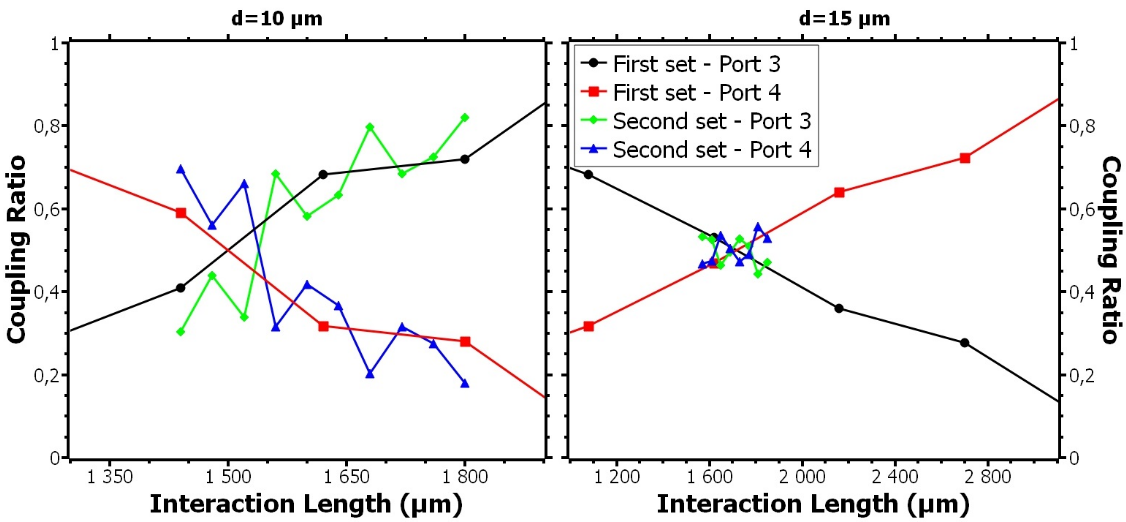

Figure 5.11: Coupling ratio for directional couplers fabricated with a separation distance of 10 and 15 μm. The first set corresponds to the first directional couplers fabricated to verify equation 5.6 and the second set to find the location of 3dB couplers and behavior variation.

horizontal and vertically polarized input light. A difference in coupling ratio is visible between orthogonal polarizations due to the effective interaction length being different for both input polarizations, since the refractive index for both polarizations is different.

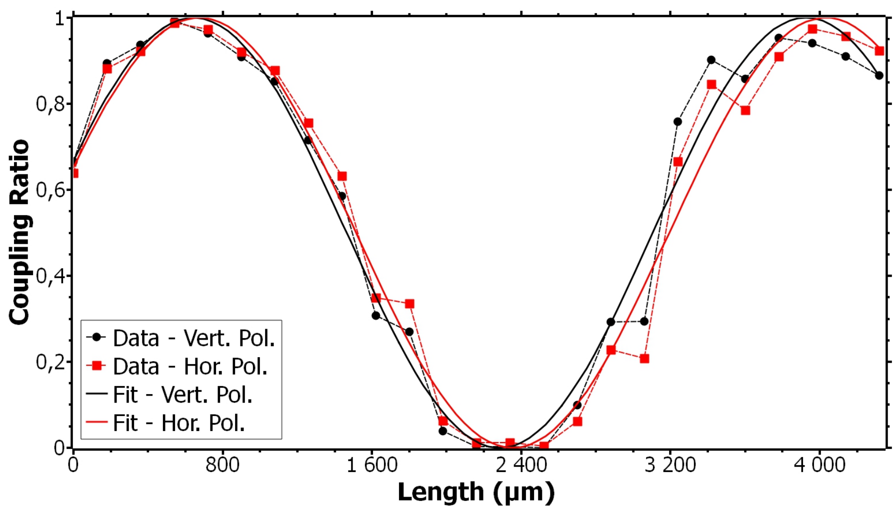

Figure 5.12: Measured coupling ratio as a function of interaction length for vertical polarized and horizontal polarized modes with corresponding fittings.

This difference in coupling ratio between horizontal and vertical input polarization is interesting because it unlocks the possibility to fabricate polarization beam splitters. To test this possibility an analysis on wavelength, from 1300 to 1600 nm, was made for directional couplers with a 10 μm waveguide separation. The measured data was fitted to equation 5.6 by a python code (see annex) using Levenberg-Marquardt algorithm, and the coupling coefficient, K, and phase, ϕ, obtained and displayed in figure 5.13. The coupling coefficient increases monotonically with wavelength, with a difference between coupling coefficients being observed. Since the coupling coefficient is smaller for lower wavelengths it is obvious that the phase acquired in the bending region also follows the same behavior.

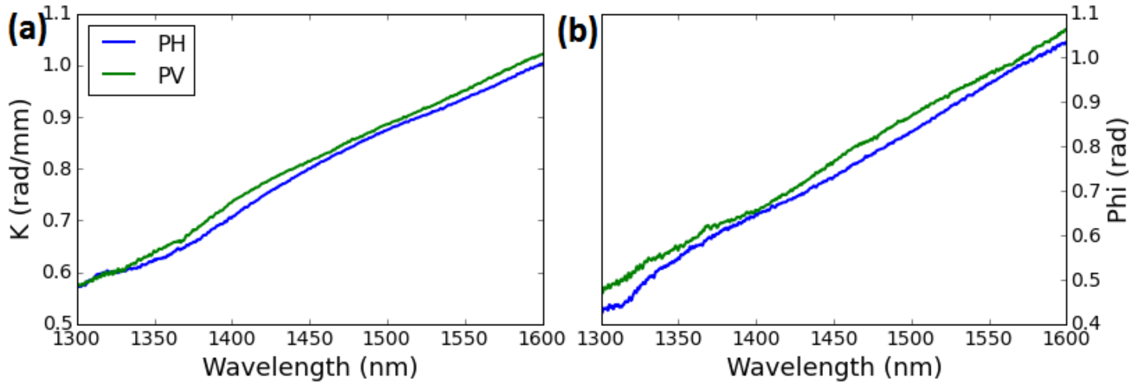

Figure 5.13: K (a) and ϕ (b) in function of wavelength, for vertical and horizontal polarized modes and 10 μm waveguide separation.

The coupling coefficient and phase acquired were used on equation 5.7 and the result plotted in figure 5.14. The figure shows the splitting contrast factor in function of interaction length and wavelength, where it can be seen that high splitting contrast factors in several wavelengths can be obtained for longer interaction lengths, thus enabling the fabrication of polarization beam splitters. In order to minimize the interaction length required for polarization splitting one can also use waveguides fabricated with perpendicular polarization, since these have around 3 times higher birefringence. Despite the higher propagation losses, the smaller device size required may reduce the total insertion losses.

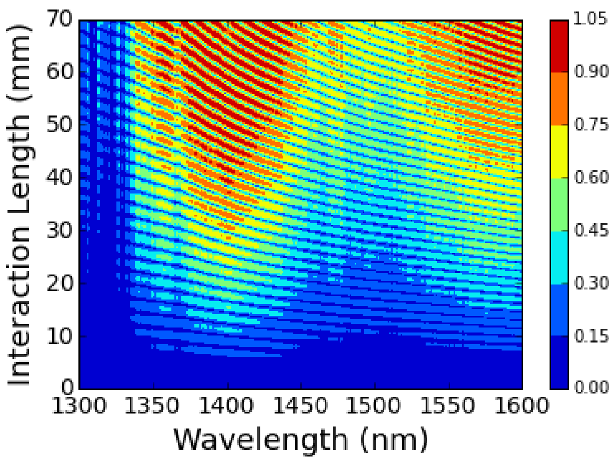

Figure 5.14: Splitting contrast factor, Δr, for directional couplers with 10 μm waveguide separation.

The coupling coefficient and phase acquired can also be used to calculate the coupling ratio for a given input light polarization. In figure 5.15 (a) the coupling ratio is displayed in function of interaction length and wavelength for vertical input polarization. From the figure one can see that directional couplers can also be used as wavelength-division (de)multiplexers. Figure 5.15 (b) shows a possible wavelength combination, where at 3.5 mm demultiplexing between 1375 and 1552 nm occurs.

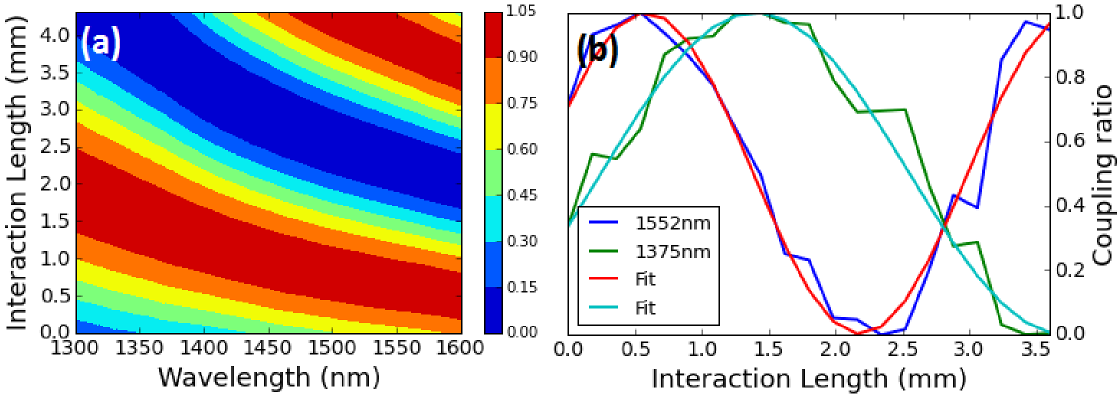

Figure 5.15: Coupling ratio in function of interaction length and wavelength (a), and example of demultiplexer for 1375/1552 nm (b).

5.3 Y-Junction Power Splitters

Integrated optical Y-junction power splitters have been used to demonstrate the potential of femtosecond laser direct writing in several materials, such as glasses, polymers and crystals [65]. This device has several advantages over other power splitters, like MMI devices and directional couplers, namely the broadband behavior and small device size. Despite these characteristics, only splitting for certain wavelengths has been investigated using femtosecond laser direct writing [66, 10, 67, 68]. This section describes the fabrication and optimization of Y-junction power splitters that fully explore its properties.

5.3.1 Background

Y-junctions are devices defined by the branching (hence the “Y”) of a single-mode waveguide into two equal single-mode waveguides. The light behavior in this device, in the splitting direction, is quite obvious: light entering through the single-mode waveguide is split evenly into both output branch waveguides. The main characteristic of this device, that differentiate it from other power splitters such as MMIs and directional couplers, is it achromatic behavior, which allows 3 dB power splitting over a large range of wavelengths. Y-junctions can also be combined together in binary tree structures. These allow a single input to be split into 2N outputs, all carrying equal power, using N branching levels. They can also be used in reverse, to combine 2N guided inputs in a single guided output. However, 100% efficiency is only achieved if all of the inputs have equal amplitude and phase, due to interference effects. Y-junctions are often used as optical power splitters or optical power combiners in modulators and switches made by joining two Y-structures by their output arms and introducing a phase shifter into one of them [53, 13]. Y-junctions are often used in integrated optical chips used for beam combining in astronomical interferometry. In this particular application the optical signals are broadband (astronomical bands are several hundreds of nanometers wide) and therefore achromatic behavior is essential [69].

High performance Y-junctions have already been demonstrated using Planar Lightwave Circuit (PLC) technology [70, 71, 72]. Junctions fabricated by PLC are desired because of the low insertion losses, high bandwidth and high uniformity between branches when the design is correct. However, to achieve these devices, many fabrication steps and a cleanroom environment are required. Production of Y-junctions by laser direct writing with UV lasers in germanium doped silica layers was demonstrated by Færch et al. [73], where problems of splitting uniformity also arrived due to depletion of photosensitivity in the branching area. The splitting ratio was adjusted by writing both branches at different doses. Femtosecond laser direct writing can be used instead of UV sources and pure silica material can be used as substrate. Femtosecond laser direct writing is a maskless, single step technique that allows the fabrication of integrated optical devices in several materials by localized nonlinear absorption. The fabrication of Y-junctions using this technique has already been reported [66, 10, 67, 68], however not enough attention has been invested in the fabrication of high performance devices. As such this work serves the purpose of fabricating high performance Y-junctions through the optimization of its design.

5.3.2 Fabrication

The femtosecond laser system used for the fabrication of the Y-junctions was described in section 3.1. The second harmonic beam at $\lambda = 515$ nm with an approximate 250 fs pulse duration was focused inside the fused silica substrate 50 μm below the surface with a 0.55 NA aspheric lens. To fabricate the Y-junctions low loss optical waveguides were used, writing with a 250 nJ pulse energy linearly polarized beam while scanning the sample at a constant speed of 400 μm/s. The writing beam polarization was oriented to be parallel to the scanning direction. These exposure conditions yielded waveguides with total insertion losses of 1.1 dB, for 2.5 cm long waveguides, with a MFD of 12.3 μm x 7.1 μm, resulting in coupling losses of 0.37 dB per facet and propagation losses of 0.14 dB/cm. To avoid any extra losses, in comparison with straight waveguides, S-bends were designed with a 80 mm radius of curvature and 125 μm offset, to yield a 250 μm output waveguide separation. These parameters translate into a 6.2 mm long Y-junction, mainly due to the S-bend length.

To study and optimize the Y-junctions fabrication parameters different tests were made. The most basic test was done with the branching starting at the same spot (point A, see figure 5.16 (a)); to do this the input waveguide is fabricated, followed by arm 1. To fabricate arm 2 the laser starts precisely on the same spot where arm 1 started (point A). The second test was made in the same way as the first, but in this case after the Y-junction is complete both arms are rewritten from the diverging point up to half S-bend (as seen in figure 5.16 (b)). In this test the number of passes per each arm is controlled. The third and last test corresponds to the situation where both arms are separated by a determined distance (figure 5.16 (c)). For this the input waveguide is fabricated, then the stage shifts laterally a given distance with the beam off and then starts to write arm 1. To fabricate arm 2 the stage re-position the substrate at a given opposite distance from the input waveguide and the arm is then written. It is important to notice that in all three cases the output waveguides are always separated by exactly 250 μm.

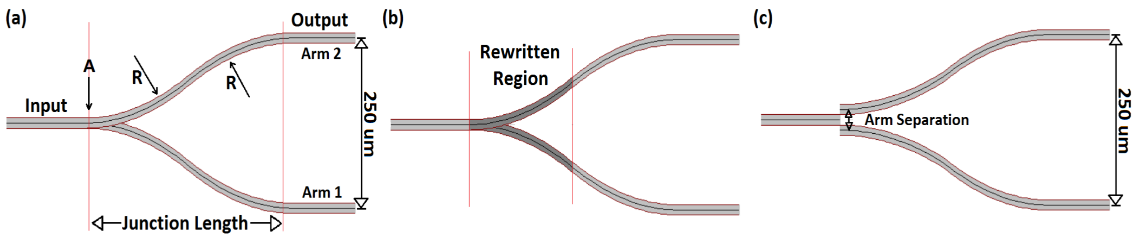

Figure 5.16: Y-junction design for the first test (a), with branching at the same spot, second test (b), with multiple arm writing, and third test (c), with initial arm separation.

5.3.3 Experimental Results and Discussion

To start, several basic Y-junctions employing the design of figure 5.16 (a) were fabricated. The characterization results, at 1550 nm, of the devices fabricated are shown in figure 5.17 (c), where power splitting, for both arms, is plotted as a function of the different Y-junctions fabricated. This graphic shows the existence of a consistent asymmetry in the fabricated junctions, since more power is flowing into arm 2 (the last arm to be written) than arm 1, with an $\approx$5% deviation from the ideal behavior (50%). The deviation can be explained by looking at figure 5.17 (b), where the last arm written is stronger. This effects result maybe from the fact that refractive index saturation was not reached during the first laser pass in the fabrication of the first arm, resulting in an asymmetric index distribution in the branching zone of the Y-junction. This asymmetry is also responsible for asymmetrical spectral arm behavior, as can be seen in the first graph of figures 5.19 and 5.21, feature that is not ideal for broadband power splitters. To correct these problems two approaches were tested, the first to perform multiple writings in the region of the diverging waveguides (figure 5.16 (b)), and the second to control the initial separation between diverging waveguides (figure 5.16 (c)).

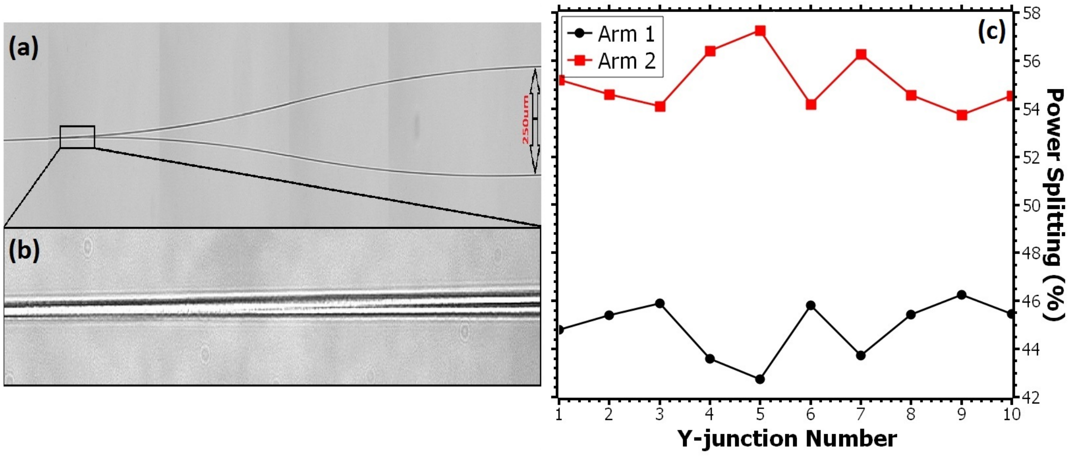

Figure 5.17: Optical microscope images of the top view of the Y-junctions fabricated (a), with particular attention to the divergence of both arms for regular Y-junctions (b). (c) Plot of power splitting, at 1550 nm, for several regular Y-junctions fabricated with equal parameters.

The idea behind rewriting the arms in sequence (arm 1, arm 2, arm 1, arm 2, ...) is to eliminate the junction asymmetry by saturating the refractive index change in that region (at the cost of some coupling loss between sections with different waveguide properties). This study was conducted by fabricating several Y-junctions with a different number of passes (2=(arm1, arm2), 3=(arm1, arm2, arm1), ...), from 2 to 20 passes. The devices fabricated were characterized at 1550 nm and the results are presented in figure 5.18. From the figure it is visible that the power splitting is very irregular with increasing number of passes, and that the junction loss increases almost linearly with the number of passes, from 0.77 dB to approximately 4.5 dB.

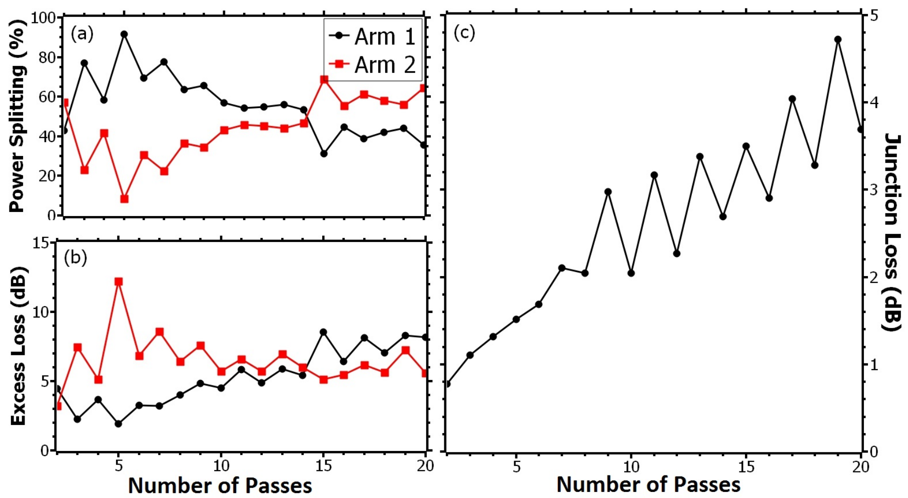

Figure 5.18: Analysis of Y-junctions, at 1550 nm, fabricated with different number of passes at the diverging point. Power splitting (a), excess loss (b) and junction loss (c) is plotted as a function of the number of passes.

An analysis on wavelength, from 1300 to 1600 nm, was also conducted (see figure 5.19). The figure shows that originally both arms have an asymmetric behavior, with arm 1 losing more power at lower wavelengths and arm 2 having a stable behavior, and that as the number of passes increases the symmetry increases. However, the behavior is still chaotic and far from ideal since these junctions are very dependent on wavelength. For these reasons it is safe to assume that this technique is not suited for junction asymmetry correction.

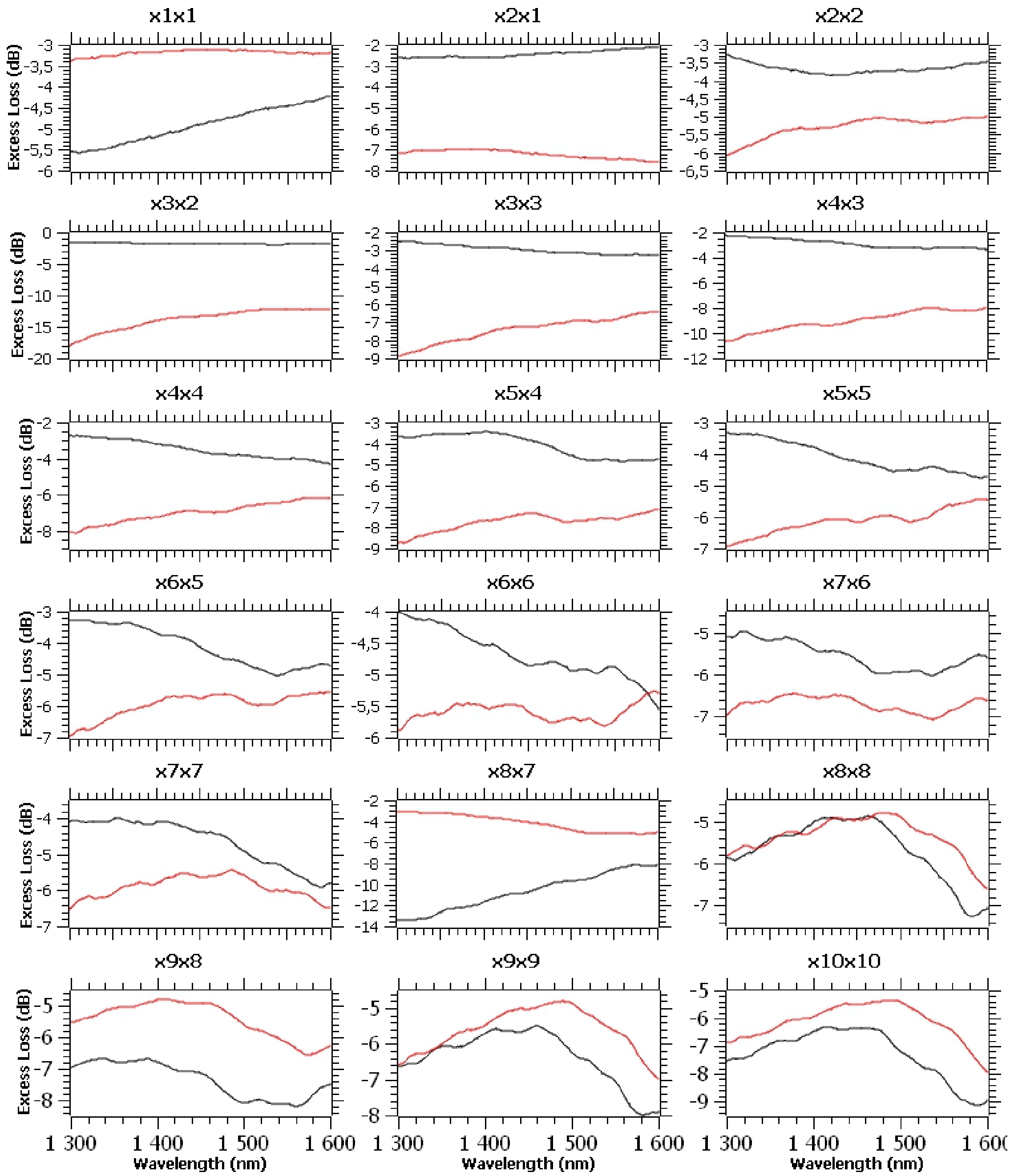

Figure 5.19: Spectral behavior of Y-junctions fabricated with different number of passings at the diverging point. Black-Arm 1; Red-Arm 2

Regarding the arm separation technique, the idea was to find the minimum separation that eliminates the junction asymmetry. This study was conducted by fabricating several Y-junctions with arm separations ranging from 0 μm (fully overlapped conventional Y-junction) to 15 μm. The devices fabricated were characterized at 1550 nm and the experimental results are presented in figure 5.20 together with the simulation results obtained with a 2D model and a 2.03 μm wide, 9.5×10^{-3} refractive index difference, waveguide using Rsoft. The results show that the power splitting becomes closer to the simulated 3 dB splitting ratio with increasing arm separation. It is also visible that the arm excess loss (insertion loss of one arm, including 3 dB splitting, minus the insertion loss of a reference waveguide) is relatively constant until 6 μm separation distance, reading 8 dB for 15 μm separation. The junction loss is also approximately constant up to 6 μm separation, increasing to 5 dB at 15 μm separation distance. This means that arm separation below 6 μm do not degrade the junction performance in what concerns loss. The experimental results agree very well with the simulated results.

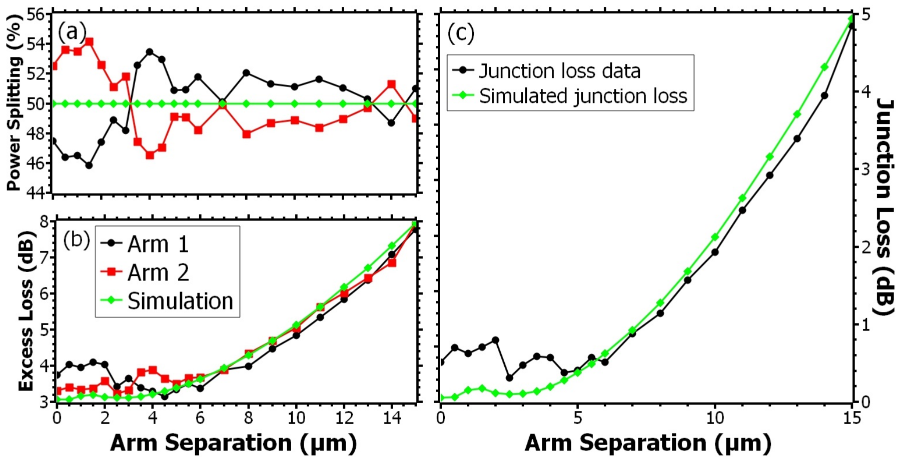

Figure 5.20: Analysis of Y-junctions, at 1550 nm, fabricated with different arm separation at the diverging point. Power splitting (a), excess loss (b) and junction loss (c) is plotted as a function of arm separation.

To further evaluate the quality of the junctions a chromatic analysis, from 1300 to 1600 nm, was also conducted (see figure 5.21). The figure shows that for no separation both arms do not follow the simulation results and have an asymmetric behavior, with arm 1 losing more power at lower wavelengths and arm 2 having a stable behavior. As the arm separation increases the symmetry increases until both arms show the simulated behavior (at 5 μm). This means that, with a separation distance greater than 5 μm, the writing of the second arm does not affect the first, and that the junction becomes symmetric. As already seen in the directional couplers (see section 5.2) the coupling coefficient increases for increasing wavelength, which means that for a small separation everything, from 1300 to 1600 nm, can couple to the output waveguides. However, as the separation increases the lower wavelengths will not be able to couple totally before the S-bends get further apart, thus the increased losses observed. As the arm separation increases even further even the higher wavelengths, that have higher coupling coefficients, won´t have enough interacting length to couple and will also suffer increased loss. It is also important to notice that the vertical shift observed when both arms have the same behavior is very likely due to misalignment of the output butt coupled fiber. In sum, taking the data into consideration, it is safe to assume that this technique is suited for junction asymmetry correction, with very good results being obtained for a 5 μm arm separation. The 5 μm arm separation junction has, at 1550 nm, a power splitting of 50.86:49.14, 0.4 dB junction loss, and an ideal 4.5 dB insertion loss (including the 3dB splitting loss) for a 2.5 cm long substrate. Regarding the spectral behavior, this junction shows only a small decrease of 0.48 dB from 1600 nm to 1300 nm, while maintaining the power splitting, thus proving to be a good broadband splitter.

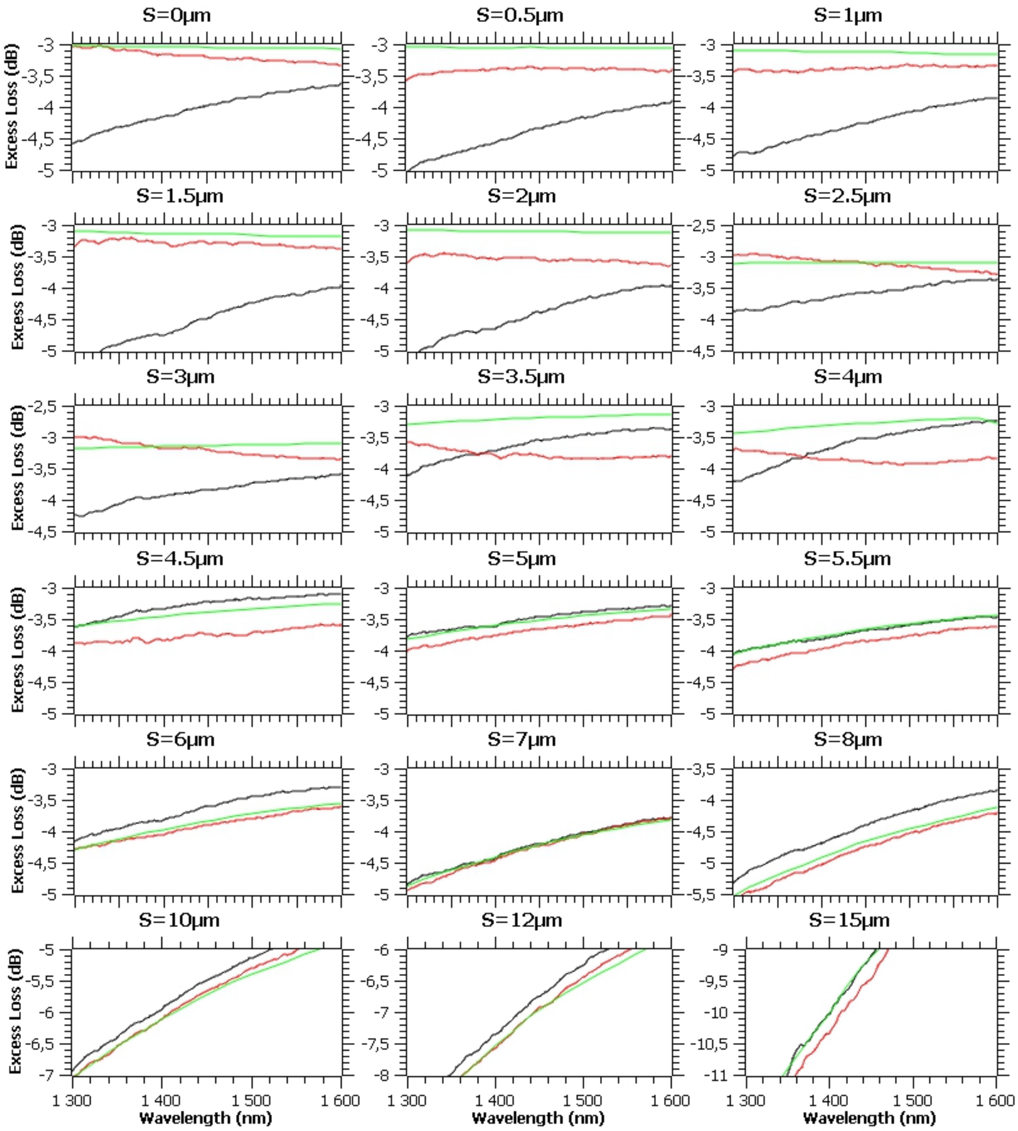

Figure 5.21: Spectral behavior of Y-junctions fabricated with different arm separations at the diverging point. Black-Arm 1; Red-Arm 2; Green-Simulations

5.4 Multimode Interference Devices

In this section, power splitting at 1550 nm is demonstrated using multimode interference (MMI) devices. This device has advantages over directional couplers and Y-junctions in particular situations. For large splitting ratios only a single MMI waveguide including output waveguides is required, instead of cascading a large number of directional couplers or Y-junctions. Such devices open the possibility for more compact photonic devices, which is beneficial for dense integration of photonic circuits where optical power splitters are key devices for optical communications and photonic information processing.

5.4.1 Background

Multimode interference devices are very important integrated optical components that can be used for several applications. These are usually composed by an input single-mode waveguide connected to a multimode waveguide and output single-mode waveguides. Light behavior in these devices is more complex than in other power splitters and works as follows: light propagating in the single-mode waveguide arrives at the multimode waveguide where a large number of modes is excited, due to an increase in normalized frequency (quantity proportional to the multimode waveguide width). The excited modes will then interfere between them as they propagate in the multimode waveguide, since now each one has a slightly different phase velocity. Due to this, constructive interference occurs in certain locations, depending on the multimode waveguide parameters. For simplicity, in this study a single-mode waveguide was connected to the center of the multimode waveguide. Since the input is placed on the axis of symmetry of the multimode waveguide only symmetrical modes can be excited, and the length at which the input field distribution is replicated is given by:

$$L_{MMI} = \frac{n_{eff}W^2}{\lambda}, \tag{5.8}$$

where n_{eff} is the multimode waveguide effective index, W the multimode waveguide width, and λ the working wavelength [53]. Self-imaging characteristics in MMI devices can be confirmed by Beam Propagation Method (BPM) simulations and it can be shown that N images are formed at $z = \frac{L_{MMI}}{N}$ for any integer N.

Such devices have many applications. For instance, MMI waveguides can be used as optical power splitters [74], couplers [75], wavelength division (de)multiplexers [76], and switches [77, 78]. These devices are usually fabricated by Planar Lightwave Circuit technology (PLC), however, to achieve these devices, many fabrication steps and a cleanroom environment is required. To our knowledge the fabrication of MMI devices using this technique has only been reported twice in literature [11, 79], and only the multimodal interference was investigated as a proof of concept for visible light. As such, this early work serves the purpose of fabricating MMI devices working in the telecommunication wavelengths.

5.4.2 Fabrication

The femtosecond laser system used for the fabrication of the MMI devices was described in section 3.1. The second harmonic beam at λ = 515 nm with a, roughly, 250 fs pulse duration was focused inside the fused silica substrate 50 μm below the surface with a 0.55 NA aspheric lens.

To fabricate the MMI devices several waveguides were written parallel to each other with a small separation between them. All waveguides were written with a 250 nJ pulse energy and linearly polarized beam while scanning the sample at a constant speed of 400 μm/s. The writing beam polarization was oriented to be parallel with the input waveguide.

For the fabrication of MMI devices three designs were tested, two where the MMI is written longitudinally (figure 5.22 (a)) and one where the MMI is written transversely (figure 5.22 (b)). In the case of the longitudinal MMIs the first design is based on the writing of longitudinal waveguides from border A to B with a given waveguide separation, while the second is based on the writing of the longitudinal waveguides from border A to the fifth waveguide from the center, followed of the ones from border B to the fifth waveguide from the center and then writing the central waveguides alternately from the closest to the borders until the center is reached. For the transversal MMIs the waveguides are written from border A to B in sequence from the input to output with a given separation distance. It should be noticed that the number of waveguides in this last design is far superior to the ones required in longitudinal designs. All MMI devices were fabricated in a way that the output plane is placed on a polished facet of the substrate.

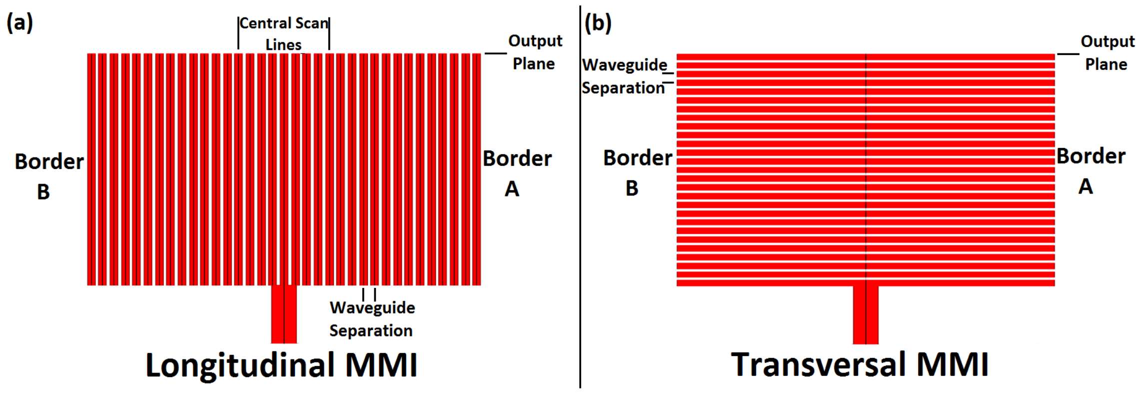

Figure 5.22: Design of the written longitudinal (a) and transversal MMIs (b).

5.4.3 Experimental Results and Discussion

As already seen in equation 5.8, MMI devices are highly dependent on width. Since femtosecond laser direct writing has not an infinite resolution it is to be expected that while doing N writings with a given waveguide separation S the total width is larger than $N \times S$.

Due to this fact tests had to be conducted to find the MMI writing width that matches the desired 50 μm. After some tests it was found that the desired 50 μm width was obtained with a writing width of roughly 47.5 μm.

Since the simulations made implied a multimode waveguide with a uniform refractive index, the separation between fabricated waveguides had to be controlled in order to obtain the simulations refractive index distribution. In figure 5.23 longitudinal and transversal MMI devices with a waveguide separation of 1 μm are displayed. From the figure it is possible to observe that with a waveguide separation of 1 μm the modification is not uniform since individual writing tracks are observable. Due to this the waveguide separation was reduced to 0.5 μm.

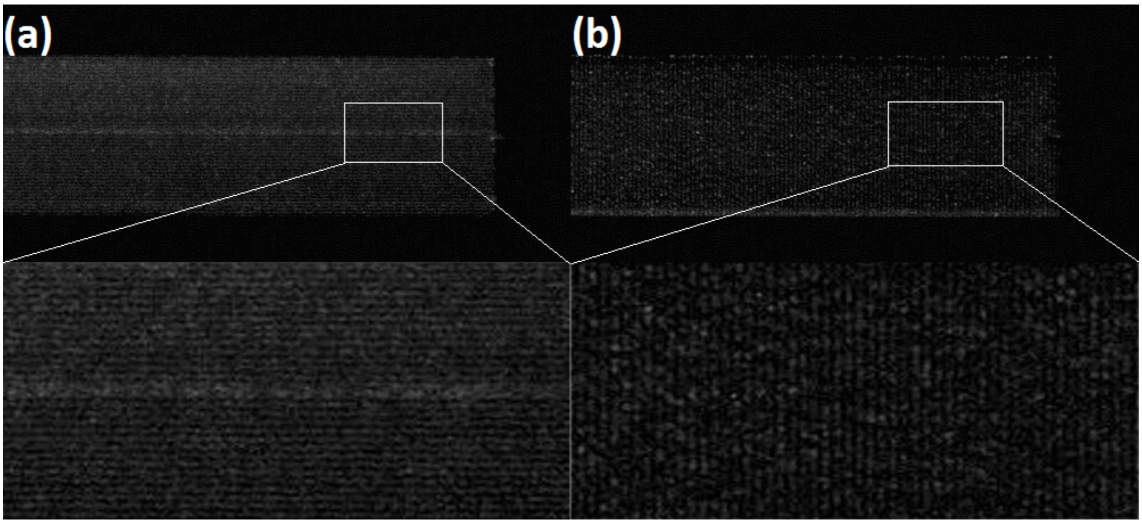

Figure 5.23: Dark field microscopy image of a longitudinal (a) and transversal (b) MMI device fabricated with a waveguide separation of 1 μm.

To fabricate MMI devices the length of the device is required. To determine this length simulations were conducted at 1550 nm with BPM (Rsoft) for 50 μm wide MMI devices (see figure 5.24 (a) to (d)). In this work 1:4, 1:3 and 1:2 power splitters were investigated and the device length was found to be roughly 690, 900 and 1350 μm, respectively. With the fabrication parameters set above several MMI devices were fabricated using the three designs specified in subsection 5.4.2. All these designs were tested in an effort to improve the device symmetry and decrease stresses originated by the fabrication process. The first longitudinal design and the transversal design showed very similar results in terms of modal distribution (first longitudinal design results are displayed in figure 5.24 (e) to (g)), while the second longitudinal design did not show the simulated behavior but rather random distributions.

This results can be explained by the microscope images in figure 5.25. From the top view images, in bright and dark field, it is possible to see that the second longitudinal design is not as uniform as the others. In the cross section view this becomes obvious since the guiding region is much more irregular. Apart from this, it is also interesting to

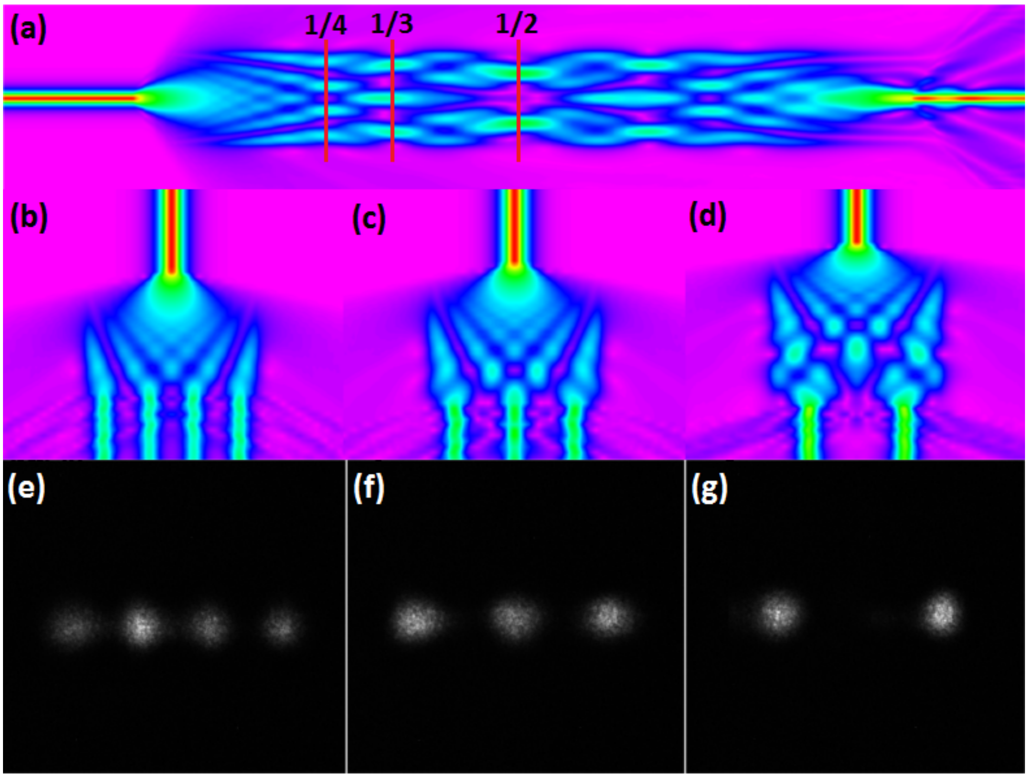

Figure 5.24: Figure showing the simulated behavior and the results obtained with the first longitudinal design for 50 μm width devices. First the 1:1 MMI behavior is simulated (a) and the 1:4 (b), 1:3 (c) and 1:2 (d) simulations obtained for a length of 690, 900 and 1350 μm respectively. From these simulated lengths the 1:4 (e), 1:3 (f) and 1:2 (g) behavior was obtained experimentally.

notice that the other two designs have problems. In the first longitudinal design all MMI devices fabricated had a crack in the corner of border B (last waveguide to be written). This probably happens due to stress building from the waveguides being written from border A to B. On the transversal design some problems can also be identified by the dark field image. This design was implemented since it avoids the stress buildup to the sides of the MMI device, which can be verified by the absence of cracks, but another problem arises due to hardware communication times. At border B more light is visible than at border A due to the laser being on while decelerating, which causes an alteration of the local properties. Another interesting fact is the stress concentration in the damaged region of the MMI device, seen in the DIC images, and the higher light scattering in this region for the longitudinal design when compared with the transversal design.

Taking everything up until now in consideration it would be easy to say that both the first longitudinal design and transversal design are optimal designs for MMI device fabrication. It is however important to look not only to the physical aspects and hardware constraints but to also be able to control the writing procedure and experimental apparatus. Figure 5.26 shows some defects, due to software limitations, obtained while writing devices with the transversal design. The cause to these defects are the software crashes, because

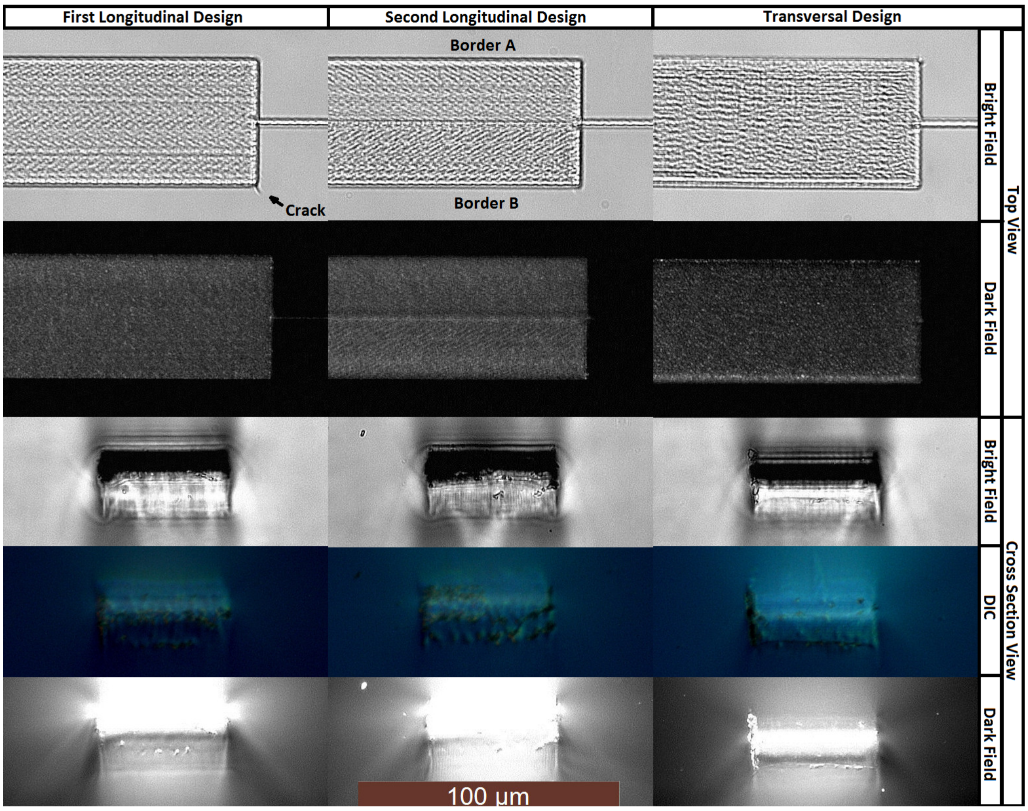

Figure 5.25: Top and cross section view microscopy images of the fabricated longitudinal and transversal MMI devices with a waveguide separation of 0.5 μm.

the transversal design requires, unlike the longitudinal design, many lines of Gerber code to fabricate a single device. For instance, a single 1:2 power splitter with this geometry and a spacing of 0.5 μm requires approximately 6470 lines of Gerber code while with the longitudinal design only 240 lines are required. It is also important to notice that for the longitudinal design these 240 lines are independent on device length but rather on width, while for the transversal design every 1 μm added to the device length 4 extra lines are needed.

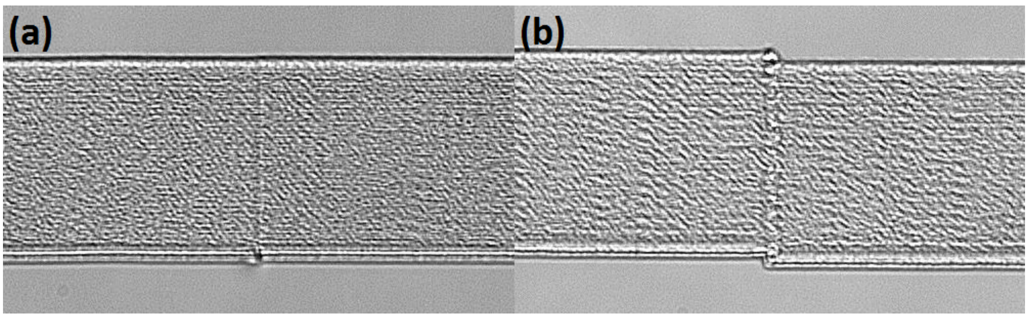

Figure 5.26: Bright field microscopy images of defects obtained in the transversal design due to stages stopping with laser on (a) and program reading error (b).

5.5 Optical Add-Drop Multiplexer

In this section, the fabrication of optical add-drop multiplexers working at around 1550 nm is demonstrated. The device was fabricated with a Mach-Zehnder configuration, using two 3 dB directional couplers as beam splitters and two uniform BGWs as spectral filters. Tests were made to see if application in 100 GHz networks is possible.

5.5.1 Background

An optical add-drop multiplexer (OADM) is a key element for wavelength-division multiplexing (WDM) optical networks. OADMs are devices used in telecommunication systems for routing different light channels in or out at different points of a optical network. In this context "add" and "drop" refer to the capability of the device to add a certain range of allowed wavelengths to a preexisting signal and the capability to remove a certain range of wavelengths, so that one or more channels can be added and/or read, respectively.

There are several configurations that enable the fabrication of OADM devices. Some of these configurations are depicted in figure 5.27, from which all require a Bragg grating as spectral filter and couplers or circulators as means to redirect light. Different configurations have different limitations; for instance, in configuration 1 an intrinsic insertion loss of 6 dB exists, in configuration 2 the circulators are difficult to fabricate, in configuration 3 the performance is compromised by the grating strength and coupler interaction length, and configuration 4 is sensitive to the signals path length and quality of the 3 dB couplers, since it is based on splitting and interference.

Furthermore, OADM devices can be fixed (are used to add or drop signals on specific WDM channels) or electronically reconfigurable (are used for the routing of channels selected at will). In this study the work is focused on the fabrication of fixed OADMs using configuration 4.

Configuration 4 is a configuration that allows low insertion loss and is almost identical to the first, where the unused ports are connected by a Bragg grating thus forming a Mach-Zehnder interferometer. Here, input light at port 1 is divided by the first 3 dB coupler into the top (symmetric) and bottom (antisymmetric) signal, where the bottom signal acquires a $\frac{\pi}{2}$ phase shift from crossing the coupler. These two signals will then be guided to the two identical Bragg gratings where the λ_B is back-reflected to the first coupler. Again at the coupler, the top and bottom signal will acquire another $\frac{\pi}{2}$ phase shift, causing the signals to be phase shifted by π at port 1, which leads to destructive interference, and 0 at port 4, leading to constructive interference and thus channel dropping. The transmitted wavelengths will propagate to the second 3 dB coupler where interference will again occur. Admitting that the optical path is identical, destructive interference is obtained at port 3 while constructive interference is obtained at port 2, meaning that all remaining channels are transmitted by the device without alterations. To add a channel at the λ_B the signal is launched in port 3. This signal will then be divided into two signals that will be reflected

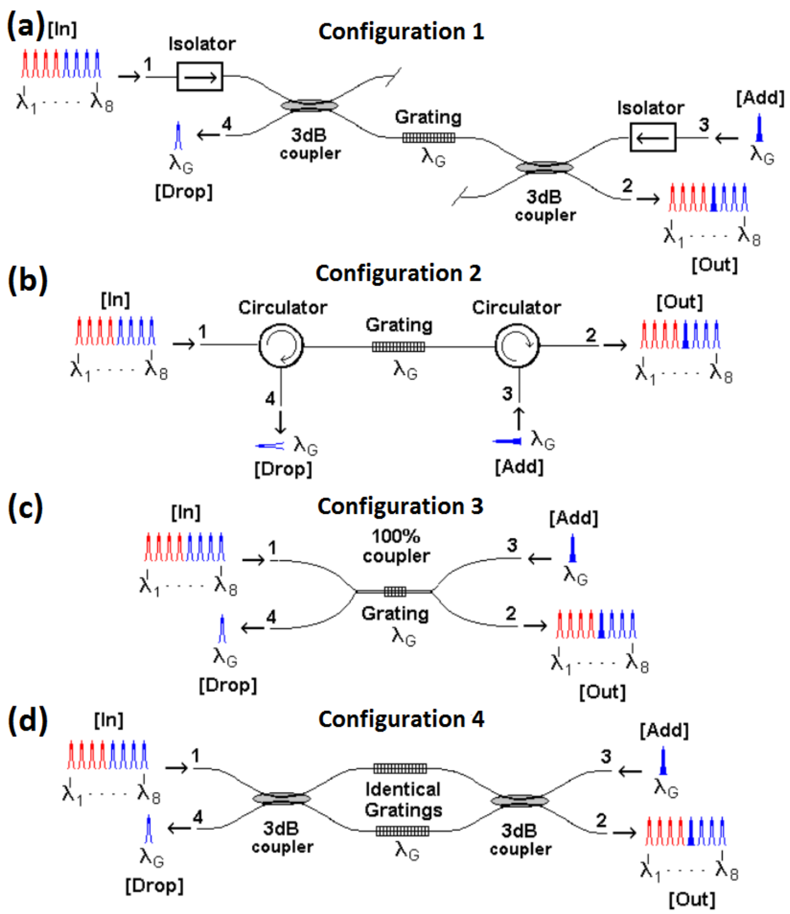

Figure 5.27: OADM device configuration based on two 3 dB couplers and a Bragg grating (a), two circulators and a Bragg grating (b), Bragg grating inscribed in the waist of a directional coupler (c), and on a Mach-Zehnder interferometer with two Bragg gratings (d) [80].

at the Bragg gratings and, similarly to the drop channel, interfere constructively to port 2 and destructively to port 3, thus adding a channel to the original signal.

As was already discussed, the difficulty on fabricating such devices is that, besides the problem of fabricating a coupler with high splitting uniformity, the optical path length must be very well adjusted in order to cause constructive interference at the drop and output ports. If we consider the phase accumulated during the optical path to be:

$$\phi = \kappa z = \frac{2\pi}{\lambda} n_{eff} L, \tag{5.9}$$

where λ is the light wavelength, n_{eff} the waveguide effective refractive index, and L the optical path length, it is trivial to deduce that the phase difference, $\Delta\phi$, between the light that travels at the top and bottom part of the device is given by:

$$\Delta\phi = \frac{4\pi n_{eff} \Delta L}{\lambda}, \tag{5.10}$$

where ΔL is the uniform grating positioning error. Now, considering a $\frac{\pi}{20}$ phase shift (9º) to be roughly in phase, it can be readily obtained that the grating positioning error can only be around 13.4 nm. Such a low positioning error cannot be regularly obtained and therefore device trimming (phase adjustments) in real time is required.

In order to integrate OADM devices in modern telecommunication networks several requirements have to be fulfilled by the Bragg gratings. First, the spectral width at 3 dB of the reflection peak has to comply with the ITU channel grid of 0.8 nm (100 GHz). This can be achieved by controlling the average coupling coefficient. Second, the grating strength has to be sufficiently high to ensure low intra-channel crosstalk (intra-channel crosstalk bellow -30 dB is desired). Third, only the selected channel should be dropped to avoid inter-channel crosstalk. For this side lobe suppression is important, to enable adjacent channel isolations higher than 20 dB.

The fabrication of these devices was already extensively reported and studied in planar lightwave circuits [63, 81, 82] and optical fibers [83]. However, the femtosecond laser direct writing technique has not yet been used for the fabrication of such devices.

5.5.2 Fabrication

To fabricate OADMs low loss optical waveguides were used, writing with a 250 nJ pulse energy linearly polarized beam while scanning the sample at a constant speed of 400 μm/s. The writing beam polarization was oriented to be parallel to the scanning direction. These exposure conditions yielded waveguides with optimum insertion losses of 1.1 dB, for 2.5 cm long substrates, with a MFD of 12.3 μm x 7.1 μm, resulting in coupling losses of 0.37 dB per facet and propagation losses of 0.14 dB/cm.

The device was fabricated in a 7.6 cm long substrate and its design is as shown in figure 5.28 (a). Directional couplers were used as 3 dB couplers, and, to avoid any extra losses, 80 mm curvature radius S-bends were employed. Furthermore, to obtain 3 dB splitting the directional couplers were fabricated with an interaction length of 1690 μm and 15 μm waveguide separation. The uniform Bragg gratings were fabricated with a temporal square modulation of 746.13 Hz, resulting in a periodicity of 536.1 nm, and a duty cycle of 40%. To obtain a grating strength of at least 30 dB a length of 2 cm was used on both gratings. It is also important to notice that 3 mm straight waveguides were placed between the ends of the directional coupler and the Bragg gratings. The main optical components are 5.4 cm long and as such straight waveguides, with a separation of 250 μm, were written to complement the optical path missing until the extremities of the substrate. The substrate was then cut at both ends, to meet size requirements of the polishing jig, and then polished in both facets. The final device obtained is 6 cm long and is displayed in figure 5.28 (b). To make the device easily usable v-grooves (FOFA-1022123116) were glued to the input/output ports with Norland optical adhesive 61 as seen in figure 5.28 (c). The glue was cured with an ultraviolet light source (Hamatsu LC8 L9588-02) in two steps. A short, uniform 10 second exposure, is used first to set the glue, followed by a longer cure time of approximately 15 minutes.

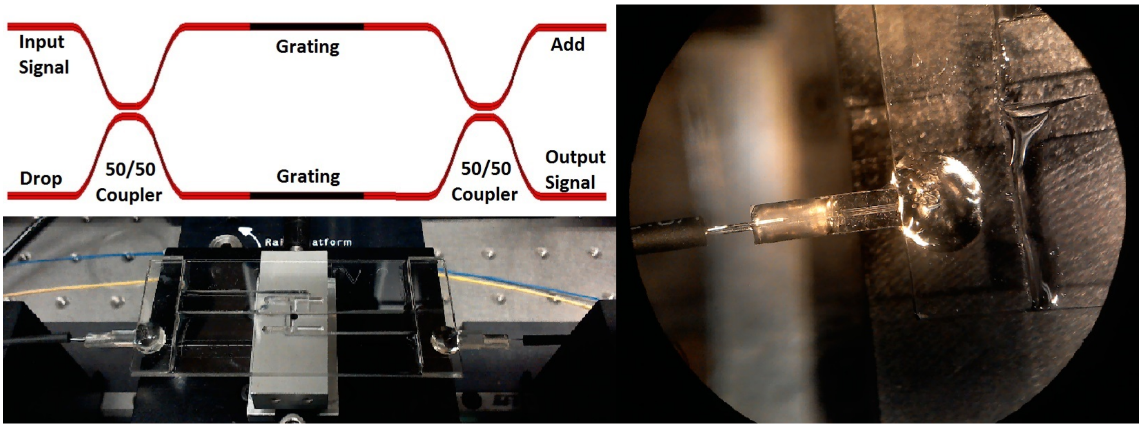

Figure 5.28: Optical add-drop multiplexer schematic (a) and fabricated device (b) with up close of one of the glued v-grooves (c).

5.5.3 Experimental Results and Discussion

For this study the best phase matched OADM was analyzed from the several that were fabricated, since real time phase adjustments were not yet applied. The input, drop, add and through-port spectra were measured around the Bragg wavelength (1549.67 nm) with a spectrometer, as described in section 3.2.4, and the results are displayed in figure 5.29. All these measurements were made to confirm if the OADM is working as intended or not. First, for a symmetrical device with 50/50 directional couplers, it is expected that the add and through port transmitted signal is zero and one, respectively, and, as can be seen, this condition was roughly met with a deviation of 7.5% from the ideal behavior. Second, the optical path difference of both arms, from the directional coupler to the BGW, has to be zero or a multiple of $\frac{\lambda}{2n_{eff}}$ to enable constructive interference. This condition was met for the drop-port side of the device, as can be seen by the 28 dB isolation between input and drop port, but, unfortunately, the same did not occur in the add side. This results enabled further analysis to see if the device would work in real WDM systems, but further work needs to be made towards phase adjustment and grating apodization (work that unfortunately was not made due to the lack of time).

The measured through-port and drop-port spectra of the fabricated OADM, with a uniform Bragg grating, are shown in figure 5.30 (a). The transmission spectra exhibit, at the Bragg wavelength, a dip lower than -30 dB (99.9%), enabling low intra-channel crosstalk. Relatively to the reflection spectra on the drop-port, the spectra corresponds to the usual uniform Bragg grating spectra with the undesired side lobes. The 3dB bandwidth is 0.24 nm (< 0.8 nm), so the fabricated device can be used in 100 GHz channel spacing WDM systems; however, a 20 dB side lobe suppression is only achieved for $\Delta\lambda = \pm 0.75$ nm, meaning that the adjacent inter-channel crosstalk barely satisfies the basic specifications. It is however important to notice that this analysis was made without polarization control, which would improve the performance of the device. Another problem present in this device is the coupling to cladding modes, visible in figure 5.30

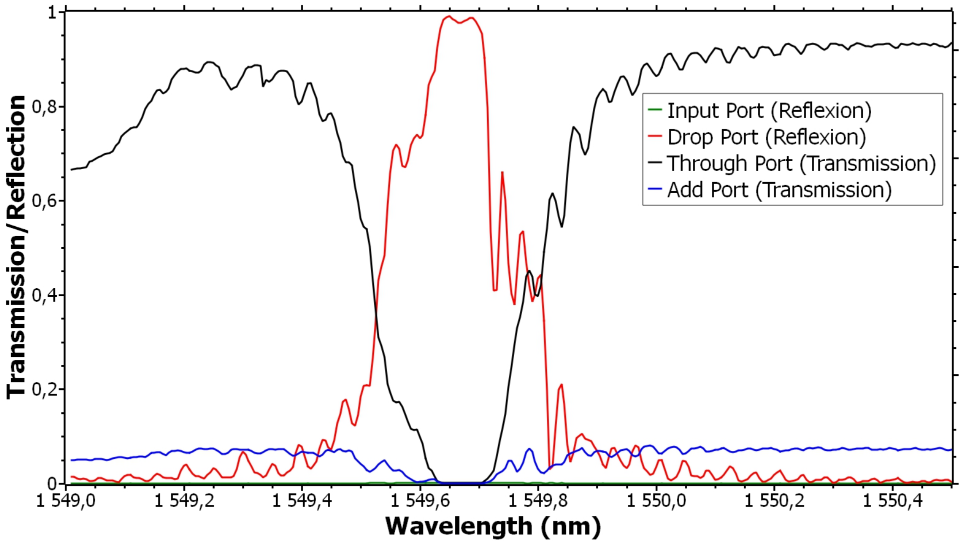

Figure 5.29: Measured reflection and transmission spectra of the four ports of an OADM around the Bragg wavelength.

(b), that will induce loss in channels with a lower wavelength than the Bragg wavelength. This arises from the low duty cycle used (40%) and can be solved with higher duty cycles. However, higher duty cycle Bragg grating waveguides require a higher length to maintain the same grating strength (due to a lower coupling coefficient), and, as such, since there were limitations in device size for the polishing, lower duty cycles had to be used.

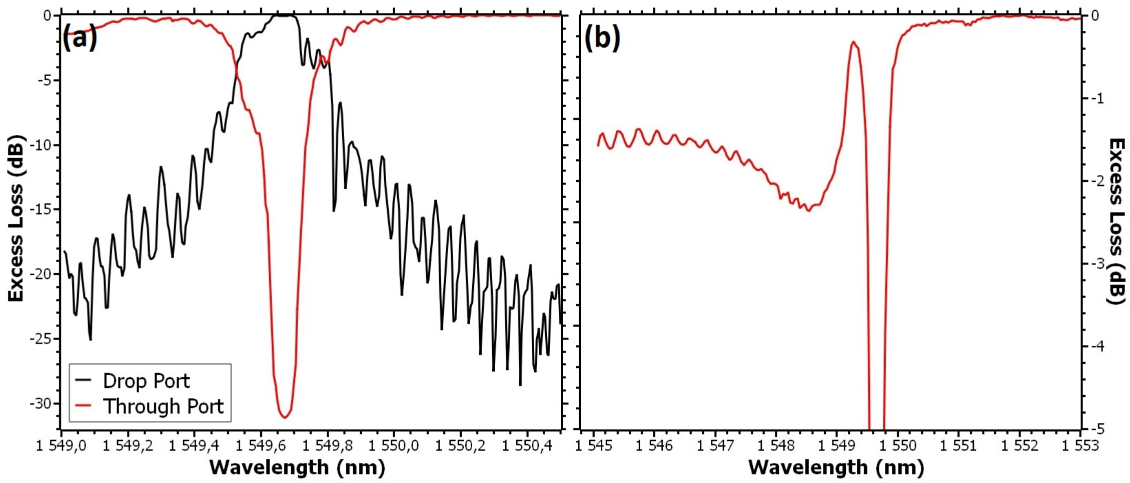

Figure 5.30: (a) Measured spectra of the through-port and drop-port responses of the fabricated OADM with a uniform grating. (b) Spectral behavior of the through-port, showing the coupling to cladding modes.

As already seen, uniform Bragg grating waveguides, defined by a constant coupling coefficient along the grating, exhibit undesired side lobes in the reflection spectrum that result in a partial drop of other channels. To reduce these lobes and enable more than 20 dB side lobe suppression grating apodization, defined by the Gaussian modulation of the coupling coefficient along the grating, can be used. This can be seen in figure 5.31, where the reflection signals from uniform and apodized Bragg gratings are simulated. In closer inspection it can also be seen that the transmission dip is reduced for the apodized grating, simply by the fact that for the same length the mean coupling coefficient is lower than in the uniform grating case. This means that the apodized Bragg gratings length has to be larger to compensate this fact, leading to a longer device. The fabrication of apodized Bragg grating waveguides with femtosecond laser direct writing was already demonstrated, where the modulation of the coupling constant was obtained by the transfer of the coupling strength to a wavelength half of the desired [60].

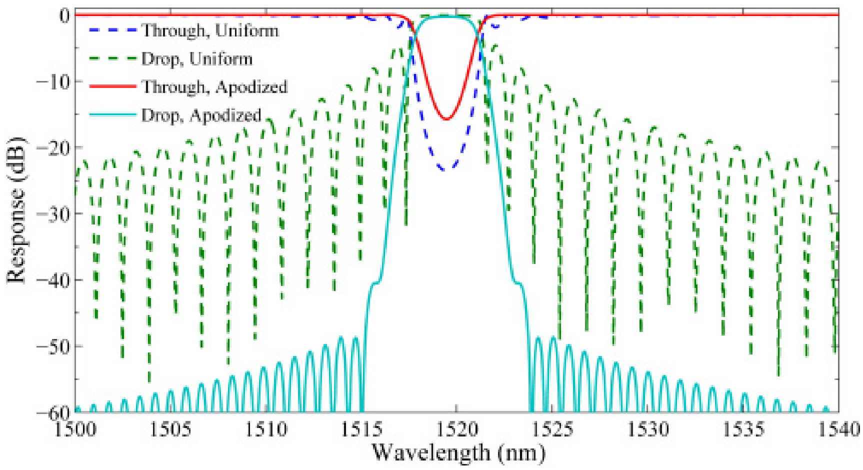

Figure 5.31: Simulated spectral responses of OADMs, one with a uniform grating and one with an apodized grating, illustrating the side-lobe suppression in the apodized grating design [84].

From equation 5.10 it was seen that the path difference between both arms has to be around 10 nm or less. As already demonstrated by Fernandes et al. [85], the birefringence of waveguides can be controlled by the fabrication of lateral stress tracks. This method enables real time phase trimming of the devices fabricated.

5.6 Conclusions

The implementation of the femtosecond laser direct writing technique on the fabrication of several passive integrated optical devices was successful, by using previous results on the fabrication of low loss waveguides.

The fabrication of uniform BGWs working at 1550 nm was demonstrated with a period of 536.1 nm and a 0.55 numerical aperture microscope objective. From the grating strength and birefringence behavior the resolution of the refractive index modification process was estimated to be around 270 nm. The modulation of the AOM frequency and duty cycle enabled easy tuning of the Bragg wavelength as well as grating strength and insertion loss, with grating strengths as high as 31 dB being obtained for smaller duty cycles. Laser polarization also shown to be a major variable regarding birefringence, with a birefringence two to three times larger being obtained for perpendicular polarization when in comparison with parallel polarization. The existence of radiation mode loss was verified, but this too can be controlled by the AOM duty cycle. This study also enabled complementary information about the characteristics of the best waveguide obtained in chapter 4 to be extracted. The chromatic dispersion was found to possess a similar behavior to the base material, and the effective refractive index change in the material to be $\Delta n_{eff} \approx 1.6 \times 10^{-3}$. The birefringence was approximately $\Delta n = 5.6 \times 10^{-5}$.

The fabrication of directional couplers was also demonstrated, with different coupling lengths being obtained for the different waveguide separations. No influence in insertion loss was observed for waveguide separations greater than 7.5 μm. Due to waveguide birefringence differences in coupling ratios were observed. This characteristic allows the capability to fabricate polarization beam splitters for several wavelengths. To finalize, wavelength-division (de)multiplexer devices were shown to be possible between several wavelengths, with demultiplexing between 1375 and 1552 being demonstrated.

A new design, based on arm separation, for the fabrication of Y-junction power splitters was tested and optimized. Subsequently, a novel 1 x 2 optical power splitter with relatively low loss, good uniformity and low wavelength dependent loss was fabricated with a 5 μm arm separation in a 2.5 cm fused silica substrate, enabling more complex binary tree structures with the same characteristics. The insertion loss (including 3 dB splitting loss), uniformity and wavelength dependent loss obtained were 4.5, 0.15 (50.86:49.14), and 0.48 dB respectively, in the wavelength range of 1300 to 1600 nm. The results obtained show the potential of femtosecond laser direct writing since each device requires only 2 minutes to be fabricated with the current writing parameters.

The fabrication of multimode interference devices, working at 1550 nm, was shown to be possible in fused silica with the femtosecond laser direct writing technique. Power splitting was achieved with experimental results proving to be in good agreement with BPM simulations. Splitters with a splitting ratio of 1:4, 1:3 and 1:2 were fabricated with a 50 μm width and a length of 690, 900 and 1350 μm, respectively. Due to time constraints the splitting uniformity was not investigated nor the fabrication of MMI devices with waveguides at the output to retrieve the power. However, this preliminary work shows the capability to fabricate more complex structures where the cross section has to be manipulated.

The fabrication of OADM devices, working in the C band, is reported in fused silica with the femtosecond laser direct writing. The device was built in a Mach-Zehnder interferometer configuration with two directional couplers as 3 dB couplers, and two uniform Bragg gratings as spectral filters. Performance wise, a 0.24 nm 3 dB bandwidth was obtained, enabling application in 100 GHz optical networks, with an intra-channel and adjacent inter-channel crosstalk of -30 and -20 dB, respectively. Future investigation in apodized Bragg gratings will enable further reduction of inter-channel crosstalk to the point where even smaller grid separations such as 50 GHz will be allowed. To our knowledge it is the first time that a device of such complexity was reported.

Chapter 6

Conclusions and Future Work

Femtosecond laser direct writing of optical devices in fused silica was explored during this work for the successful demonstration of low loss waveguides and low loss S-bends that allow more complex devices to be built. Using the optimal writing parameters enabled the fabrication of direct point-by-point first order uniform Bragg grating waveguides, that can be used in optical communications and sensors, and three different power splitters (directional couplers, Y-junctions and MMIs), that are the main basic components in complex integrated optical devices. In the end an add-drop multiplexer composed by two uniform Bragg gratings and two directional couplers was demonstrated for use in optical communications.

To ensure the fabrication of low loss optical devices the fabrication of waveguides was optimized using a laser pulse repetition rate of 500 KHz, at a wavelength of 515 nm, and a microscope objective with a 0.55 numerical aperture. The best waveguides found, in terms of insertion loss, were fabricated at a depth of 50 μm with a pulse energy of 250 nJ and a scan velocity of 400 μm/s, while using a polarization parallel to the scanning direction. For these conditions a propagation loss around 0.14 dB/cm was found with an elliptical mode distribution being responsible for the coupling loss of 0.37 dB. The propagation loss achieved is in line with the best results in literature[6, 7].

Most optical devices require bends to perform their tasks. To understand the evolution of the bend losses several arc shaped S-bends were fabricated while using the previous parameters set for linear waveguides. In these conditions the bend loss showed to be negligible for arcs with a curvature radii larger than 50 mm. From this data a curvature radius of 80 mm was set for the following devices in order to guarantee no extra losses.

The study of point-by-point first order uniform Bragg grating waveguides opened the possibility to the design of the spectral behavior, with applications in optical communications and sensors. The fabricated Bragg gratings showed a tunability of the grating strength with writing duty cycle, ranging from 31 to 0 dB, as well as a tunability of the birefringence with writing polarization, with birefringence being two to three times larger for perpendicular polarization. With this study the birefringence of waveguides fabricated with parallel and perpendicular polarization was also discovered to be $\Delta n =$

5.6×10^{-5} and $\Delta n = 1.48 \times 10^{-4}$, respectively. The resolution of the refractive index modification was estimated to be around 270 μm. The fabrication of a optofluidic sensor using the Bragg grating waveguides described here was demonstrated by a colleague.

To allow the fabrication of more complex optical devices power splitting was studied by testing three different types of devices. Several directional couplers were fabricated varying interaction length and waveguide separation, where the best behaved directional couplers were found at 15 μm separation distance. An analysis on wavelength was made and, due to waveguide birefringence, polarization beam splitters were shown to be possible. The variation of coupling coefficient with wavelength was also confirmed, which enabled the fabrication of wavelength-division (de)multiplexers. On the other hand, 2.5 cm long Y-junction devices were fabricated. The junction presented an asymmetric behavior which was corrected by employing an initial arm separation. The optimal arm separation was found to be 5 μm, where an insertion loss (including 3 dB splitting loss), uniformity and wavelength dependent loss of 4.5, 0.15 (50.86:49.14), and 0.48 dB were found, respectively, in the wavelength range of 1300 to 1600 nm. The fabrication of MMI devices with a width of 50 μm was also tested and good results achieved. One-to-four, one-to-three and one-to-two splitting behavior was demonstrated using the simulated MMI length.

To end this thesis a more complex device, that uses Bragg gratings and 3 dB directional couplers, was fabricated. For the fabrication of the add-drop multiplexer a Mach-Zehnder configuration was employed, being obtained a 0.24 nm 3 dB bandwidth and an intra-channel and adjacent inter-channel crosstalk of -30 and -20 dB, respectively, enabling applications in 100 GHz optical networks. Optical fibers mounted on silica v-groove blocks were permanently glued to the optical chip produced. It should be noticed that this device is, as far as I know, the first add-drop multiplexer fabricated using femtosecond laser direct writing.

The work demonstrated in this thesis shows the capabilities of femtosecond laser direct writing in the fabrication of integrated optical devices. Several building blocks for complex integrated optical devices were demonstrated and optimized. In the future, new developments should be made upon this work, such as:

- Fabricating apodized Bragg grating waveguides to greatly reduce the side lobes. These Bragg gratings will then be applied in devices such as add-drop multiplexers where low inter-channel crosstalk is important;

- Real time phase adjustments in add-drop multiplexers, to be able to correct the phase in each arm of the Mach-Zehnder individually;

- Test waveguide writing with the laser third harmonic (343 nm) to test if lower losses can be achieved;

- Use the slit beam shaping method to obtain a symmetrical waveguide cross-section.

Bibliography

[1] S. Suzuki and A. Sugita, “Recent Progress in Silica-based Planar Lightwave Circuits (PLCs)”, NTT Technical Review, vol. 3, no. 7, pp. 12-16, 2005.

[2] K. Davis, K. Miura, N. Sugimoto et al., “Writing waveguides in glass with a femtosecond laser”, Optics Letters, vol. 21, no. 21, pp. 1729–1731, 1996.

[3] S. Eaton, H. Zhang, M. Ng et al., “Transition from thermal diffusion to heat accumulation in high repetition rate femtosecond laser writing of buried optical waveguides”, Optics Express, vol. 16, no. 13, pp. 9443-9458, 2008.

[4] S. Li, Y. Ye and M. Wang, “Femtosecond laser written channel optical waveguide in Nd:YAG crystal”, Optics & Laser Technology, vol. 58, pp. 89-93, 2014.

[5] S. Sowa, W. Watanabe, T. Tamaki et al., “Symmetric waveguides in poly(methyl methacrylate) fabricated by femtosecond laser pulses”, Optics Express, vol. 14, no. 1, pp. 291-297, 2006.

[6] Y. Nasu, M. Kohtoku and Y. Hibino, “Low-loss waveguides written with a femtosecond laser for flexible interconnection in a planar light-wave circuit”, Optics Letters, vol. 30, no. 7, pp. 723-725, 2005.

[7] S. Eaton, H. Zhang, P. Herman et al., “Heat accumulation effects in femtosecond laser-written waveguides with variable repetition rate”, Optics Express, vol. 13, no. 12, pp. 4708-4716, 2005.

[8] H. Zhang, S. Eaton and P. Herman, “Single-step writing of Bragg grating waveguides in fused silica with an externally modulated femtosecond fiber laser”, Optics Letters, vol. 32, no. 17, pp. 2559-2561, 2007.

[9] S. Eaton, W. Chen, L. Zhang et al., “Telecom-Band Directional Coupler Written With Femtosecond Fiber Laser”, Photonics Technology Letters, vol. 18, no. 20, pp. 2174-2176, 2006.

[10] J. Liu, Z. Zhang, S. Chang et al., “Directly writing of 1-to-N optical waveguide power splitters in fused silica glass using a femtosecond laser”, Optics Communications, vol. 253, pp. 315-319, 2005.

[11] L. Da-Yong, L. Yan, D. Yan-Ping et al., “Transverse Writing of Multimode Interference Waveguides inside Silica Glass by Femtosecond Laser Pulses”, Chinese Physics Letters, vol. 25, no. 7, pp. 2500-2503, 2008.

[12] T. Calmano, J. Siebenmorgen, O. Hellmig et al., “Nd:YAG waveguide laser with 1.3 W output power, fabricated by direct femtosecond laser writing”, Applied Physics B, vol. 100, no. 1, pp. 131-135, 2010.

[13] A. Crespi, Y. Gu, B. Ngamsom et al., “Three-dimensional Mach-Zehnder interferometer in a microfluidic chip for spatially-resolved label-free detection”, Lab on a Chip, vol. 10, no. 9, pp. 1167-1173, 2010.

[14] N. Bellini, K. Vishnubhatla, F. Bragheri et al., “Femtosecond laser fabricated monolithic chip for optical trapping and stretching of single cells”, Optics Express, vol. 18, no. 5, pp. 4679-4688, 2010.

[15] R. Osellame, V. Maselli, R. Vazquez et al., “Integration of optical waveguides and microfluidic channels both fabricated by femtosecond laser irradiation”, Applied Physics Letters, vol. 90, no. 23, pp. 231118, 2007.

[16] Y. Bellouard, A. Said, M. Dugan et al., “Monolithic Three-Dimensional Integration of Micro-Fluidic Channels and Optical Waveguides in Fused Silica” MRS Proceedings, vol. 782, 2011.

[17] A. Ostendorf and B. Chichkov, “Two-Photon Polymerization: A New Approach to Micromachining”, Photonics Spectra, vol. 40, no. 10, pp. 72-79, 2006.

[18] Y. Hibino, “Silica-Based Planar Lightwave Circuits and Their Applications”, MRS Bulletin, vol. 28, no. 5, pp. 365-371, 2003.

[19] L. Fernandes, “Birefringence and Bragg grating control in femtosecond laser written optical circuits”, Ph.D. thesis, 2012.

[20] L. Huang, P. Salter, M. Karpinski et al. “Waveguide fabrication in KDP crystals with femtosecond laser pulses”, Applied Physics A, vol. 118, no. 3, pp. 831-836, 2014.

[21] K. Yamada, W. Watanabe, T. Toma et al., “In situ observation of photoinduced refractive-index changes in filaments formed in glasses by femtosecond laser pulses”, Optics Letters, vol. 26, no. 1, pp. 19-21, 2001.

[22] W. Watanabe, “Femtosecond filamentary modifications in bulk polymer materials”, Laser Physics, vol. 19, no. 2, pp. 342-345, 2009.

[23] M. Beresna, M. Gecevicius and P. Kazansky, “Ultrafast laser direct writing and nanostructuring in transparent materials”, Advances in Optics and Photonics, vol. 6, no. 3, pp. 293-339, 2014.

[24] M. Ams, G. Marshall, D. Spence et al., “Slit beam shaping method for femtosecond laser direct-write fabrication of symmetric waveguides in bulk glasses”, Optics express, vol. 13, no. 15, pp. 5676-5681, 2005.

[25] R. Osellame, S. Taccheo, M. Marangoni et al., “Femtosecond writing of active optical waveguides with astigmatically shaped beams”, Journal of the Optical Society of America B, vol. 20, no. 7, pp. 1559-1567, 2003.

[26] H. Huang, L. Yang and Jian Liu, “Femtosecond fiber laser direct writing of optical waveguide in glasses”, Proceedings of SPIE, 2011.

[27] B. Stuart, M. Feit, S. Herman et al., “Nanosecond-to-femtosecond laser-induced breakdown in dielectrics”, Physical Review B, vol. 53, no. 4, pp. 1749-1761, 1996.

[28] R. Gattass and E. Mazur, “Femtosecond laser micromachining in transparent materials”, Nature Photonics, vol. 2, no. 4, pp. 219-225, 2008.

[29] L. Keldysh, “Ionization in the field of a strong electromagnetic wave”, JETP, vol. 20, no. 5, pp. 1307-1314, 1965.

[30] C. Schaffer, A. Brodeur and E Mazur, “Laser-induced breakdown and damage in bulk transparent materials induced by tightly focused femtosecond laser pulses”, Measurement Science and Technology, vol. 12, no. 11, pp. 1784-1794, 2001.

[31] M. Ams, G. Marshall, P. Dekker et al., “Investigation of ultrafast laser-photonic material interactions: Challenges for directly written glass photonics”, IEEE Journal on Selected Topics in Quantum Electronics, vol. 14, no. 5, pp. 1370-1388, 2008.

[32] K. Miura, J. Qiu, H. Inouye et al., “Photowritten optical waveguides in various glasses with ultrashort pulse laser”, Applied Physics Letters, vol. 71, no. 23, pp. 3329-3331, 1997.

[33] E. Glezer and E. Mazur, “Ultrafast-laser driven micro-explosions in transparent materials”, Applied Physics Letters, vol. 71, no. 7, pp. 882-884, 1997.

[34] S. Juodkazis, K. Nishimura, S. Tanaka et al., “Laser-Induced Microexplosion Confined in the Bulk of a Sapphire Crystal: Evidence of Multimegabar Pressures”, Physical Review Letters, vol. 96, no. 16, pp. 166101, 2006.

[35] L. Sudrie, M. Franco, B. Prade et al., “Writing of permanent birefringent microlayers in bulk fused silica with femtosecond laser pulses”, Optics Communications, vol. 171, pp. 279-284, 1999.

[36] Y. Shimotsuma, P. Kazansky, J. Qiu et al., “Self-organized nanogratings in glass irradiated by ultrashort light pulses”, Physical Review Letters, vol. 91, no. 24, pp. 247405, 2003.

[37] A. Zoubir, C. Lopez, M. Richardson et al., “Femtosecond laser fabrication of tubular waveguides in poly(methyl methacrylate)”, Optics letters, vol. 29, no. 16, pp. 1840-1842, 2004.

[38] F. Chen and J Vázquez de Aldana, “Optical waveguides in crystalline dielectric materials produced by femtosecond-laser micromachining”, Laser & Photonics Reviews, vol. 8, no. 2, pp. 251-275, 2014.

[39] A. Baum, S. Nicola, S. Abdalah et al., “Optical characterization of PMMA phase gratings written by a 387 nm femtosecond laser”, Optics Communications, vol. 284, no. 12, pp. 2771-2774, 2011.

[40] S. Nolte, M. Will, J. Burghoff et al., “Femtosecond waveguide writing: A new avenue to three-dimensional integrated optics”, Applied Physics A: Materials Science and Processing, vol. 77, no. 1, pp. 109-111, 2003.

[41] L. Shah, A. Arai, S. Eaton et al, “Waveguide writing in fused silica with a femtosecond fiber laser at 522 nm and 1 MHz repetition rate”, Optics express, vol. 13, no. 6, pp. 1999-2006, 2005.

[42] K. Itoh, W. Watanabe, S. Nolte et al., “Ultrafast Processes for Bulk Modification of Transparent Materials”, MRS Bulletin, vol. 31, no. 8, pp. 620-625, 2006.

[43] C. Hnatovsky, R. Taylor, E. Simova et al., “Fabrication of microchannels in glass using focused femtosecond laser radiation and selective chemical etching”, Applied Physics A-Materials Science |& Processing, vol. 84, pp. 47-61, 2006.

[44] O. Svelto, *Principles of Lasers*, Springer, 2010.

[45] V. Diez-Blanco, J. Siegel, A. Ferrer et al., “Deep subsurface waveguides with circular cross section produced by femtosecond laser writing”, Applied Physics Letters, vol. 91, no. 5, pp. 051104, 2007.

[46] G. New, *Introduction to Nonlinear Optics*. Cambridge University Press, 2011.

[47] R. Osellame, R. Cerullo and G. Ramponi, *Femtosecond Laser Micromachining*, Springer, 2012.

[48] Altechna, *Watt Pilot Motorized Attenuator User Manual*, 2015.

[49] C. McCutchen, “Superresolution in microscopy and the Abbe resolution limit”, Journal of the Optical Society of America, vol. 57, no. 10, pp. 1190-1192, 1967.

[50] R. Mikhail, “Not All Beams Are Created Equal”, Industrial Photonics, vol. 1, no. 3, pp. 12-14, 2014.

[51] D. Alexandre, “Desenvolvimento de uma unidade de escrita directa laser para fabricação de dispositivos ópticos integrados”, MSc dissertation, 2003.

[52] D. Lopes, "Femtosecond Laser Direct Writing: Fabrication and Characterization of Waveguides and Gratings", MSc dissertation, 2014.

[53] K. Okamoto, *Fundamentals of Optical Waveguides*, Academic Press, 2006.

[54] C. Chen, *Foundations for Guided-Wave Optics*, Wiley, 2006.

[55] G. Agrawal, *Fiber-Optic Communications Systems*, Wiley, 2002.

[56] J. Yamauchi, O. Saito, M. Ikegaya et al., "Comparison of insertion losses of s-shaped optical waveguide bends", Microwave and Optical Technology Letters, vol. 7, no. 9, pp. 399-401, 1994.

[57] R. Kashyap, *Fiber Bragg Gratings*, Academic Press, 2010.

[58] H. Zhang and P. Herman, "Chirped Bragg Grating Waveguides Directly Written Inside Fused Silica Glass With an Externally Modulated Ultrashort Fiber Laser", IEEE Photonics Technology Letters, vol. 21, no. 5, pp. 277-279, 2009.

[59] J. Grenier, L. Fernandes, J. Aitchison et al., "Femtosecond laser fabrication of phase-shifted Bragg grating waveguides in fused silica", Optics Letters, vol. 37, no. 12, pp. 2289-2291, 2012.

[60] P. Zeil, C. Voigtländer, J. Thomas et al., "Femtosecond laser-induced apodized Bragg grating waveguides", Optics Letters, vol. 38, no. 13, pp. 2354-2356, 2013.

[61] V. Maselli, J. Grenier, S. Ho et al., "Femtosecond laser written optofluidic sensor: Bragg grating waveguide evanescent probing of microfluidic channel", Optics Express, vol. 17, no. 14, pp. 11719-11729, 2013.

[62] M. Pu, N. Yao, C. Hu et al., "Directional coupler and nonlinear Mach-Zehnder interferometer based on metal-insulator-metal plasmonic waveguide", Optics express, vol. 18, no. 20, pp. 21030-21037, 2010.

[63] X. Xing and Y. Wang, "A Planar Lightwave Circuit Based on Optical Add-Drop Multiplexer with 16 Tunable Wavelength Channels", Advanced Materials Research, vol. 216, pp. 661-665, 2011.

[64] L. Fernandes, J. Grenier, P. Herman et al., "Femtosecond laser fabrication of birefringent directional couplers as polarization beam splitters in fused silica", Optics Express, vol. 19, no. 13, pp. 11992-11999, 2011.

[65] G. Valle, R. Osellame and P. Laporta, "Micromachining of photonic devices by femtosecond laser pulses", Journal of Optics A: Pure and Applied Optics, vol. 11, no. 1, pp. 013001, 2009.

[66] I. Sohn, M. Lee, H. Park et al., “Direct writing of a 1-to-4 optical splitter and packaging technology using a femtosecond laser”, Journal of the Korean Physical Society, vol. 52, no. 4, pp. 1120-1122, 2008.

[67] R. He, I. Hernández-Palmero, C. Romero et al., “Three-dimensional dielectric crystalline waveguide beam splitters in mid-infrared band by direct femtosecond laser writing”, Optics Express, vol. 22, no. 25, pp. 31293, 2014.

[68] J. Lv, Y. Cheng, W. Yuan et al., “Threedimensional femtosecond laser fabrication of waveguide beam splitters in LiNbO_3 crystal” Optical Materials Express, vol. 5, no. 6, pp. 1274-1280, 2014.

[69] J. LeBouquin, J. Berger, P. Labeye et al., “Comparison of integrated optics concepts for a near-infrared multi-telescope beam combiner”, In Proceedings of SPIE, New Frontiers in Stellar Interferometry, pp. 1362–1369, 2004.

[70] Y. Wang, S. Gao, K. Wang et al., “Ultra-broadband and low-loss 3 dB optical power splitter based on adiabatic tapered silicon waveguides”, Optics Letters, vol. 41, no. 9, pp. 2053-2056, 2016.

[71] L. Wang, J. An, Y. Wu et al., “Design and fabrication of novel symmetric low-loss 1x24 optical power splitter”, Journal of Lightwave Technology, vol. 32, no. 18, pp. 3112-3118, 2014.

[72] J. Gamet and G. Pandraud, “Ultralow-loss 1 x 8 splitter based on field matching Y junction”, IEEE Photonics Technology Letters, vol. 16, no. 9, pp. 2060-2062, 2004.

[73] K. Færch and M. Svalgaard, “Symmetrical Waveguide Devices Fabricated by Direct UV Writing”, IEEE Photonics Technology Letters, vol. 14, no. 2, pp. 173-175, 2002.

[74] A. Hosseini, D. Kwong, Y. Zhang et al., “1xN multimode interference beam splitter design techniques for on-chip optical interconnections”, IEEE Journal on Selected Topics in Quantum Electronics, vol. 17, no. 3, pp. 510-515, 2011.

[75] L. Soldano, F. Veerman, M. Smit et al., “Planar Monomode Optical Couplers Based on Multimode Interference Effects”, Journal of Lightwave Technology, vol. 10, no. 12, pp. 1843-1850, 1992.

[76] J. Porque, P. Coudray, R. Charters et al., “WDM based on multimode interference-coupler built in an organic-inorganic material”, Optics Communications, vol. 183, no. 1, pp. 45-49, 2000.

[77] A. Al-hetar, A. Supa’at, A. Mohammad et al., “Multimode interference photonic switches” Optical Engineering, vol. 47, no. 11, pp. 112001, 2008.

[78] F. Yu, K. Yamamoto, X. Piao et al., “Multimode interference waveguide switch of electro-optic polymer with tapered access waveguides”, Physics Procedia, vol. 14, pp. 25-28, 2011.

[79] W. Watanabe, Y. Note and K. Itoh, “Fabrication of multimode interference waveguides in glass by use of a femtosecond laser”, Optics Letters, vol. 30, no. 21, pp. 2888-2890, 2005.

[80] C. Alegria, “All-Fibre Devices for WDM Optical Communications”, Ph.D. thesis, 2001.

[81] T. Erdogan, T. Strasser, M. Milbrodt et al., “Integrated-optical Mach-Zehnder add-drop filter fabricated by a single UV-induced grating exposure”, Applied Optics, vol. 36, no. 30, pp. 7838-7845, 1997.

[82] L. Eldada, S. Yin, C. Poga et al., “Integrated Multichannel OADM’s Using Polymer Bragg Grating MZI’s”, Photonics Technology Letters, vol. 10, no. 10, pp. 1416-1418, 1998.

[83] L. Dong, P. Hua, T. Briks et al., “Novel add/drop filters for wavelength-division-multiplexing optical fiber systems using a Bragg grating assisted mismatched coupler”, IEEE Photonics Technology Letters, vol. 8, no. 12, pp. 1656-1658, 1996.

[84] W. Shi, X. Wang, C. Lin et al., “Silicon photonic grating-assisted, contra-directional couplers”, Optics Express, vol. 21, no. 3, pp. 3633-3650, 2013.

[85] L. Fernandes, J. Grenier, P. Herman et al., “Stress induced birefringence tuning in femtosecond laser fabricated waveguides in fused silica”, Optics Express, vol. 20, no. 22, pp. 24103-24114, 2012.

Annex

Pyhton code used to analyze the directional coupler's data as a function of wavelength:

```
# -*- coding: utf-8 -*-

from numpy import*
import numpy as np
import matplotlib.pyplot as plt
from scipy.special import j1,yn
from scipy.optimize import curve_fit
from numpy import sin,linspace,pi
from mpl_toolkits.mplot3d import Axes3D
import pylab

data_horizontal=["S=10um_horizontal_L=0um.txt","S=10
    um_horizontal_L=180um.txt","S=10um_horizontal_L=360um.txt","S
    =10um_horizontal_L=540um.txt","S=10um_horizontal_L=720um.txt"
    ,"S=10um_horizontal_L=900um.txt","S=10um_horizontal_L=1080um.
    txt","S=10um_horizontal_L=1260um.txt","S=10um_horizontal_L
    =1440um.txt","S=10um_horizontal_L=1620um.txt","S=10
    um_horizontal_L=1800um.txt","S=10um_horizontal_L=1980um.txt",
    "S=10um_horizontal_L=2160um.txt","S=10um_horizontal_L=2340um.
    txt","S=10um_horizontal_L=2520um.txt","S=10um_horizontal_L
    =2700um.txt","S=10um_horizontal_L=2880um.txt","S=10
    um_horizontal_L=3060um.txt","S=10um_horizontal_L=3240um.txt",
    "S=10um_horizontal_L=3420um.txt","S=10um_horizontal_L=3600um.
    txt","S=10um_horizontal_L=3780um.txt","S=10um_horizontal_L
    =3960um.txt","S=10um_horizontal_L=4140um.txt","S=10
    um_horizontal_L=4320um.txt","S=10um_horizontal_L=4500um.txt"]
data_horizontal_adjustment
    =[-4.426456653569754,-9.265353663661058,-11.09378653567654,-19.074785422244

data_vertical=["S=10um_vertical_L=0um.txt","S=10um_vertical_L
    =180um.txt","S=10um_vertical_L=360um.txt","S=10um_vertical_L
```

```
    =540um.txt","S=10um_vertical_L=720um.txt","S=10um_vertical_L
    =900um.txt","S=10um_vertical_L=1080um.txt","S=10um_vertical_L
    =1260um.txt","S=10um_vertical_L=1440um.txt","S=10
    um_vertical_L=1620um.txt","S=10um_vertical_L=1800um.txt","S
    =10um_vertical_L=1980um.txt","S=10um_vertical_L=2160um.txt","
    S=10um_vertical_L=2340um.txt","S=10um_vertical_L=2520um.txt",
    "S=10um_vertical_L=2700um.txt","S=10um_vertical_L=2880um.txt"
    ,"S=10um_vertical_L=3060um.txt","S=10um_vertical_L=3240um.txt
    ","S=10um_vertical_L=3420um.txt","S=10um_vertical_L=3600um.
    txt","S=10um_vertical_L=3780um.txt","S=10um_vertical_L=3960um
    .txt","S=10um_vertical_L=4140um.txt","S=10um_vertical_L=4320
    um.txt","S=10um_vertical_L=4500um.txt"]
data_vertical_adjustment
    =[-4.756377537659732,-9.759885071682856,-11.97011894657786,-21.934813670280


data_horizontal_matrix=np.zeros((25,1001))
data_vertical_matrix=np.zeros((25,1001))

i=1
while i<=len(data_horizontal)-1:
    x=loadtxt(data_horizontal[i-1])    #load the input.dat file
        data to an array
    x=x[:,1]
    f1=data_horizontal_adjustment[i-1]-x[833]
    y=loadtxt(data_vertical[i-1])    #load the input.dat file
        data to an array
    y=y[:,1]
    f2=data_vertical_adjustment[i-1]-y[833]
    for u in range (0,len(x)):
        if u==0:
            data_horizontal_matrix[i-1,u]=1-(10**((((3*x[u]+2*x[
                u+1]+x[u+2])/6)+f1)/10))
            data_vertical_matrix[i-1,u]=1-(10**((((3*y[u]+2*y[u
                +1]+y[u+2])/6)+f1)/10))
        elif u==1:
            data_horizontal_matrix[i-1,u]=1-(10**((((2*x[u-1]+3*
                x[u]+2*x[u+1]+x[u+2])/8)+f1)/10))
            data_vertical_matrix[i-1,u]=1-(10**((((2*y[u-1]+3*y[
                u]+2*y[u+1]+y[u+2])/8)+f1)/10))
        elif u>=2 and u<=998:
```

```
                data_horizontal_matrix[i-1,u]=1-(10**((((x[u-2]+2*x[
                    u-1]+3*x[u]+2*x[u+1]+x[u+2])/9)+f1)/10))
                data_vertical_matrix[i-1,u]=1-(10**((((y[u-2]+2*y[u
                    -1]+3*y[u]+2*y[u+1]+y[u+2])/9)+f1)/10))
            elif u==999:
                data_horizontal_matrix[i-1,u]=1-(10**((((x[u-2]+2*x[
                    u-1]+3*x[u]+2*x[u+1])/8)+f1)/10))
                data_vertical_matrix[i-1,u]=1-(10**((((y[u-2]+2*y[u
                    -1]+3*y[u]+2*y[u+1])/8)+f1)/10))
            else:
                data_horizontal_matrix[i-1,u]=1-(10**((((x[u-2]+2*x[
                    u-1]+3*x[u])/6)+f1)/10))
                data_vertical_matrix[i-1,u]=1-(10**((((y[u-2]+2*y[u
                    -1]+3*y[u])/6)+f1)/10))
    x=0
    y=0
    i+=1

Wavelength=np.linspace(1300,1600,1001)
Coupler_Length=np.linspace(0,4.320,25)

def Directional_Coupler(L,k,phi):
    return (np.sin(k*L+phi))**2

def delta_r(L,W,k_v,k_h,phiv,phih):
    a=np.zeros((len(L),len(W)))
    u=0
    while u<len(W):
        a[:,u]=np.abs(np.sin((k_v[u]-k_h[u])*L+phiv[u]-phih[u])*
            np.sin((k_v[u]+k_h[u])*L+phiv[u]+phih[u]))
        u+=1
    return a

def Directional_Coupler2(L,W,k,phi):
    a=np.zeros((len(L),len(W)))
    u=0
    while u<len(W):
        a[:,u]=(np.sin(k[u]*L+phi[u]))**2
        u+=1
    return a
```

```
def Directional_Coupler3(L,k,phi):
    return (np.sin(k*L+phi))**2

Phi_horizontal=np.zeros(1001)
K_horizontal=np.zeros(1001)
Phi_vertical=np.zeros(1001)
K_vertical=np.zeros(1001)

p1=[0.57,1]
p2=[0.57,1]
for p in range(0,len(Wavelength)):
    fit1, fitCovariances1 = curve_fit(Directional_Coupler,
        Coupler_Length, data_horizontal_matrix[:,p],p0=p1)
    Phi_horizontal[p]=fit1[1]
    K_horizontal[p]=fit1[0]
    p1=[fit1[0],fit1[1]]
    fit2, fitCovariances2 = curve_fit(Directional_Coupler,
        Coupler_Length, data_vertical_matrix[:,p],p0=p2)
    Phi_vertical[p]=fit2[1]
    K_vertical[p]=fit2[0]
    p2=[fit2[0],fit2[1]]

plt.figure(1)
plt.plot(Wavelength,K_horizontal,linewidth=2.0, label='PH')
plt.plot(Wavelength,K_vertical,linewidth=2.0, label='PV')
plt.ylabel('K␣(rad/mm)', fontsize=18)
plt.xlabel('Wavelength␣(nm)', fontsize=18)
plt.legend(loc='best', fontsize=16)
plt.xticks(fontsize = 14)
plt.yticks(fontsize = 14)

f=plt.figure(2)
ax = f.add_subplot(111)
ax.yaxis.tick_right()
ax.yaxis.set_label_position("right")
plt.plot(Wavelength,Phi_horizontal,linewidth=2.0)
plt.plot(Wavelength,Phi_vertical,linewidth=2.0)
plt.ylabel('Phi␣(rad)', fontsize=18)
plt.xlabel('Wavelength␣(nm)', fontsize=18)
plt.legend(loc='best', fontsize=16)
plt.xticks(fontsize = 14)
```

```
plt.yticks(fontsize = 14)


Coupler_Length=np.linspace(0,70,1000)
X, Y = np.meshgrid(Wavelength, Coupler_Length)
kv=K_vertical
kh=K_horizontal
pv=Phi_vertical
ph=Phi_horizontal

for h in range(0,len(Wavelength)):
    if h==0:
        K_vertical[h]=(3*kv[h]+2*kv[h+1]+kv[h+2])/6.0
        K_horizontal[h]=(3*kh[h]+2*kh[h+1]+kh[h+2])/6.0
        Phi_vertical[h]=(3*pv[h]+2*pv[h+1]+pv[h+2])/6.0
        Phi_horizontal[h]=(3*ph[h]+2*ph[h+1]+ph[h+2])/6.0
    elif h==1:
        K_vertical[h]=(2*kv[h-1]+3*kv[h]+2*kv[h+1]+kv[h+2])/8.0
        K_horizontal[h]=(2*kh[h-1]+3*kh[h]+2*kh[h+1]+kh[h+2])
            /8.0
        Phi_vertical[h]=(2*pv[h-1]+3*pv[h]+2*pv[h+1]+pv[h+2])
            /8.0
        Phi_horizontal[h]=(2*ph[h-1]+3*ph[h]+2*ph[h+1]+ph[h+2])
            /8.0
    elif h>1 and h<len(Wavelength)-2:
        K_vertical[h]=(kv[h-2]+2*kv[h-1]+3*kv[h]+2*kv[h+1]+kv[h
            +2])/9.0
        K_horizontal[h]=(kh[h-2]+2*kh[h-1]+3*kh[h]+2*kh[h+1]+kh[
            h+2])/9.0
        Phi_vertical[h]=(pv[h-2]+2*pv[h-1]+3*pv[h]+2*pv[h+1]+pv[
            h+2])/9.0
        Phi_horizontal[h]=(ph[h-2]+2*ph[h-1]+3*ph[h]+2*ph[h+1]+
            ph[h+2])/9.0
    elif h==len(Wavelength)-2:
        K_vertical[h]=(kv[h-2]+2*kv[h-1]+3*kv[h]+2*kv[h+1])/8.0
        K_horizontal[h]=(kh[h-2]+2*kh[h-1]+3*kh[h]+2*kh[h+1])
            /8.0
        Phi_vertical[h]=(pv[h-2]+2*pv[h-1]+3*pv[h]+2*pv[h+1])
            /8.0
        Phi_horizontal[h]=(ph[h-2]+2*ph[h-1]+3*ph[h]+2*ph[h+1])
            /8.0
```

```
    else:
        K_vertical[h]=(kv[h-2]+2*kv[h-1]+3*kv[h])/6.0
        K_horizontal[h]=(kh[h-2]+2*kh[h-1]+3*kh[h])/6.0
        Phi_vertical[h]=(pv[h-2]+2*pv[h-1]+3*pv[h])/6.0
        Phi_horizontal[h]=(ph[h-2]+2*ph[h-1]+3*ph[h])/6.0

plt.figure(3)
plt.contourf(X,Y,delta_r(Coupler_Length,Wavelength,K_vertical,
    K_horizontal,Phi_vertical,Phi_horizontal))
plt.colorbar()
plt.ylabel('Interaction␣Length␣(mm)', fontsize=18)
plt.xlabel('Wavelength␣(nm)', fontsize=18)
plt.legend(loc='best', fontsize=16)
plt.xticks(fontsize = 14)
plt.yticks(fontsize = 14)

plt.figure(4)
Wavelength=np.linspace(1300,1600,1001)
Coupler_Length=np.linspace(0,4.320,25)
X, Y = np.meshgrid(Wavelength, Coupler_Length)
plt.contourf(X,Y,Directional_Coupler2(Coupler_Length,Wavelength,
    K_vertical,Phi_vertical))
plt.colorbar()
plt.ylabel('Interaction␣Length␣(mm)', fontsize=18)
plt.xlabel('Wavelength␣(nm)', fontsize=18)
plt.legend(loc='best', fontsize=16)
plt.xticks(fontsize = 14)
plt.yticks(fontsize = 14)

f=plt.figure(5)
ax = f.add_subplot(111)
ax.yaxis.tick_right()
ax.yaxis.set_label_position("right")
plt.plot(Coupler_Length,data_vertical_matrix[:,900],linewidth
    =2.0,label='1552nm')
plt.plot(Coupler_Length,data_vertical_matrix[:,250],linewidth
    =2.0,label='1375nm')
plt.plot(Coupler_Length,Directional_Coupler3(Coupler_Length,
    K_vertical[900],Phi_vertical[900]),linewidth=2.0,label='Fit')
plt.plot(Coupler_Length,Directional_Coupler3(Coupler_Length,
    K_vertical[250],Phi_vertical[250]),linewidth=2.0,label='Fit')
```

```
plt.ylabel('Coupling ratio', fontsize=18)
plt.xlabel('Interaction Length (mm)', fontsize=18)
plt.legend(loc='best', fontsize=16)
plt.xticks(fontsize = 14)
plt.yticks(fontsize = 14)
plt.axis([0.0,3.6,0,1])
plt.legend(loc='best', fontsize=13)
print(Wavelength[840])
print(Wavelength[250])

plt.show()
```